8-2016

Modeling fluid interactions with the rigid mush in alloy solidification

Alexander J. Plotkowski
Purdue University

Graduate School Form
30 Updated 12/26/2015

PURDUE UNIVERSITY
GRADUATE SCHOOL
Thesis/Dissertation Acceptance

This is to certify that the thesis/dissertation prepared

By Alexander J Plotkowski

Entitled
MODELING FLUID INTERACTIONS WITH THE RIGID MUSH IN ALLOY SOLIDIFICATION

For the degree of Doctor of Philosophy

Is approved by the final examining committee:

Matthew J. M. Krane, Ph.D. Chair	Kevin Trumble, Ph.D.
David Johnson, Ph.D.	Timothy Fisher, Ph.D.

To the best of my knowledge and as understood by the student in the Thesis/Dissertation Agreement, Publication Delay, and Certification Disclaimer (Graduate School Form 32), this thesis/dissertation adheres to the provisions of Purdue University's "Policy of Integrity in Research" and the use of copyright material.

Approved by Major Professor(s): Matthew J. M. Krane, Ph.D.

Approved by: David Bahr, Ph.D. 5/24/2016
Head of the Departmental Graduate Program Date

MODELING FLUID INTERACTIONS WITH THE RIGID MUSH IN ALLOY SOLIDIFICATION

A Dissertation

Submitted to the Faculty

of

Purdue University

by

Alexander J Plotkowski

In Partial Fulfillment of the

Requirements for the Degree

of

Doctor of Philosophy

August 2016

Purdue University

West Lafayette, Indiana

This work is dedicated to my family, and especially to my wife Andrea, whose support throughout graduate school was invaluable.

ACKNOWLEDGEMENT

First and foremost I would like to acknowledge the support of my family and my wife, Andrea, over the last four years. Graduate school has been a rewarding, but difficult challenge, and without their encouragement, this work would not have been possible. I would also like to thank my adviser, Dr. Krane, who supervised this work, as well as the support and contributions from my graduate committee: Dr. Trumble, Dr. Johnson, and Dr. Fisher. Additional thanks are owed to the staff of the School of Materials Engineering who enabled much of this research, and especially to Tim Vanmeter who was always available for help in the MSE labs, and Vicki Cline for her academic advising.

I would also like to acknowledge the financial support that has made my research possible. Dr. Bahr and the School of Materials Engineering at Purdue University made sure that I was free to do my best work when other sources of funding were not available. Jack deBarbadillo, Special Metals Corporation, and the Air Force Research Lab provided funding and valuable experience during my second year of graduate school with support provided by the USAF MAI project: “Development of an ICME-based tool for Remelting Processes for High-Performance Aerospace Alloys”, USAF Agreement Order FA8650-11-5224-B. And finally, Robert Wagstaff and Novelis Inc. supplied the financial gift that funded the majority of this work without restricting the direction or scope of my research.

Finally, I would like to thank the other graduate students who made it a pleasure to come to work each day and helped with this research. My work would have been impossible without Jeff Yanke's previous contributions and advice. Thank you to Kyle Fezi and John Coleman for enlightening conversations that were integral to this work. Additional thanks to Andrew Kustas, Pikee Priya, Logan Kroneman, Dan Klenosky, Kara Luitjohan, Travis Thornell and many others who made graduate school such a joy during this process.

TABLE OF CONTENTS

Page

Page

Page

LIST OF TABLES

LIST OF FIGURES

Figure Page

Figure Page

Figure Page

Figure Page

Figure Page

Figure Page

Figure Page

NOMENCLATURE

Latin Symbols

c	Constant pressure specific heat
C^i	Mixture composition of component i
C_j^i	Composition of component i in phase j
d	Representative particle diameter
D	Mass diffusivity
f_i	Mass fraction of phase i
F	Weighting function
g_i	Volume fraction of phase i
$g_{s,c}$	Critical solid volume fraction for grain attachment
$g_{s,p}$	Packing fraction
$\bar{g}_{s,p}$	Average packing fraction
Δg_s	Packing range
k	Thermal conductivity, partition coefficients, number of iterations
K	Permeability
L_f	Latent heat of fusion
m	Current iteration level
n	Weighting exponent
p	Pressure
P	Packed fraction
r	Radial coordinate

Latin Symbols

S_{rigid}	Momentum source terms in the rigid region
S_{slurry}	Momentum source terms in the slurry region
t	Time
T	Temperature
u	Axial mixture velocity
v	Radial mixture velocity
$\vec{V}$	Mixture velocity vector
z	Axial coordinate

Greek Symbols

α	Shape parameter of the Weibull distribution
β	Scale parameter of the Weibull distribution
$\beta_{T,i}$	Coefficient of thermal expansion for phase i
$\beta_{S,j}^{i}$	Coefficient of solutal expansions for component i in phase j
γ	Threshold value for the Weibull distribution
ρ	Mixture density
$\Delta\rho$	Difference between solid and liquid densities
μ_i	Viscosity of phase i
$\bar{\mu}_s$	Average solid viscosity

Subscripts

ds	Downstream cell
l	Liquid
nb	Neighboring cell
p	Cell of interest
s	Solid

ABSTRACT

Plotkowski, Alexander J. Ph.D., Purdue University, August 2016. Modeling Fluid Interactions with the Rigid Mush in Alloy Solidification. Major Professor: Matthew Krane.

Macrosegregation is a casting defect characterized by long range composition differences on the length scale of the ingot. These variations in local composition can lead to the development of unwanted phases that are detrimental to mechanical properties. Unlike microsegregation, in which compositions vary over the length scale of the dendrite arms, macrosegregation cannot be removed by subsequent heat treatment, and so it is critical to understand its development during solidification processing. Due to the complex nature of the governing physical phenomena, many researchers have turned to numerical simulations for these predictions, but properly modeling alloy solidification presents a variety of challenges. Among these is the appropriate treatment of the interface between the bulk fluid and the rigid mushy zone. In this region, the non-linear and coupled behavior of heat transfer, fluid mechanics, solute transport, and alloy thermodynamics has a dramatic effect on macrosegregation predictions. This work investigates the impact of numerical approximations at this interface in the context of a mixture model for alloy solidification.

First, the numerical prediction of freckles in columnar solidification is investigated, and the predictive ability of the model is evaluated. The model is then extended to equiaxed solidification, in which the analogous interface is the transition of free-floating solid particles to a rigid dendritic network. Various models for grain attachment are investigated, and found to produce significant artifacts caused by the discrete nature of their implementation on the numerical grid. To reduce the impact of these artifacts, a new continuum grain attachment model is proposed and evaluated. The differences between these models are compared using uncertainty quantification, and recommendations for future research are presented.

CHAPTER 1. INTRODUCTION

1.1 Macrosegregation during Alloy Solidification

During alloy solidification, the relative motion of solid and liquid results in long range compositional differences called macrosegregation. Unwanted local compositions can result in the precipitation of undesirable phases and negative effects on mechanical properties and downstream processing [1]. Unfortunately, the length scale of macrosegregation is on the order of the ingot, making it time prohibitive to remove through subsequent heat treatments due to limited solid state mass diffusivity. The development of such defects is the result of the complex and coupled transport phenomena and alloy thermodynamics. As a result, the analytical prediction of alloy solidification behavior is limited to only the simplest of cases, and complex numerical models must be used to understand any application of practical size and complexity.

The focus of this work is the prediction of macrosegregation during both columnar and equiaxed solidification using numerical models. In both modes of solidification, the interaction between bulk convection fluid flow and the edge of the rigid mush plays a critical role in macrosegregation development. As this work will show, an accurate representation of this interaction is crucial to produce physically meaningful predictions, and failures to do so result in numerical artifacts that limit the predictive capabilities of

the model. In particular, the development of channel segregation (a sub-class of macrosegregation defect) is investigated for both types of solidification, and numerical contributions to their formation and propagation are evaluated. Finally, recommendations for columnar solidification simulations and new model developments for equiaxed solidification are presented.

1.2 Columnar Solidification

1.2.1 Freckles and Freckle Criteria

Freckles are a type of macrosegregation defect in which a string of equiaxed grains form in an otherwise columnar structure [2,3]. Freckles are also enriched in elements with a partition coefficients less than one and depleted of elements with partition coefficients greater than one. These local inhomogeneities in grain structure and composition result in unsatisfactory mechanical properties, and cast components that contain these defects must be scrapped. Freckle formation is of primary concern in the production of nickel-based superalloys [2–4] and specialty steels [5,6], but also affect various other alloy systems [7–9] and has been directly observed in aqueous ammonium chloride, a transparent alloy analogue [10,11].

It is now generally accepted that this family of defects arises from flow through interdendritic channels driven by solutal buoyancy [12,13]. The advection of enriched liquid in the interdendritic region causes a local remelting through the coupling of the thermosolutal field with the alloy phase change. The increased permeability in the

channel enables additional flow of enriched liquid, and the process becomes a positive feedback loop, allowing the channel to propagate into the casting as the solidification front moves forward. The direction of channel propagation is determined by the direction of the combined solutal and thermal buoyancy forces. In cases where convective flow is dominated by the upward buoyancy of lighter alloying elements, as is observed in some nickel-based superalloys and high alloy steels, freckles form in an upward direction. In cases where the solutal buoyancy is dominated by comparatively dense elements, the solutal effect aids the downward thermal buoyancy and freckles are more likely to propagate downward.

Even with an understanding of the mechanism of freckle formation, the accurate prediction of these defects has remained an elusive goal. The interaction among the buoyancy driving forces, thermodynamics, and mush permeability are complex, and further complicated by the influence of any bulk fluid flow near the edge of the mushy zone. Much research has sought to develop a criterion for freckle formation. One approach casts the criterion as a simple mathematical function of the local temperature gradient and solidification rate [5–7,10] generally based on the time available for a channel to form within the mushy zone as a function of the alloy properties and cooling conditions. While the evaluation of these criteria are relatively simple, the critical value to which they are compared is an unclear function of the alloy system and solidification geometry, and therefore, generally determined empirically.

Another set of criteria has been developed from various formulations of the Rayleigh number [2,3,14,15], which describes the ratio between buoyancy driving forces

and opposing viscous forces. This approach is inspired by the Benard problem, in which a critical value of the Rayleigh number predicts the onset of buoyancy-driven fluid motion in a horizontal fluid layer uniformly heated from below and cooled from above [16]. This configuration is always mechanically unstable due to the lighter fluid below, but the upward buoyancy must reach a certain level before flow begins. There is an obvious physical analogy with an alloy with a lighter interdendritic liquid, cooled from below and growing against gravity. It is expected that a critical Rayleigh number could be found which predicts the onset of upward plumes which begin freckle formation. Unfortunately, a satisfactory form of the Rayleigh number that includes the effects of the mushy zone characteristics and can be applied generally to any alloy or system geometry has not yet been formulated.

The alloys in which freckles have been most studied are nickel-based superalloys and steels, in which the rejected solute is much less dense than the nominal liquid and, consequently, freckles form in the upward direction. As noted above, much work has been done to study the particular case of directional solidification, primarily because it is applicable to the casting of turbine blades [2,3,11]. Other system configurations, however, may be significantly affected by bulk fluid flow driven by thermosolutal convection. Very few studies have attempted to formulate criteria for a range of solidification front angles [2,3], but are only applicable to angles near the horizontal directional solidification case. They cannot be used for more complex solidification conditions such as those found in ingot production for nickel superalloys and specialty steels or even static castings cooled from a vertical side-wall. There is still a significant need for a general freckle criterion. It

must consider alloys with either positive or negative solutal buoyancy, any arbitrary solidification front angle, and the effect of the bulk fluid flow near the edge of the mushy zone. Significant future research will be required to formulate such a criterion.

1.2.2 Numerical Predictions of Freckles

To predict freckle formation and test various criteria, researchers have often turned to numerical simulations of alloy solidification in place of expensive and time consuming experimentation. Simulations also have the advantage of easy access to system information that is difficult to observe or measure experimentally. There are two different types of simulations that may be used in this manner. The first models the sharp solid-liquid interface on the scale of the dendrite arm spacing [17,18]. The computational expense of these models due to the fine scale grid required limits their use for casting scale predictions. For larger length scales and coarser grids, a more common approach to solidification modeling is the continuum formulation [19,20]. These models average the solid fraction and other physical parameters over representative control volumes. This approach drastically reduces the computational expense and allows for the use of standard finite volume or finite element solution techniques.

A variety of studies have used continuum simulations to predict freckles in directional solidification, and several have investigated the effect of grid size or other numerical parameters. Frueh *et al.* [21] found, using a finite element model, that the predicted level of segregation and magnitude of convective flow in directional solidification was strongly impacted by the chosen domain size, but that the presence of

freckles was not. In a similar model, Sung *et al.* [22] performed finite element simulations for directional solidification of Rene N5 and found that whether or not freckles appeared was dependent on the mesh size used. They suggested that a grid spacing smaller than twice the primary dendrite arm spacing be used to achieve the most realistic results. In a subsequent study, Sung *et al.* [23] even used a horizontal element size smaller than the dendrite arm spacing. While these simulations appear to predict freckle formation, the computational expense of such small grid sizes is not practical for simulations of larger castings. Guo and Beckermann [24] evaluated a finite element model for various element sizes in a three-dimensional simulation and found that, particularly for the initial stages of flow instability, grid independent results were not achieved.

Finite volume simulations have also been used to predict freckles in directional solidification [25] and other solidification configurations [26–28]. However, similar to finite element simulations, numerical effects have often been reported. Combeau *et al.* [26] compared freckle formation predicted by several different solidification codes. The alloy studied was Pb-18wt.%Sn in a rectangular cavity cooled from the side. They found that the number of freckles, their shape, and the level of segregation contained within the channels was dependent on the simulation software. Kumar *et al.* [27] studied the effect of the discretization of the mushy zone permeability term in the momentum conservation equations and the grid size on freckle appearance for Sn-5wt.%Pb alloy in a rectangular cavity cooled from the side (this term represents the drag the solid dendrite impart on the liquid moving through the mushy zone). They found that the choice of numerical discretization scheme for the permeability had a dramatic effect on the

number and severity of channel segregates. The number of freckles was also dependent on the mesh size, with more appearing for coarser grids. Li *et al.* performed finite volume simulations of a 2.45 ton ingot of plain carbon steel [29]. They found that decreasing the grid spacing resulted in a higher number density of predicted A-segregates.

Vušanović and Voller [28] examined the mechanism of channel initiation in numerical models in order to better understand the origins of their grid dependence. They compared a traditional implicit time-stepping scheme for a volume averaged mixture formulation of the governing conservation equations for momentum, energy, and species to a hybrid technique [30,31] that used an explicit time-stepping scheme for the energy and species equations before solving the momentum equations in an implicit manner within each time step. Their simulations were uniformly capped at 20 iterations per time step, which artificially introduced numerical noise to the system in the form of convergence residuals, but because the explicit scheme requires only a single iteration per time step, the hybrid method inherently reduced the numerical error in the system. For an Al–4.5wt.%Cu alloy in a rectangular cavity cooled from the side, they found the hybrid method to be more stable at various time steps and grid sizes due to the reduction in noise from convergence residuals. While this study is not applicable to most simulations in which strict convergence criteria are achieved, it does suggest a method for studying the numerical dependence of freckle formation in the introduction of instabilities from excessive convergence residuals. This technique will be used in CHAPTER 3 to exacerbate channel segregate phenomena.

1.2.3 Columnar Study Objectives

There are still open questions about the ability of volume averaged solidification simulations to accurately predict the formation of freckles. Particularly in the case of larger geometries (applicable for many casting processes such as large steel ingots, electroslag remelting, and vacuum arc remelting) in which numerical cell sizes on the length scale of the dendrite arm spacing is not practical, and for thermal boundary conditions that produce solidification fronts very different from directional solidification. The objective of the portion of this work pertaining to columnar solidification is primarily to understand the mechanism for channel formation and propagation in these simulations. To do so, the approach of Vušanović and Voller [28] of limiting the number of iterations per time step is employed to exaggerate channel formation in a mixture formulation of columnar solidification based on the work of Bennon and Incropera [19,20]. The effect of numerical noise in the form of convergence residuals on freckle development and grid dependence is discussed and the numerical nature of channel initiation is used to evaluate the physical relevance of freckle predictions in macroscale process modeling. Finally, recommendations are made for convergence criteria that enable stable, representative results.

1.3 Equiaxed Solidification

In many industrial applications, including direct chill casting of aluminum alloys [32] and magnesium processing [33], grain refiner is added to the liquid metal to encourage a uniform, equiaxed microstructure. Predicting macrosegregation in equiaxed solidification

presents several challenges from a modeling standpoint. Grains initially nucleate in the melt on the grain refiner particles, and may be freely advected by the surrounding liquid metal before eventually coalescing into a rigid solid structure (Figure 1.1). The motion of free-floating particles with respect to the bulk fluid flow, their coalescence into a rigid solid structure, and the permeability of the resulting solid network all affect the overall macrosegregation distribution and each necessitates careful numerical consideration. In particular, the shape of the interface between the slurry (containing free-floating grains) and rigid solid regions has a dramatic effect on the local fluid flow due to the damping effect of the dendrite permeability. The point at which this transition occurs is often measured in terms of the local volume fraction solid at the time of the transition and is referred to as the dendrite coherency point or packing fraction.

1.3.1 Dendrite Coherency

A common assumption among many early models of equiaxed solidification [34,35] is that the morphology of the equiaxed grains is spherical. In this case, the packing fraction may be taken as 0.637, equal to the density of random close packed spheres [36]. In reality however, any deviation from this spherical assumption towards a dendritic morphology will result in a decrease in the actual packing fraction (if measured in terms of the volume fraction solid). Several experimental studies have sought to determine the packing fraction for a variety of alloys and solidification conditions using two different experimental approaches. Rheological methods test the shear strength of an alloy

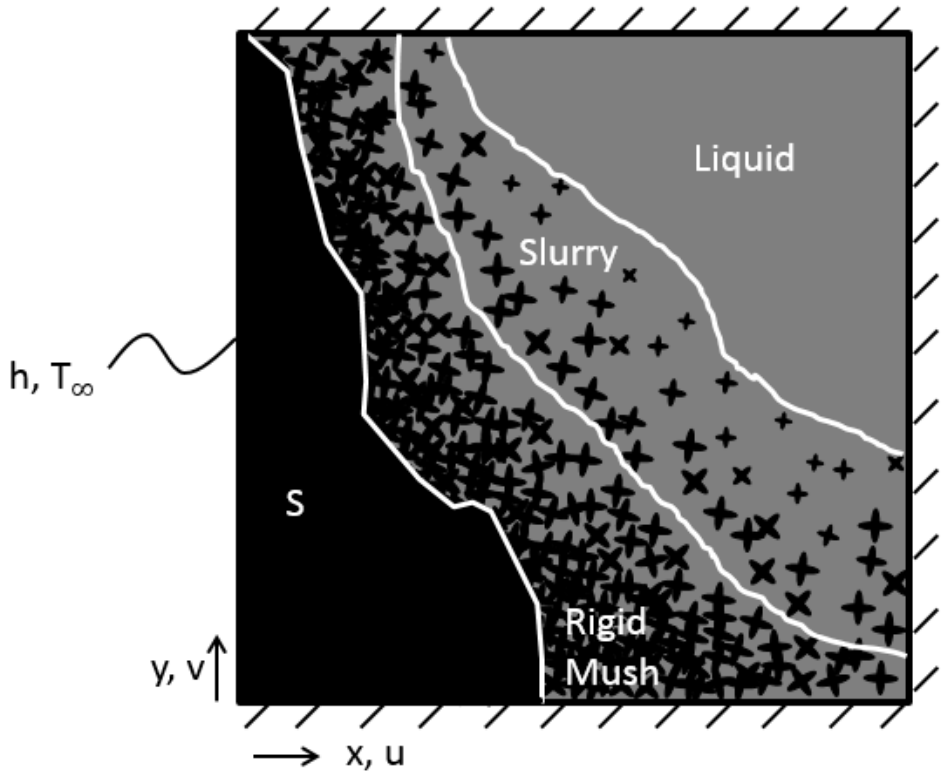

Figure 1.1: Schematic showing the different regions of a grain refined casting including all-solid, the rigid mush, the slurry region (containing free-floating equiaxed grains) and all liquid.

through the freezing range and the coherency point is marked by a sudden change in slope [37–40]. Alternatively, thermal analyses measure the temperature difference between two points, which exhibits a minimum at coherency due to the increased thermal transport in the solid [41,42]. Arnberg and coworkers performed a series of studies reporting measured coherency fraction for various aluminum alloys [41,43–45] which ranged widely, including very low packing fractions for Si-rich foundry alloys (0.06-0.10 for alloy B390) to higher values for Zn-rich alloys (0.23-0.34 for alloy 713) and pure aluminum (0.53 for 99.99 wt.% Al). This last value, measured in a metal which produces

no dendrites, approaches the spherical assumption discussed above. Each result is for a particular solidification condition, alloy composition, and level of grain refinement, all of which may affect the dendrite morphology and number of equiaxed particles. Generally speaking, increased solute content [43] and cooling rate [41] tend to reduce the packing fraction by encouraging highly dendritic morphologies, while larger grain refiner additions [42] form a more globular microstructure and increase the packing fraction.

1.3.2 Review of Equiaxed Solidification Models

To give context to the specific model used in this study, a brief review of equiaxed solidification models is first presented. The multi-phase and mixture formulations represent two distinct approaches to modeling equiaxed solidification, each with advantages and disadvantages.

1.3.2.1 Multi-Phase Models

The general approach of multi-phase formulations is to solve governing conservation equations for each phase considered within the system. Ni and Beckermann [34] proposed a volume-averaged, two-phase model for transport phenomena in solidification processing which was later used to model equiaxed solidification in vertical direct chill casting of an Al-Cu alloy by Reddy and Beckermann [35]. The model considers the solid and liquid phases separately and couples them using a variety of interfacial transfer terms. It also requires some type of nucleation model, or as Reddy and

Beckermann assume, some known number density of grains. They further assumed a globular grain morphology, and used a uniform and constant packing volume fraction that corresponds to the density of random close packed spheres [36], as the criterion for the coherency.

Wang and Beckermann expanded the two-phase model to include the interdendritic liquid as a third phase, allowing for modeling of the grain envelope [46,47], which includes the solid and the liquid trapped between the dendrite arms. They used a set of morphological relationships [48] to determine the fraction solid and solid-liquid interfacial area inside the grain envelope. Further relationships were used to govern grain nucleation and growth, as well as flow partitioning between the inter- and extradendritic liquid. This model used a slight variation on the previous packing criterion in that it was applied to the grain volume fraction (including the solid particles and interdendritic liquid) rather than the solid volume fraction. The grain envelopes were assumed spherical, and packing occurred at a grain volume fraction of 0.637. To treat the transition from free-floating to rigid solid in these models, Wang *et al.* [49] developed an interfacial drag term for the momentum equations that approaches Stokes' law for low solid fractions and the Blake-Kozeny permeability model above the packing fraction, and varies continuously through the transition in between.

Other models have been developed based on the multi-phase approach of Beckermann's group using as many as five phases [50,51] in which columnar and equiaxed grains, the interdendritic liquid in each type of solid structure, and the bulk liquid are considered separately in order to model the columnar to equiaxed transition [52,53].

These multi-phase formulations are very detailed in their inclusion of a wide range of relevant physical phenomena, including the ability to better model the mass transfer across phase boundaries allowing for the inclusion of detailed thermodynamic models, whereas the mixture models are primarily limited to the equilibrium and Scheil formulations. However, multi-phase models are also computationally expensive due to the need to solve a new set of governing equations for each phase. Additionally, the predictive ability that such detailed models in practice is severely limited by uncertainty in the correct values of a wide array of input parameters.

1.3.2.2 Mixture Models

The mixture approach to modeling solidification phenomena improves upon the computational expense of the multi-phase formulations by casting the governing conservation equations in terms of "mixture" variables, each of which includes contributions from the constituent phases. The computational expense is significantly reduced by solving only one set of conservation equations, and if necessary, the contributions of individual phases are calculated using supplemental relationships. The first of these models was formulated by Bennon and Incropera [19,20] for columnar growth and was later extended by Ni and Incropera [54,55] and Vreeman *et al.* [56,57] to equiaxed solidification.

These mixture models treat the transition from free-floating to rigid solid differently than the multi-phase models. The differing effects of the two regions (either

viscous effects in the slurry of free-floating particles or permeability effects in the rigid mush) are modeling using a set of source terms in the momentum conservation equations. These terms are turned on or off on a cell-by-cell basis depending on the conditions of a given cell, determined by the packing criterion. Commonly, this criterion is simply based on the local volume fraction solid and compared against some critical packing fraction. Unlike the three-phase models described above, the grain morphology is not modeled explicitly. Instead, the selection of the packing fraction implicitly defines the morphology for the domain. For highly globular grains, packing fractions approaching that for close packed spheres may be used. Alternatively, any lower value represents a continuum of "dendritic-ness". For example, Vreeman *et al.* used packing fraction between 0.15 and 0.3 for simulations of vertical direct-chill casting of Al-4.5wt.%Cu and Al-6.0wt.%Mg alloys [57].

1.3.2.3 Grain Attachment Schemes

The grain attachment (also referred to as packing or dendrite coherency) schemes described above for both model types may generally be referred to as constant packing fraction (CPF) schemes, in that the critical value at which grain attachment occurs is held constant and uniform throughout the domain. This approach is attractive in its simplicity and ease of implementation. However, it does not consider the effect of the local velocity field on the likelihood of grain attachment. Advection of solid particles indirectly influences the packing scheme by affecting the solid fraction field. However, particles are

more likely to pack if their velocity is towards a packed interface, and less likely to attach when advected away from the interface (Figure 1.2), an effect that is not considered in the constant packing fraction model, even in the multiphase cases that consider the local grain morphology [48]. Vušanović and Krane [58] introduced a simple rule set to account for the velocity field by basing packing not on the condition of the numerical cell of interest, but on the condition of a neighboring cell in the downstream direction. They implemented this approach in a simulation of horizontal direct chill casting of aluminum using the transport model of Vreeman et al. [56], and compared the velocity-based method to various constant packing fraction cases. However, they only looked at the new model under a single set of conditions. It is necessary to analyze the effects of the velocity-based model further in order to fully understand its differences from the constant packing fraction approach.

1.3.3 Equiaxed Study Objectives

The objective of this study is first to more closely examine the behavior of two velocity-based packing schemes as a function of the various model parameters for a mixture model of equiaxed solidification. The packing scheme proposed by Vušanović and Krane [58] and a new variant will be compared to the constant packing fraction approach used by Vreeman *et al.* [56] for a static casting of AA7050 (CHAPTER 4). It is found that these schemes all produce channel segregates that are similar in appearance to freckles found in columnar castings. The mechanism of these defects are examined in detail and shown to be numerical artifacts resulting from the discrete nature of the grain attachment

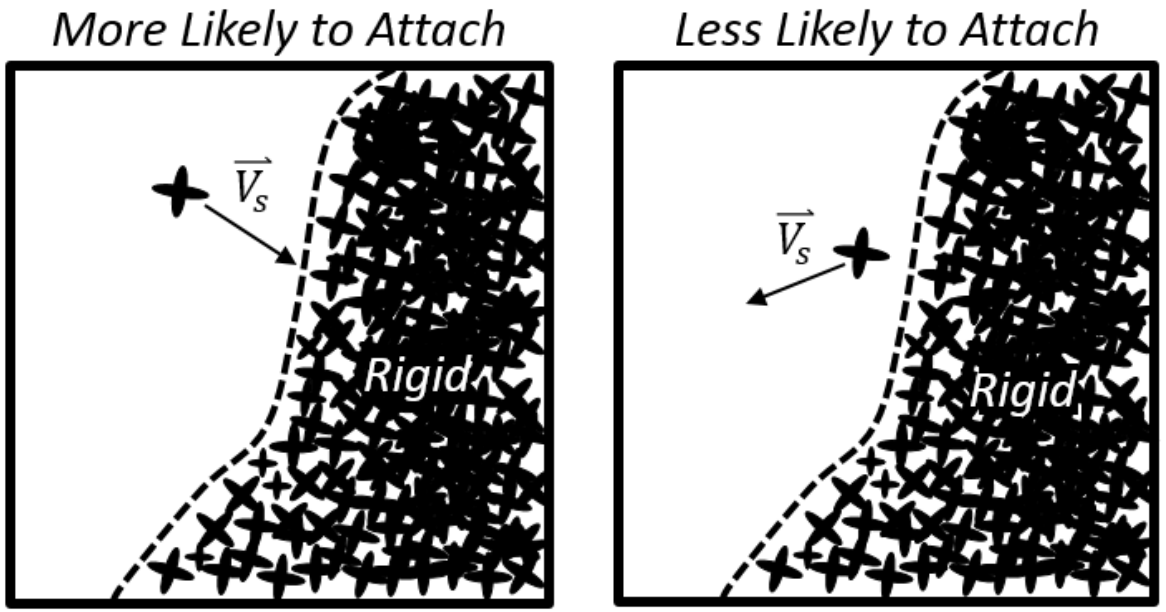

Figure 1.2: Schematic of a single equiaxed grain being advected (a) towards or (b) away from a rigid interface, demonstrating the rationale for a velocity based attachment model.

models (CHAPTER 5). In response to this finding, a new continuum grain attachment model is developed and compared to the discrete models (CHAPTER 6). Recommendations are made for future work to further improve grain attachment models for equiaxed solidification.

1.4 Uncertainty Quantification in Solidification Modeling

In order to understand the differences between models or between models and experimental results, comparisons within a single case are not sufficient. Instead, it is necessary to understand the effects of uncertain inputs on the distribution of outputs. For this reason, uncertainty quantification (UQ) has become increasingly common for fields such as heat transfer [59] and materials [60] modeling. Unfortunately, to this point, UQ has only gained limited adoption in the solidification community [61,62]. In the case of the present work, it is of interest to understand the differences between the predictions of the various grain attachment models for equiaxed solidification. Essentially, if the macrosegregation predictions for each of the attachment models mostly overlap over the uncertainty range of the inputs, then the selection of a given model may be made for considerations such as numerical stability or efficiency. On the other hand, if the predictions are significantly different, then effort should be put towards determining which model is most physically accurate.

This type of uncertainty, which pertains to the lack of knowledge in which model best represents the physical system, is referred to as epistemic uncertainty, also called reducible uncertainty. It is “reducible” in the sense that improved knowledge of the

physical system through careful experimentation would allow for the determination of the most appropriate model. However, even with very accurate information of a given input parameter, some uncertainty remains due to natural variation of its value and in the limitations of the associated measurements technique. This type of uncertainty is called aleatoric uncertainty and is irreducible.

The goal of uncertainty quantification is to determine the distribution of outputs that result due to the propagation of uncertain inputs. One way of generating an output distribution is the Monte Carlo method which randomly samples from the range of input variables to collect the corresponding output values. This method requires a large number of samples to produce a converged output distribution, however, which is not feasible given the computational expense of solidification models. Thankfully, methods have been developed to handle such cases. In this study, the PRISM uncertainty quantification (PUQ) framework, developed at Purdue University, is used to examine the effects of various input parameters on the predictions from each grain attachment model [63]. PUQ works by sampling only a select few points from the computational model, determined using the Smolyak sparse grid algorithm, and using generalized polynomial chaos (gPC) to fit a lower order surrogate model to the numerical outputs. Monte Carlo sampling is then performed on the efficient, lower order model to produce output distributions.

1.4.1 Uncertainty Quantification Study Objectives

This study has two main objectives related to the epistemic uncertainty of the grain attachment models. First, what is the magnitude of the effect of the velocity field on

macrosegregation predictions? If the constant packing fraction and velocity-based models produce the same outputs, then the inclusion of the solid velocity field in the packing criteria may be safely neglected. Alternatively, if the outputs are significantly different, then obtaining experimental data to validate the use of the velocity-based model becomes a priority.

Second, does the continuum packing model produce different results than the constant packing fraction model? (The continuum packing model is not compared to the velocity-based model in this case because the continuum approach is not intended to account for the velocity field.) There are several interesting components of this objective. First, the continuum scheme is not intended to produce significantly different results from the constant packing fraction model, only to eliminate unwanted numerical artifacts. Therefore, it is of interest if the outputs are also changed significantly as a result. Second, what is the effect of the new parameters introduced with the continuum model that do not apply to the discrete models? If the model is very sensitive to these parameters, then the overall distribution of the outputs may widen significantly, representing a need for new information about the appropriate values of these parameters.

CHAPTER 2. MODEL DESCRIPTION

2.1 A General Mixture Model for Alloy Solidification

2.1.1 Conservation Equations

The basis of the finite volume model used for this work is the mixture formulation proposed by Vreeman *et al.* [56,57], written here in cylindrical coordinates. Mass continuity may be expressed as

$$\nabla \cdot \left(\rho \vec{V}\right) = 0, \tag{2.1}$$

where ρ is the mixture density and $\vec{V}$ is the mixture velocity vector defined as $\vec{V} = f_s \vec{V}_s + f_l \vec{V}_l$, where $\vec{V}_i$ are the velocity vectors of the solid and liquid phases and f_i are the corresponding mass fractions. Shrinkage induced flow is not considered in the present model, so that ρ is not a function of phase, composition, or temperature, except as represented by the Boussinesq approximation, and the mass fractions of solid and liquid are equal to the respective volume fractions. However, to maintain generality of the model formulation, appropriate uses of the mass and volume fractions will be used throughout. Buoyancy forces caused by actual density differences between solid and

liquid are considered using a representative density difference, $\Delta\rho \neq 0$, in the relevant momentum equations and free-floating solid model. All other properties, unless otherwise noted, are assumed to be independent of composition, temperature, and phase.

The momentum conservation equations originally proposed by Vreeman *et al.* [56] will first be presented in the final form from that work, in which some source terms were neglected based on a preliminary scaling analysis. The equations are divided into two pairs, one for the liquid and slurry regions, and one for the rigid mush. In the liquid and slurry regions, the solid particles are collectively treated as a pseudo-fluid. Here, the axial and radial momentum conservation equations, respectively, are

$$\begin{aligned}
&\frac{\partial}{\partial t}(\rho u) + \nabla\cdot\left(\rho\vec{V}u\right) \\
&\quad = \nabla\cdot\left(\mu_l\frac{\rho}{\rho_l}\nabla u\right) - \nabla\cdot\left(\mu_l\frac{\rho f_s}{\rho_l}\nabla u_s\right) + \nabla\cdot\left(\bar{\mu}_s g_s \nabla u_s\right) + g_s\Delta\rho g \\
&\quad - \nabla\cdot\left[\frac{\rho f_s}{f_l}\left(\vec{V}-\vec{V}_s\right)(u-u_s)\right] \\
&\quad - g_s\rho_s g\left[\beta_{T,s}(T-T_0) + \sum_{i=1}^{m}\beta_{S,s}^{i}\left(C_s^i - C_0^i\right)\right] \\
&\quad - g_l\rho_l g\left[\beta_{T,l}(T-T_0) + \sum_{i=1}^{m}\beta_{S,l}^{i}\left(C_l^i - C_0^i\right)\right] - \frac{\partial p}{\partial z}
\end{aligned} \tag{2.2}$$

and

$$\frac{\partial}{\partial t}(\rho v) + \nabla \cdot \left(\rho \vec{V} v\right)$$

$$= \nabla \cdot \left(\mu_l \frac{\rho}{\rho_l} \nabla v\right) - \mu_l \frac{\rho}{\rho_l} \frac{v}{r^2} - \nabla \cdot \left(\mu_l \frac{\rho f_s}{\rho_l} \nabla v\right) + \mu_l \frac{\rho f_s}{\rho_l} \frac{v}{r^2} \tag{2.3}$$

$$+ \nabla \cdot (\bar{\mu}_s g_s \nabla v) - \bar{\mu}_s g_s \frac{v}{r^2} - \frac{\partial p}{\partial r},$$

where t is time, u and v the axial and radial velocity components, g_s and g_l the solid and liquid volume fractions, μ_l the liquid viscosity, $\bar{\mu}_s$ the average solid viscosity, g the acceleration due to gravity, $\beta_{T,s}$ and $\beta_{T,l}$ the solid and liquid thermal expansion coefficients, m the number of chemical components, $\beta_{S,s}^i$ and $\beta_{S,l}^i$ the solid and liquid solutal expansion coefficients of component i, $C_s^i$and C_l^i mass fractions of component i in the solid and liquid, C_0^i the nominal composition of i, and p the pressure.

In the packed regions, the momentum equations in the axial and radial directions are

$$\frac{\partial}{\partial t}(\rho u) + \nabla \cdot \left(\rho \vec{V} u\right)$$

$$= \nabla \cdot (\mu_l \nabla u) - \frac{\mu_l}{K} u - \rho_l g \left[\beta_{T,l}(T - T_0) + \sum_{i=1}^{m} \beta_{S,l}^i \left(C_l^i - C_0^i\right)\right] \tag{2.4}$$

$$- \frac{\partial p}{\partial z}$$

and

$$\frac{\partial}{\partial t}(\rho v) + \nabla \cdot \left(\rho \vec{V} v\right) = \nabla \cdot (\mu_l \nabla v) - \frac{\mu_l}{K} v - \mu_l \frac{v}{r^2} - \frac{\partial p}{\partial r}. \quad (2.5)$$

The primary difference between the two sets of equations is the viscous terms for the solid particles and solid buoyancy forces that are included in the slurry region, and the permeability of the rigid mush, K, which affects the rigid solid only, defined using the Blake-Kozeny relationship [64–68]:

$$K = \frac{\lambda^2}{180} \frac{(1 - g_s)^3}{g_s^2}, \quad (2.6)$$

The model for equiaxed solidification works by using the first pair of equations for any control volumes that have not yet packed, and the second set for control volumes that have. This form of the equations, however, is not convenient for application of all the grain attachment models that will be discussed here. Therefore, they have been collapsed into a single pair of momentum equations for the axial and radial directions, each of which is valid over the entire domain:

$$\frac{\partial}{\partial t}(\rho u) + \nabla \cdot \left(\rho \vec{V} u\right) = \nabla \cdot \left(\mu_l \frac{\rho}{\rho_l} \nabla u\right) - \frac{\partial p}{\partial z} + (1 - F) S^z_{slurry} + F S^z_{rigid}, \quad (2.7)$$

and

$$\frac{\partial}{\partial t}(\rho v) + \nabla \cdot (\rho \vec{V} v) = \nabla \cdot \left(\mu_l \frac{\rho}{\rho_l} \nabla v\right) - \mu_l \frac{\rho}{\rho_l} \frac{v}{r^2} - \frac{\partial p}{\partial r} + \ (1 - F) S^r_{slurry} + F S^r_{rigid}. \tag{2.8}$$

The source terms S^z_{slurry}, S^z_{rigid}, S^r_{slurry}, and S^r_{rigid} are simply collections of source terms from Equation (2.2) through (2.5) based on which portion of the domain (slurry or rigid) and which direction (z or r) they pertain to:

$$\begin{aligned} S^z_{slurry} = &-\nabla \cdot \left(\mu_l \frac{\rho f_s}{\rho_l} \nabla u_s\right) + \nabla \cdot (\bar{\mu}_s g_s \nabla u_s) + g_s \Delta \rho g - \nabla \cdot \left[\frac{\rho f_s}{f_l} (\vec{V} - \vec{V}_s)(u - u_s)\right] \\ &- g_s \rho_s g \left[\beta_{T,s}(T - T_0) + \sum_{i=1}^{n} \beta^i_{S,s}\left(C^i_s - C^i_0\right)\right] \\ &- g_l \rho_l g \left[\beta_{T,l}(T - T_0) + \sum_{i=1}^{n} \beta^i_{S,l}\left(C^i_l - C^i_0\right)\right], \end{aligned} \tag{2.9}$$

$$S^z_{rigid} = -\frac{\mu_l}{K} \frac{\rho}{\rho_l} u - \rho_l g \left[\beta_{T,l}(T - T_0) + \sum_{i=1}^{n} \beta^i_{S,l}\left(C^i_l - C^i_0\right)\right], \tag{2.10}$$

$$S^r_{slurry} = -\nabla \cdot \left(\mu_l \frac{\rho f_s}{\rho_l} \nabla v\right) + \mu_l \frac{\rho f_s}{\rho_l}_s \frac{v}{r^2} + \nabla \cdot (\bar{\mu}_s g_s \nabla v) - \bar{\mu}_s g_s \frac{v}{r^2}\ , \tag{2.11}$$

and

$$S^r_{rigid} = -\frac{\mu_l}{K}\frac{\rho}{\rho_l}v. \tag{2.12}$$

The weighting function, F, introduced in Equations (2.7) and (2.8) is used to toggle the various source terms depending on the conditions of the particular control volume. The value of F varies from zero to one, with zero representing the slurry region and one the rigid solid region. The weighting function F may be written in terms of the packed fraction, P, of a given control volume using any appropriate functional form. Here, in order to avoid introducing a large number of new variables, a simple power law form is implemented:

$$F = P^n, \tag{2.13}$$

where n is called the weighting exponent. The value of P is set by the grain attachment model as discussed in §2.2.1. The justification for the use of a weighting function is also explained in §2.2.1.3.

Species conservation for a given alloying element i is given by

$$\begin{aligned}\frac{\partial}{\partial t}\left(\rho C^i\right) + \nabla\cdot\left(\rho\vec{V}C^i\right) \\ = \nabla\cdot\left(\rho f_l D\nabla C^i\right) + \nabla\cdot\left(\rho D\nabla\left(C_l^i - C^i\right)\right) \\ - \nabla\cdot\left(\rho f_s\left(\vec{V} - \vec{V}_s\right)\left(C_l^i - C^i\right)\right),\end{aligned} \tag{2.14}$$

where C^i is the mixture composition with respect to element i and D is mass diffusivity.

Energy conservation is written in terms of temperature [69]:

$$\frac{\partial}{\partial t}(\rho c T) + \nabla \cdot \left(\rho c T \vec{V}\right) = \nabla \cdot (k \nabla T) - \frac{\partial}{\partial t}\left(\rho f_l L_f\right) - \nabla \cdot \left(\rho \vec{V} f_l L_f\right) - \nabla \cdot \left[\rho f_s L_f \left(\vec{V} - \vec{V_s}\right)\right], \tag{2.15}$$

where c is the constant pressure specific heat, L_f the latent heat of fusion, and k is a mixture thermal conductivity, calculated using a volume weighted harmonic mean of the solid and liquid contributions:

$$k = \frac{k_s k_l}{g_s k_l + g_l k_s}. \tag{2.16}$$

2.2 Supplemental Relationships

2.2.1 Grain Attachment Models

The purpose of a grain attachment model is to determine whether the solid within a cell is to be treated as free-floating solid particles or as a permeable, rigid structure. These models can be generally classified into two types: discrete and continuum. All past attachment models for the mixture formulation of the governing conservation equations fall into the former category, in which each cell may only be fully packed or fully unpacked,

with no states in between. These models are implemented mathematically by only allowing the packed fraction of a cell P be equal to zero or one. It will be shown in CHAPTER 5 that these types of schemes produce significant numerical artifacts. To counteract these problems, a continuum model was developed in which the control volumes transition smoothly from free-floating to rigid solid, corresponding to values of P that vary continuously from zero to one. For all of the models presented here, grain attachment will depend on some critical volume fraction solid, $g_{s,c}$. The actual volume fraction that a given cell becomes packed at will be called the packing fraction, $g_{s,p}$.

2.2.1.1 The Constant Packing Fraction Model

The first and most common approach for equiaxed solidification, falling into the discrete type of grain attachment model, is the constant packing fraction (CPF) scheme, which assumes that the packing transition occurs at a critical volume fraction solid, $g_{s,c}$. Additionally, the CPF model requires that at least one of the neighboring control volumes is packed, so that any free-floating solid particles within the cell of interest have a rigid interface upon which to attach. Mathematically, this scheme may be written for the value of P in terms of the volume fractions solid of the cell of interest and the critical value as

$$P = \begin{cases} 0, if\ g_s < g_{s,c}\ or\ \sum P_{nb} = 0 \\ 1, if\ g_s \geq g_{s,c}\ and\ \sum P_{nb} \geq 1 \end{cases} \tag{2.17}$$

where P_{nb} is the packed fraction of the neighboring control volumes.

As Equation (2.17) clearly shows, the CPF model is discrete in that P may only take on values of zero of one. Furthermore, the packing fraction for each cell is simply equal to the critical value: $g_{s,p} = g_{s,c}$. This protocol is shown schematically in Figure 2.1.

It should be noted here that columnar solidification is simply a special case of the CPF model in which $g_{s,c} = g_{s,p} = 0$. The solid velocity is therefore forced to be equal to zero throughout the domain (§2.2.2).

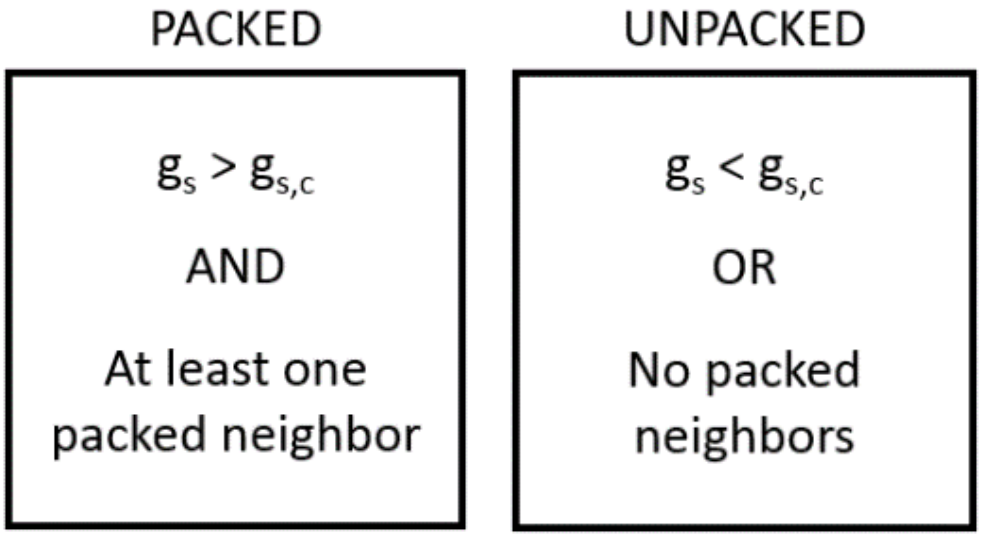

Figure 2.1: Schematic of the constant packing fraction (CPF) approach for (a) a packed cell and (b) a cell that remains unpacked.

2.2.1.2 Velocity Based Packing Models

The simplicity of the CPF approach is attractive, and it has been implemented into a variety of solidification models. However, it does not consider the effects of the local velocity field, which may either push free-floating grains into the rigid interface or carry them away. To add consideration of the velocity field, Vušanović and Krane [58] proposed a simple velocity-based model. The basis of this model is to determine packing of the cell of interest by considering the condition of the cell in the downstream direction. If the downstream cell is packed and has a volume fraction solid above a critical value, $g_{s,c}$, then the cell of interest is considered packed. Mathematically, the value of P for the cell of interest may be expressed as

$$P = \begin{cases} 0, if\ g_{s,ds} < g_{s,c}\ or\ P_{ds} = 0 \\ 1, if\ g_{s,ds} \geq g_{s,c}\ and\ P_{ds} = 1 \end{cases} \tag{2.18}$$

where $g_{s,ds}$ is the volume fraction solid of a given downstream control volume with corresponding packed fraction P_{ds}. Again, P may only take on values of either zero or one, making this a discrete attachment scheme.

The velocity based approach is shown schematically in Figure 2.2. Because grain attachment is dependent on the local solid velocity field, the solid fraction at which a cell packs is not equal to the critical solid fraction, as is true for the CPF case, and furthermore, varies on a cell-by-cell basis. For the sake of comparison to the other attachment schemes,

an average packing fraction, $\bar{g}_{s,p}$, will be used to describe the packing in these cases, calculated by simply using the arithmetic mean of the packing fractions within the domain.

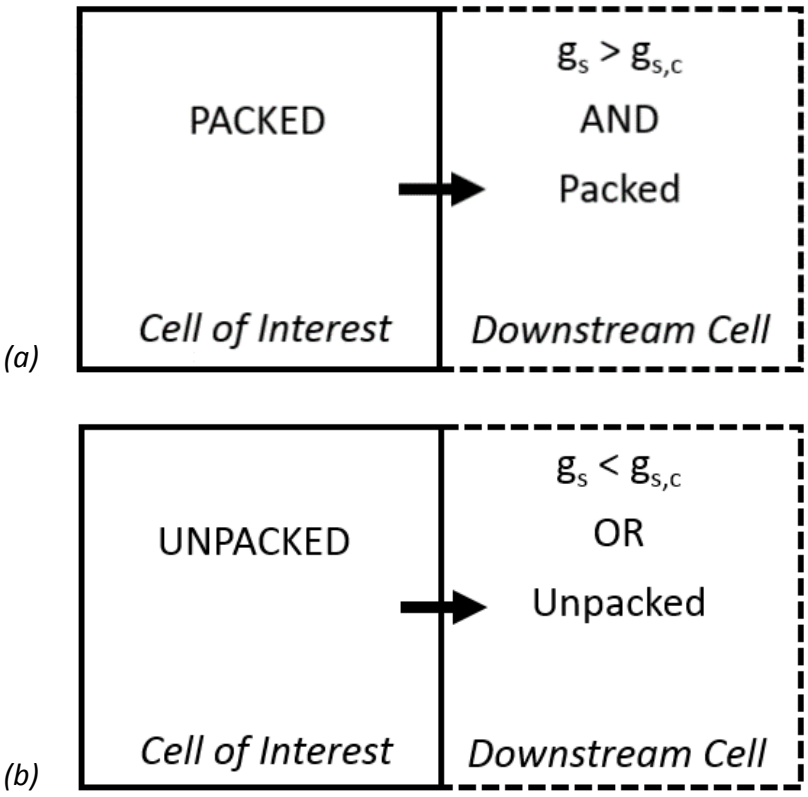

Figure 2.2: Schematic of velocity based packing logic in which (a) the cell of interest becomes packed and (b) the cell of interest remain unpacked.

The packing of free-floating solid particles is tied to the local velocity field through the methodology for determining the downstream cell or cells based on the solid velocity components that are located on the cell faces. The challenge in doing so is that the solid velocity at the interface between the cell of interest and a neighboring packed cell is, by

definition, zero. Therefore, some scheme must be used to approximate the velocity of the free floating solid within the cell of interest rather than on the staggered velocity grid. Vušanović and Krane circumvented this problem by using the arithmetic mean of the solid velocities in each direction. The larger magnitude of the two resulting velocity vectors was then used to determine the downstream cell. This approach will therefore be termed the average velocity method (AVM).

The AVM scheme is simple to implement, but ignores the existing mixture velocity that has already been calculated at the cell faces. A different approach is to calculate an apparent solid velocity at each face using the known mixture velocity, and Stokes' law, for the fraction solid in the cell of interest. In this case, because the reduced permeability of the interface with a packed control volume will significantly lower the mixture velocity at these points, it is best to ignore the magnitudes of the apparent solid velocities. Instead, only the direction of the apparent solid velocities is considered and the packing criterion shown in Figure 4 is applied to *any* cell that is downstream from the cell of interest (i.e. the corresponding apparent solid velocity flows out of the cell of interest). This approach is termed the face velocity method (FVM). The essential difference between these two methods is that the AVM tests only the cell downstream from the strongest solid velocity, while the FVM tests *all* downstream cells.

These two velocity-based approaches may be summarized as follows:

Average Velocity method (AVM)

1. Calculate the arithmetic mean across the cell of interest for each of the of r and z components of the solid velocity
2. The larger of the two averaged solid velocity vectors points to the downstream cell upon which the packing logic is applied

Face Velocity Method (FVM)

1. Calculate an apparent solid velocity at each face of the cell of interest from Stokes' law, the face mixture velocity, and g_s of cell of interest
2. Apply the packing logic to *any* cell that is downstream, i.e. has an apparent solid velocity flowing into it

Figure 2.3 shows a schematic representation of the two velocity-based methods described above. Interactions between unattached particles may still cause dendrite coalescence, so the velocity-based methods also require an upper limit to the solid fraction of the slurry region to be applied in the same way as the constant packing fraction approach. An obvious and practical choice for this upper limit is $g_{s,c}$, so that any cell with a volume solid fraction high enough to trigger packing of neighboring cells will itself be packed, ensuring a smooth movement of the rigid interface through the domain. The

consequence of using too high of an upper limit is that the packing of one cell may trigger an avalanche of packing among many neighboring cells, creating instability in the model and unrealistic results.

2.2.1.3 A Continuum Attachment Model

The need for a continuum attachment scheme will be clearly demonstrated in CHAPTER 5, but the mathematical formulation and some of its details will be presented here without motivation. The main concept behind the continuum attachment model is that the value of P may take on any value between zero and one. Of course, this requires some formulation for determining the value of P. Here, the form selected is a simple linear variation over a given range of solid fractions with the upper limit being the critical solid fraction and the range controlled by a new parameter, the packing range, Δg_s:

$$P = \begin{cases} 0, if\ g_s < g_{s,c} - \Delta g_s \\ 1 - \dfrac{g_{s,c} - g_s}{\Delta g_s}, if\ g_{s,c} - \Delta g_s < g_s < g_{s,c} \\ 1, if\ g_s > g_{s,c} \end{cases} \tag{2.19}$$

The purpose of this attachment scheme is to allow a smooth transition between the free-floating and rigid solid regimes. However, while using a linear form for packed fraction of a given control volume is reasonable, giving a linear variation in the weighting of the source terms in the governing equations for momentum conservation may not be realistic due to large differences in the order of magnitude of the different terms.

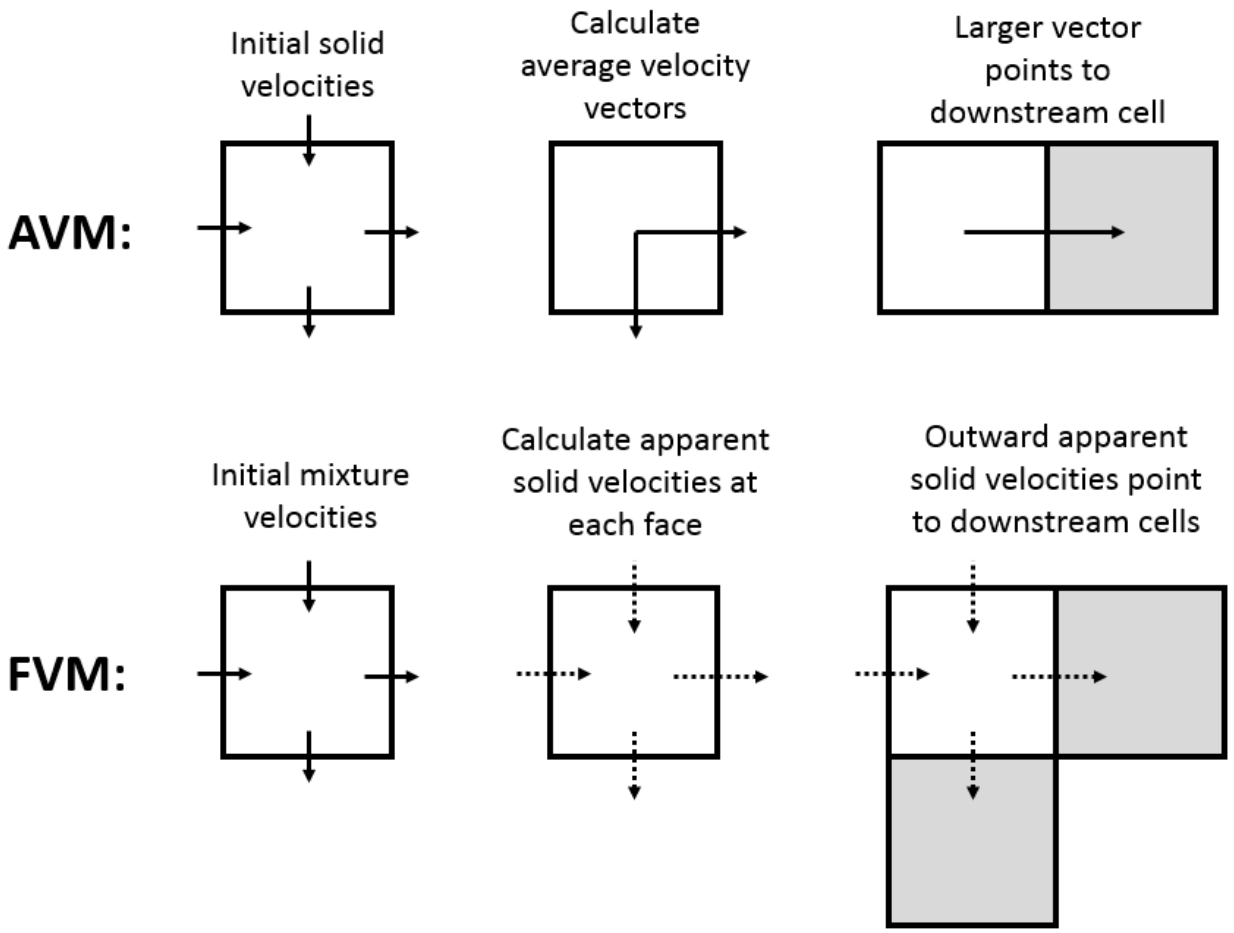

Figure 2.3: Schematic representation of the two velocity based packing schemes. The cell of interest is shown in white and the downstream cells to which the packing logic (Figure 2.2) will be applied are shown in gray.

In order to vary the manner in which the terms contribute to the behavior of the cells undergoing the transition between the free-floating and rigid regimes, a weighting function, F, is introduced. Because it is not immediately clear what the appropriate form of this function should be, a power law form was used, as given in Equation (2.13), as a simple way to control the shape of the function without introducing too many new parameters. A more detailed analysis of the relative orders of magnitude of the source terms and how the weighting exponent n affects the system is described in CHAPTER 6.

2.2.2 The Free-Floating Solid Model

As stated previously, the solid particles in suspension within the liquid metal are collectively treated as a pseudo-fluid, with a mixture viscosity based on the recommended formulation of Ishii and Zuber [70]:

$$\mu_m = \mu_l \left(1 - \frac{g_s}{g_{s,c}}\right)^{-2.5 g_{s,c}}, \tag{2.20}$$

where the mixture viscosity may also be expressed in terms of the associated volume fractions of each phase, $\mu_m = g_s \mu_s + g_l \mu_l$. The contribution of the solid pseudo-fluid to the viscosity is then

$$\mu_s = \frac{\mu_l}{g_s}\left[\left(1 - \frac{g_s}{g_{s,c}}\right)^{-2.5 g_{s,c}} - g_l\right], \tag{2.21}$$

and an average solid viscosity used in the momentum equations may be calculated by integrating over the majority of the solid fraction range prior to packing, as recommended by Vreeman [71]:

$$\bar{\mu}_s = \frac{1}{0.7 g_{s,c}} \int_0^{0.7 g_{s,c}} \mu_s d g_s. \tag{2.22}$$

The velocity of the solid particles is modeled using Stokes' law for spherical particles, modified by the packed fraction:

$$\vec{V}_s = (1 - P)\left(\frac{(1 - g_s)}{18\mu_m} \Delta\rho d^2 \vec{g} + \vec{V}_l\right), \tag{2.23}$$

where d is a representative particle diameter. The choice of using $(1 - P)$ as a multiplier for Stokes' law (as opposed to using the weighting function) does not affect the discrete attachment models. The impact of this decision on the continuum model will be discussed in CHAPTER 6.

2.2.3 The Thermodynamic Model

The fraction solid and local solid and liquid compositions are determined for a given cell using the instantaneous temperature and mixture composition, assuming

equilibrium (lever law) thermodynamics. For multicomponent systems (such as that used here), an expression for the liquidus surface must be known as a function of the mass fraction of each of the alloying elements, as well as the partition coefficients for each. The model works by first assuming a mass fraction solid of 0.5 and calculates the local liquid composition based on the known mixture composition and the relevant partition coefficients ($C^i = f_s C_s^i + f_l C_l^i$ and $k^i = C_s^i / C_l^i$). This liquid composition determines a temperature on the liquidus surface which is compared to the actual temperature of the control volume. If these values do not match, the guessed fraction solid is adjusted up or down appropriately, and the process is repeated until convergence.

2.3 Numerical Methods

The model is solved using standard finite volume techniques [72] on a uniform, rectangular, orthogonal, staggered grid using an implicit time stepping scheme. The SIMPLER algorithm is used to solve for the velocity and pressure fields. Advection terms are discretized using upwind differencing and the advection-like source terms in the species equation are discretized according to the recommendations of Vreeman and Incropera [73].

2.3.1 Interpolations for the Staggered Velocity Grids

In staggering the velocity grids, several important interpolations must be performed from the main control volumes onto the relevant grids for the momentum

equations. The first of these is the determination of the permeability for the rigid mush. In this case, the fraction solid is first interpolated linearly between the main control volumes, and permeability for the associated velocity cell is then calculated using this interpolated value and Equation (2.6).

The second issue is in determining the value of P in the velocity control volumes for the grain attachment models in equiaxed solidification (P is simply equal to unity at all times for columnar solidification). In the discrete models, because P may only be equal to zero or one, the assumption is that if either of the main control volumes shared by a given staggered cell are packed, then the staggered cell itself is packed. In the continuum model, since the packed fraction may take on any value between zero and one, it is linearly interpolated between the respective main control volumes.

2.3.2 The Transient Latent Heat Source Term

The highly non-linear nature of the transient latent heat source term in the temperature formulation of the energy equation (Equation (2.15)) requires special treatment. Here, the linearization scheme proposed by Voller and Swaminathan [74] is implemented and extended for multicomponent alloy systems. This method linearizes the source term into a form that may be readily incorporated into the standard finite volume discretization described by Patankar [72]. The form of the linearized source term is

$$S = S_p T_p + S_c \tag{2.24}$$

And is incorporated into the discretized governing equation:

$$\left(a_p - S_p\right)^k T_p^{k+1} = \left(\sum_{nb} a_{nb} T_{nb} + a_p^0 T_p^0 + S_c\right)^k \tag{2.25}$$

where $k+1$ is the current iteration level, p denotes the control volume of interest and nb its neighbors, a are discretization coefficients, and 0 superscript indicates the previous time step. If the solid and liquid specific heats are assumed equal, the contributions of the transient latent heat term to the source terms S_p and S_c are

$$S_p = -\rho L_f \frac{d\varepsilon}{dT} V_p \tag{2.26}$$

and

$$S_c = \rho L_f V_p \left(\left(f_l^0 - f_l^k\right) + \frac{d\varepsilon}{dT} \varepsilon^{-1}\left(f_l^k\right)\right) \tag{2.27}$$

where ε is the function relating the fraction liquid and temperature through the phase diagram, and $\varepsilon^{-1}\left(f_l^k\right)$ is the temperature determined by that relationship, evaluated at the fraction liquid of the previous iteration. This model calculated the change in fraction liquid between temperatures T^{k+1} and T^k and then add this value to f_l^k. At each

iteration, this method decouples the strict relationship between temperature and fraction liquid, so that the assumption of equilibrium solidification conditions is not truly satisfied until convergence.

One challenge in implementing this linearization scheme is the determination of $d\varepsilon/dT$. For binary alloys this can be determined analytically from the phase diagram. The form of ε for binary alloys is

$$\varepsilon = \frac{C_0}{A(T - T_m)} - \frac{1}{Am_s} \tag{2.28}$$

where T_m is the melting temperature of the pure material, m_l and m_s are the slopes of the liquidus and solidus lines, respectively, and

$$A = \frac{1}{m_l} - \frac{1}{m_s} \tag{2.29}$$

The derivative of this relationship with respect to temperature is

$$\frac{d\varepsilon}{dT} = \frac{-C_0}{A(T - T_m)^2} \tag{2.30}$$

For multicomponent alloys, the determination of the fraction liquid is performed as described in §2.2.3. In this case, a simple analytical expression for the derivative is not forthcoming. Instead, it is approximated numerically:

$$\frac{d\varepsilon}{dT} = \frac{\varepsilon(T^k + 0.005) - \varepsilon T^k}{0.005} \tag{2.31}$$

2.4 System Description

The alloy used for this work is AA7050, a high-strength aerospace aluminum alloy that is commonly cast commercially in a grain refined conditions. Properties used for this alloy are shown in Table 2.1. The domain is axisymmetric with dimensions and thermal boundary conditions given in Figure 2.4. For the momentum and species equations, the outer boundaries were assumed no-slip and impermeable, respectively, with symmetry conditions applied at the centerline.

Table 2.1: Properties of AA7050 taken from [71,75–77].

Property	**Value**	**Property**	**Value**
Initial Comp. Zn, C_0^{Zn} (wt. fr.)	0.062	Density, ρ (kg/m^3)	2515
Initial Comp. Cu, C_0^{Cu} (wt. fr.)	0.023	Density Difference, $\Delta\rho$ (kg/m^3)	229.1
Initial Comp. Mg, C_0^{Mg} (wt. fr.)	0.0225	Specific heat, c (J/kg-K)	1141
Liq. solutal exp. coef. Zn, $\beta_{S,l}^{Zn}$	-0.65	Thermal cond. solid, k_s (W/m-K)	149.4
Liq. solutal exp. coef. Cu, $\beta_{S,l}^{Cu}$	-0.75	Thermal cond. liquid, k_l (W/m-K)	83.2
Liq. solutal exp. coef. Mg, $\beta_{S,l}^{Mg}$	0.53	Latent heat, L_f (J/kg)	3.76x10^5
Sol. solutal exp. coef. Zn, $\beta_{S,s}^{Zn}$	-1.43	Liquid mass diffusivity, D (m^2/s)	8.0x10^{-9}
Sol. solutal exp. coef. Cu, $\beta_{S,s}^{Cu}$	-2.01	Liq. dynamic viscosity, μ_l (kg/m-s)	1.3x10^{-3}
Sol. solutal exp. coef. Mg, $\beta_{S,s}^{Mg}$	0.31	k^{Zn}	0.39
Liq. thermal exp. coef., $\beta_{T,l}$ (K^{-1})	2.29x10^{-5}	k^{Cu}	0.09
Sol. thermal exp. coef., $\beta_{T,s}$ (K^{-1})	1.5x10^{-5}	k^{Mg}	0.29

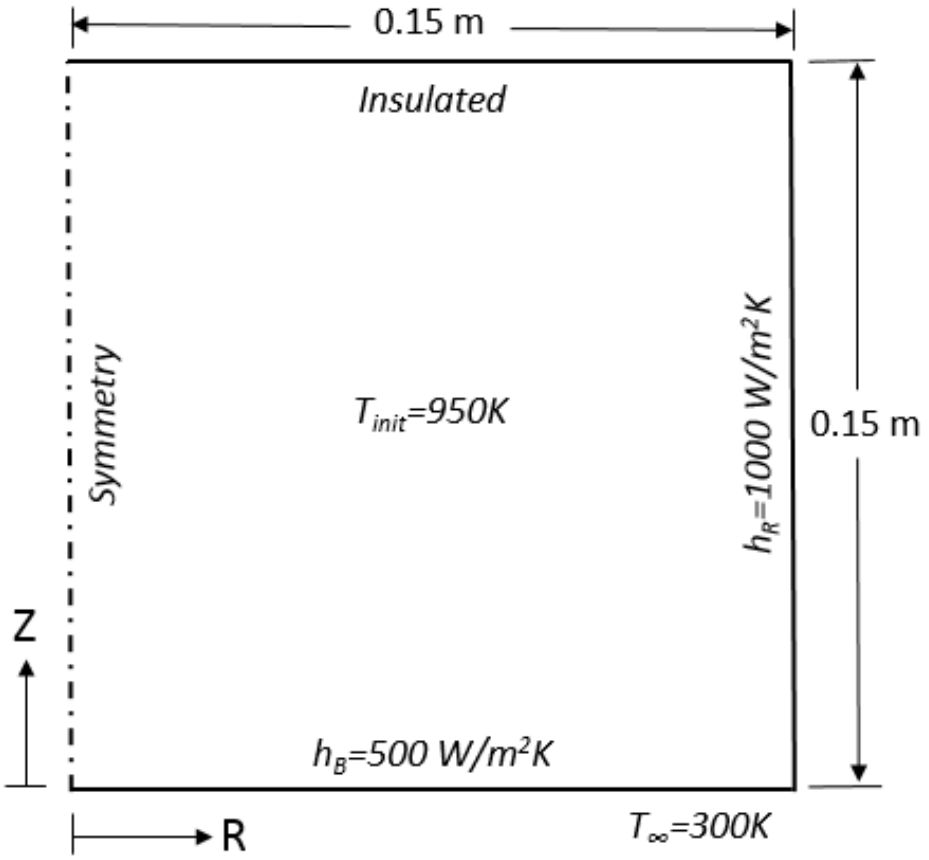

Figure 2.4: System geometry and boundary and initial conditions.

Only the three main chemical components of AA7050 (Zn, Cu and Mg) were explicitly modeled. The liquidus surface for the quaternary system is described by:

$$T_{liq} = 933.15 + 0.63 - 174.16C_l^{Zn} - 271.55C_l^{Cu} - 494.68C_l^{Mg}, \quad (2.32)$$

where the temperature is in Kelvin, the compositions in weight fraction, the first term is the melting temperature of pure aluminum, and the second accounts for the addition of elements not tracked by the model (Zr, Fe, Si, Ti, Cr, and Mn). The solid surface is related to the liquidus surface by the relevant partition coefficients as give in Table 2.1. Equation (2.32) and the partition coefficients were determined with Thermo-calc™ using the TCAL1 database [78]. While the three primary alloying elements were tracked by the model for their contributions to the alloy thermodynamics and solutal buoyancy, results will only be presented for Zn because the other elements will show the same trends.

2.5 Quantification of Macrosegregation

In order to quantitatively compare a large number of cases, the three-parameter Weibull distribution will be used to describe the final composition fields. Fitting the Weibull distribution to the final composition field (done here in terms of Zn) is described by Fezi, Plotkowski and Krane [79]. The volume distribution function is given by

$$VDF_w(C) = \frac{\alpha}{\beta}\left(\frac{C-\gamma}{\beta}\right)^{\alpha-1} exp\left(-\left(\frac{C-\gamma}{\beta}\right)^{\alpha}\right), \tag{2.33}$$

where α is the shape parameter, β the scale parameter, and γ the threshold value. The VDF is the derivative of the corresponding cumulative volume distribution function:

$$CVDF_W(C) = 1 - exp\left(-\left(\frac{C-\gamma}{\beta}\right)^{\alpha}\right). \quad (2.34)$$

The distribution parameters are calculated by first generating a cumulative volume distribution from the final composition field predicted by the simulation. This new dataset is calculated by first ordering all of the compositions in the domain from least to greatest and recording their corresponding volumes. For each unique composition, the corresponding point on the cumulative volume distribution is equal to the sum of the volumes of all cells containing a lower composition normalized by the domain volume. For a given threshold value, the shape and scale parameters are found from this new data set using the least squares method. Possible threshold values are then searched from zero to minimum composition using a small increment (e.g. 10^{-5}) to find the value that gives the smallest RMS error between the data and the fitted cumulative volume distribution function.

Once the parameters that describe the distribution have been found, the metric of interest is the normalized Weibull deviation, W:

$$W = \frac{\sigma_W}{C_0} = \frac{\beta}{C_0}\left[\Gamma\left(1+\frac{2}{\alpha}\right) - \Gamma^2\left(1+\frac{1}{\alpha}\right)\right]^{1/2}, \quad (2.35)$$

where σ_W is the deviation of the three-parameter Weibull distribution and Γ is the gamma function

$$\Gamma(z) = \int_0^\infty t^{z-1} e^{-t} dt. \tag{2.36}$$

The normalized Weibull deviation is a measure of the width of the fitted distribution for a given alloying element, and therefore, is a useful description of the macrosegregation within the casting, where higher values indicate a wider range of compositions. This approach is not probabilistic in nature, but the three-parameter Weibull distribution is used here simply as a convenient function to which to fit the volume weighted collection of compositions within the domain.

CHAPTER 3. ON THE NUMERICAL PREDICTION OF FRECKLES IN COLUMNAR SOLIDIFICATION

3.1 Introduction

Freckles are a type of macrosegregation defect characterized by solute enriched streaks of equiaxed grains found in otherwise columnar structures. These defects have a detrimental effect on the mechanical properties of the resulting solidified component and as a result, as described in §1.2.1, significant effort has been put forth to understand the mechanism behind freckle formation and to develop a quantitative criterion to predict their occurrence. Unfortunately, to date, a satisfactory criterion that can be used for any alloy or system geometry has not been found. One avenue towards better understanding the mechanisms for freckle formation and development of improved criteria for their prediction is the use of numerical solidification simulations.

The focus of this chapter is to understand the initiation and propagation of freckles specifically in numerical simulations, in order to determine their relevance to physical castings, and if necessary, to suppress the formation of erroneous predictions. While the mechanisms causing freckle formation and growth in simulations are similar to those observed experimentally, it will be shown here that aspects of the numerical methods have an unacceptably large influence on these phenomena. Therefore, using predictions to establish a quantitative criterion for freckle formation in physical systems is, at best,

fraught with uncertainty. This work will argue that the best approach for designing such a physical criterion is to couple freckle-free simulations with experimental observation. It will be shown that carefully controlling the convergence of these simulations is necessary for such an approach, and a recommendation for an appropriate convergence criterion is made.

3.2 Grid Dependence of Initial Simulations

To begin with, the grid dependence of simulations with a strict convergence criterion will be examined. In this case, the rate of convergence is controlled by the energy equation to which a normalization factor equal to the alloy freezing range and a tolerance of $1x10^{-5}$ was applied. This convergence scheme is proposed here without rationale, but will be discussed in detail in §3.5. The results of these simulations for three different grid sizes are shown in Figure 3.1. While freckles are mostly suppressed in coarse grids, some begin to develop as the grid is refined, although even at their most severe, the difference in composition from the surrounding metal is small relative to total macrosegregation in the domain. The freckles shown in Figure 3.1 propagate downwards relative to the motion of the solidification front, which proceeds inward from the outer radius and up from the bottom. This result is physically realistic considering that the primary alloying element in AA7050 is Zn, which is denser than Al. Solutal buoyancy, therefore, will aid the downward thermal buoyancy. Downward facing freckles such as these have been reported for Al-Cu alloys [7]. Of course, the opposite is often found when upward solutal buoyancy

dominates the combined thermosolutal convection, as is sometimes the case in nickel-based superalloys and the often studied aqueous ammonium chloride system [11]. The trend of increasing channel severity with decreasing grid size is consistent with observations of Li *et al.* [29] who found that A-segregates in a simulation of large ingot casting for Fe-0.45wt.%C became more pronounced as the grid was refined.

3.3 The Effect of Iterations on the Mechanism of Freckle Formation

Figure 3.1 demonstrates the susceptibility of the present system to freckle formation and shows their sensitivity to the grid spacing, but the channels in this case are not significant relative to the overall segregation of the ingot. In order to study the mechanism of their formation more easily, it is necessary to exaggerate their presence. This can be done using the strategy of Vušanović and Voller [28] of limiting the number of iterations per time step in order to introduce noise to the system in the form of convergence residuals that may act to seed channel development. To test this approach, the present model was hard-wired to perform various predetermined numbers of iterations per time step throughout the process. The final Zn composition plots for iteration levels from four to six are shown in Figure 3.2 for an 80x80 numerical grid. Clearly, when large amounts of numerical noise are introduced to the system by limiting convergence, the result is a significant increase in channel severity. This effect is quickly reduced as the number of iterations increases. A larger number of cases are summarized in Figure 3.3, which shows the normalized Weibull deviation for the final Zn composition

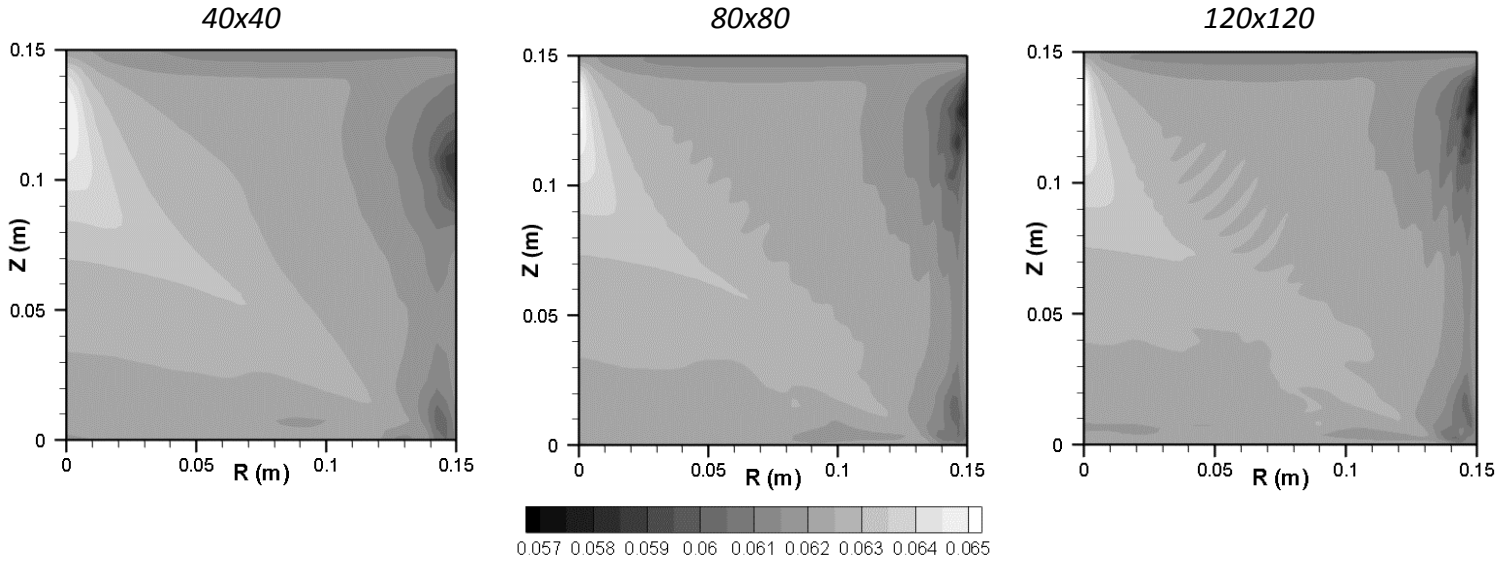

Figure 3.1: Final Zn composition fields for the base model at various grid sizes with a convergence criterion for the energy equation that uses the alloy freezing range as a normalization factor and a tolerance of $1x10^{-5}$.

field over a range of iterations per time step. At low iteration levels, the overall segregation is dominated by freckles, and the distribution of compositions reflects this. However, as the number of iterations increases, the freckles are quickly suppressed and only the general segregation pattern remains. Further iterations beyond about 20 do not significantly change the final composition field.

One qualification must accompany these results, in that the meaning of an iteration is subject to the details of the numerical solver. In the present model, a line-by-line tridiagonal matrix algorithm (TDMA) was used to solve the discretized equations. Included in the solution procedure are a great number of parameters, such as the sequence of sweep directions and use of under-relaxation factors, that may be tuned for optimal computation time. The values of these parameters do not affect the converged solution, but do change the path to this solution. The number of iterations for each result are therefore not necessarily representative of other similar models. However, the general trends are not affected by changes in solution procedure, so exact values of these solver parameters are not presented further in the interest of keeping the discussion as general as possible. The reason for the change in freckle appearance shown in Figure 3.2 is that additional iterations improve the accuracy of the solution to the highly non-linear governing equations. Using too few iterations leaves behind convergence residuals. These residuals are carried to the next time step and likely produce instabilities that, when added to by residuals in subsequent time steps, are able to grow into channels with significant deviations in the local composition. This mechanism fully explains the findings

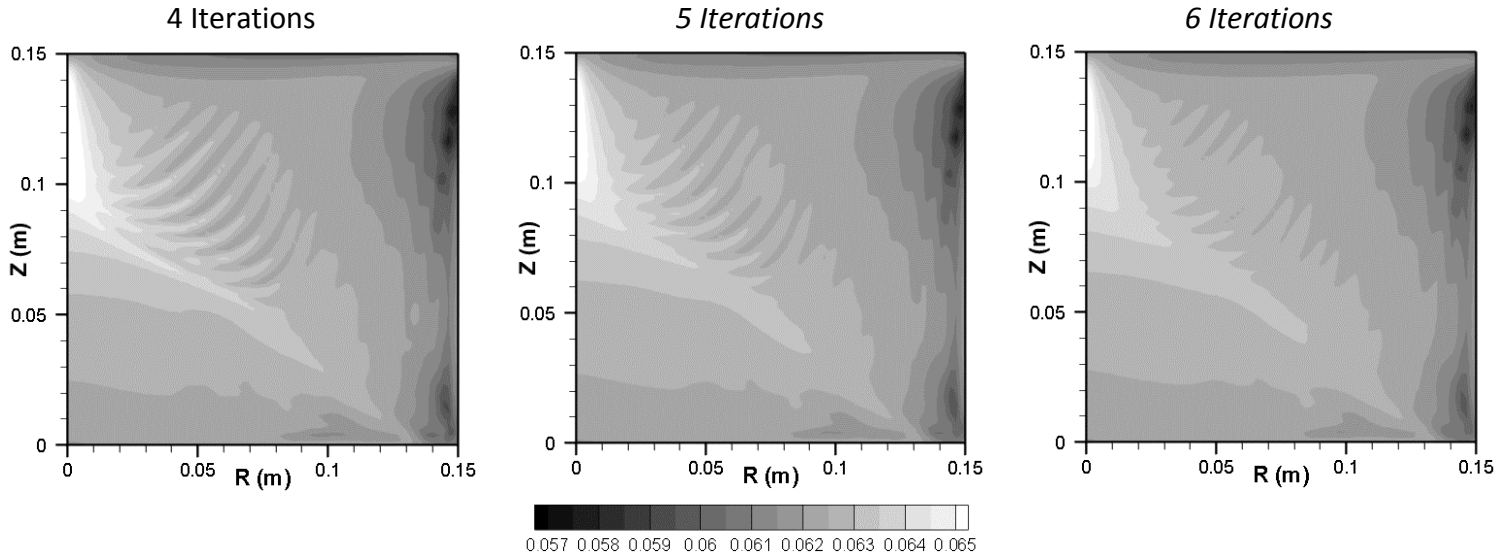

Figure 3.2: Final Zn composition fields for simulations with various numbers of iterations per time step. Grid spacing is 80x80 in all cases.

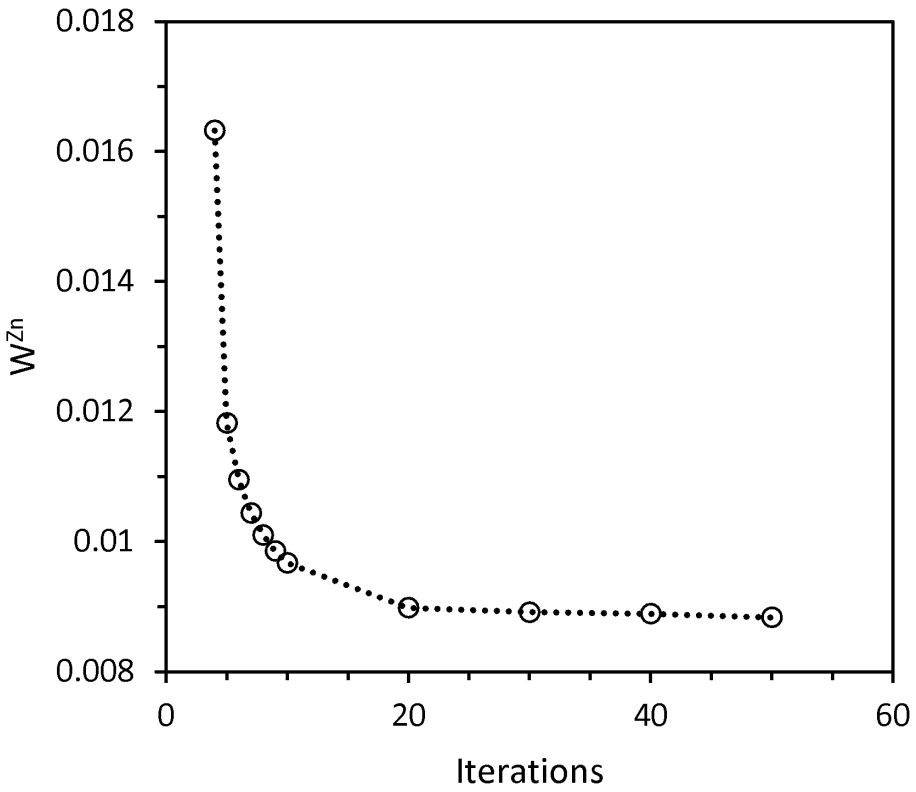

Figure 3.3: Normalized Weibull deviation for the final Zn composition field as a function of number of iterations per time step.

by Vušanović and Voller [28], in which the solution was limited to twenty iterations per time step in all cases. When using an implicit scheme, this limit might have prevented proper convergence in any of the governing equations. In the hybrid scheme, they used an explicit time step discretization for the energy and species equations so that they could obtain a solution with smaller residuals. This approach means that only the momentum equations, which were still solved implicitly, could be prevented from converging while the unchanged values of temperature and composition also helped speed convergence.

Thus, an increase in stability was observed, although channel formation was not eliminated.

Here, having introduced excessive numerical noise to exacerbate freckle formation, the mechanism of the transient channel formation may be investigated. Figure 3.4 shows the Zn composition fields and flow patterns for two different numbers of iterations at intermediate times during the process. Streamlines were selected to show flow through the outer part of the mushy zone, indicated by iso-solid fraction lines (in white) at 0.0025 and 0.01. Note that for different numbers of iterations, changes in macrosegregation impact the solidification time through the coupling between the species equations and the thermodynamic model. Therefore, similar times in the process cannot be compared directly. Instead, the location of the solidification front has been roughly matched for cases with 4 and 10 iterations per time step.

At four iterations, there are “ripples” in the streamlines that pass through the outer edge of the mushy zone, indicating changes in velocity (streamlines that are closer together indicate faster flow rates). These ripples appear to be aligned with the alternating regions of high and low composition, which in turn, correspond to variations in the solid fraction field. At earlier times (120 s), the flow is smoother, but the ripples build up over subsequent time steps. When the number of iterations per time step is increased to ten, these instabilities in the flow are mostly damped, associated with a significant decrease in the level of segregation within the channels.

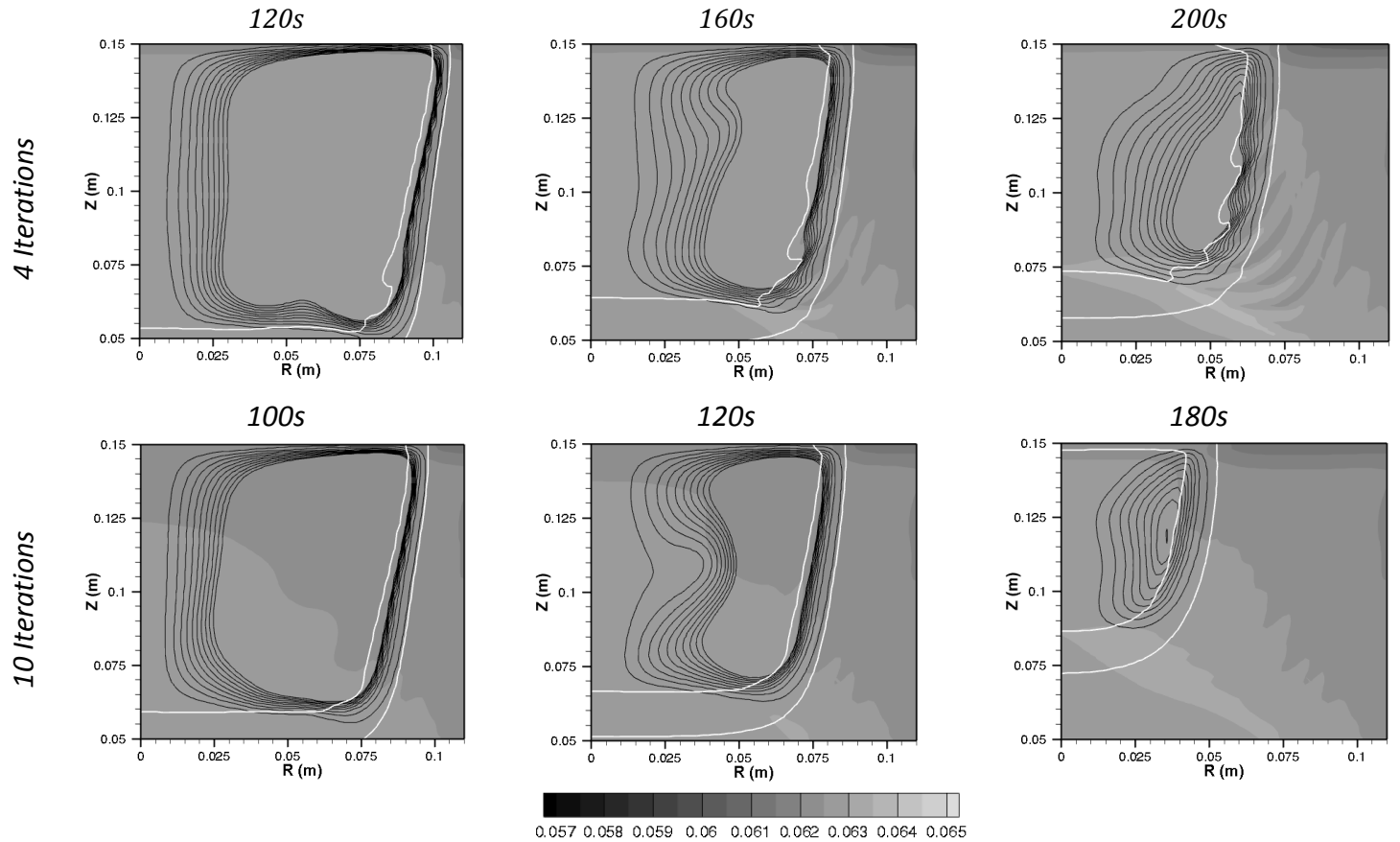

Figure 3.4: Comparison of flow and Zn composition fields (in weight fraction) for simulations with 4 and 10 iterations per time step for the portion of the domain where freckles appear. Streamlines are shown in black and are clockwise from 10^{-4} to 10^{-3} kg/s, selected to show the flow at the edge of the mushy zone, advancing from the right and bottom and shown by the iso-solid fraction lines at 0.0025 and 0.02 in white.

The mechanism for the development of freckles is shown in greater detail for the simulation with only four iterations per time step in Figure 3.5. Channels are initiated by some protrusion in the solidification front, as is likely to be present in a solution that is not converged. Regions of higher solid fraction have a correspondingly lower permeability as described by the Blake-Kozeny permeability model. Fluid flows preferentially around areas of low permeability rather than through, resulting in the “rippled” streamlines present in Figure 3.4 and Figure 3.5a. The reason for the changes in the fraction solid do not occur in isolation, but rather, are intimately related to the local composition and flow field, all of which feed upon each other.

For alloying elements with a partition coefficient less than one (as is the case for the elements tracked here), solute is rejected into the liquid while the solid is depleted. The solid at the edge of the mush is stationary but permeable. The enriched liquid contained within is advected downstream, driven by the combined effect of thermal and solutal buoyancy, leaving behind the depleted solid. This fluid is replaced by flow from upstream, which generally consists of liquid that is nearer the nominal composition. The net result is that the neighboring downstream control volume is enriched while the solid protrusion is depleted. The direction of the flow and therefore the direction of propagation of the channel are determined by the thermosolutal buoyancy, the motion of the solidification front, and the associated local fluctuations in the permeability at the edge of the mushy region.

The flow, composition, and permeability at the edge of the mush are linked by the thermodynamic model. Cells with higher solute content will have a lower liquidus

temperature, and therefore, a lower solid fraction for a given temperature. This result is shown in Figure 3.5b. Here, the solid fraction is overlaid by a single iso-composition line (at a value slightly above the nominal alloy composition) enclosing the depleted regions. The lower composition obviously corresponds to the protrusions of solid into the bulk fluid flow, and subsequently, to the ripples in the streamlines shown in Figure 6a. This mechanism functions as a positive feedback loop in which protrusions cause further compositional differences, which affect the solid fraction, which then further affects the flow through the permeability term in the momentum equations.

As shown in Figure 3.6, the number of iterations per time step also affects the grid dependence. For both iteration levels, no channels are predicted for coarse grids. As the grids are refined, the lower iteration levels begin to predict severe freckles. While some instability is present in the higher iteration level for fine grids, the composition difference between channels is only about a tenth of a weight percent. The grid convergence of each of the iteration levels can be seen quantitatively in terms of the normalized Weibull deviation in Figure 3.7. For only four iterations, the solution is obviously not grid independent. However, the Weibull deviation is only slightly affected by the grid spacing for the higher number of iterations.

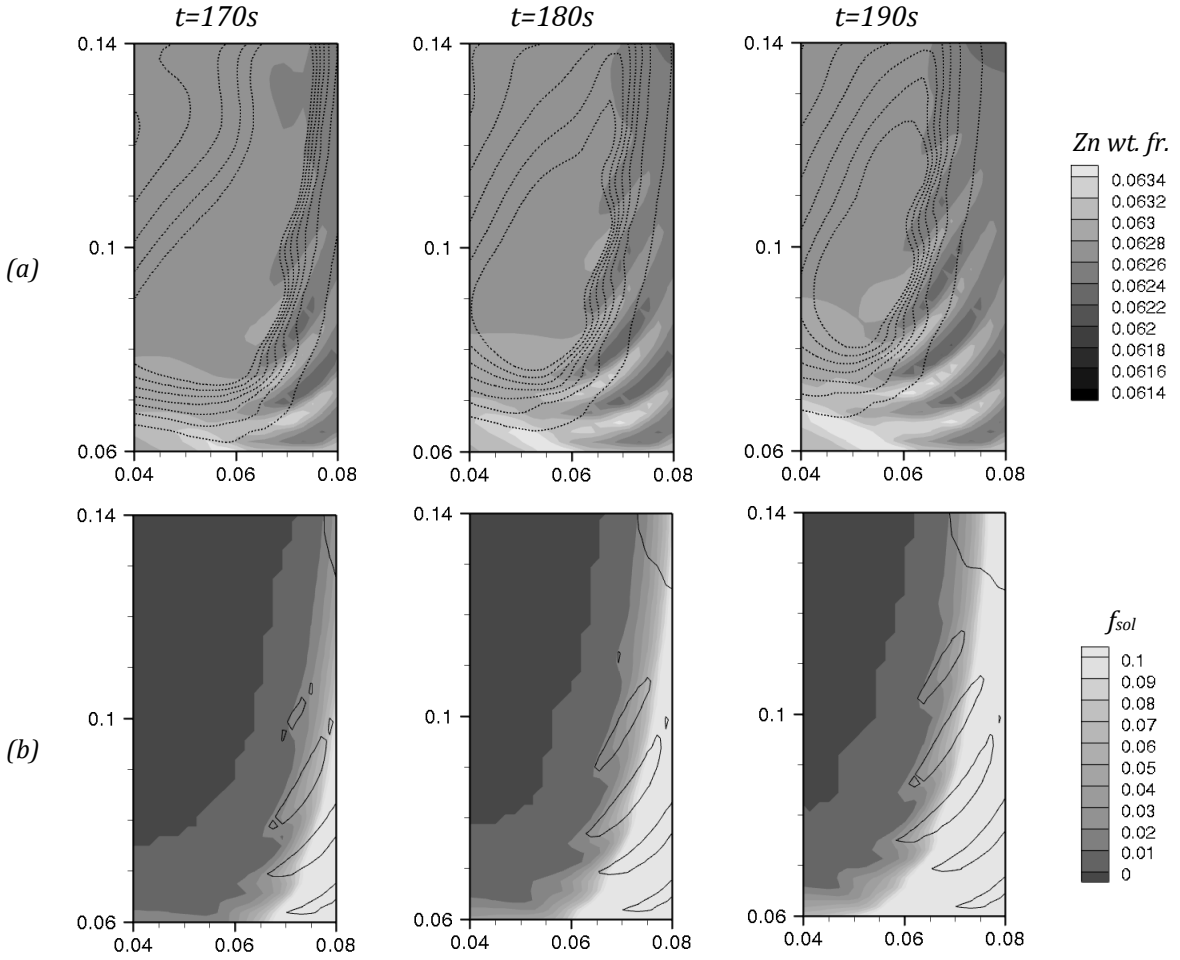

Figure 3.5: (a) Zn composition field showing streamlines from 0.0001 to 0.0013 kg/s through the edge of the mushy zone and (b) solid fraction field overlaid with a line showing Zn weight fraction of 0.0625 enclosing the most depleted regions. The plots are taken from a simulation limited to 4 iterations per time step.

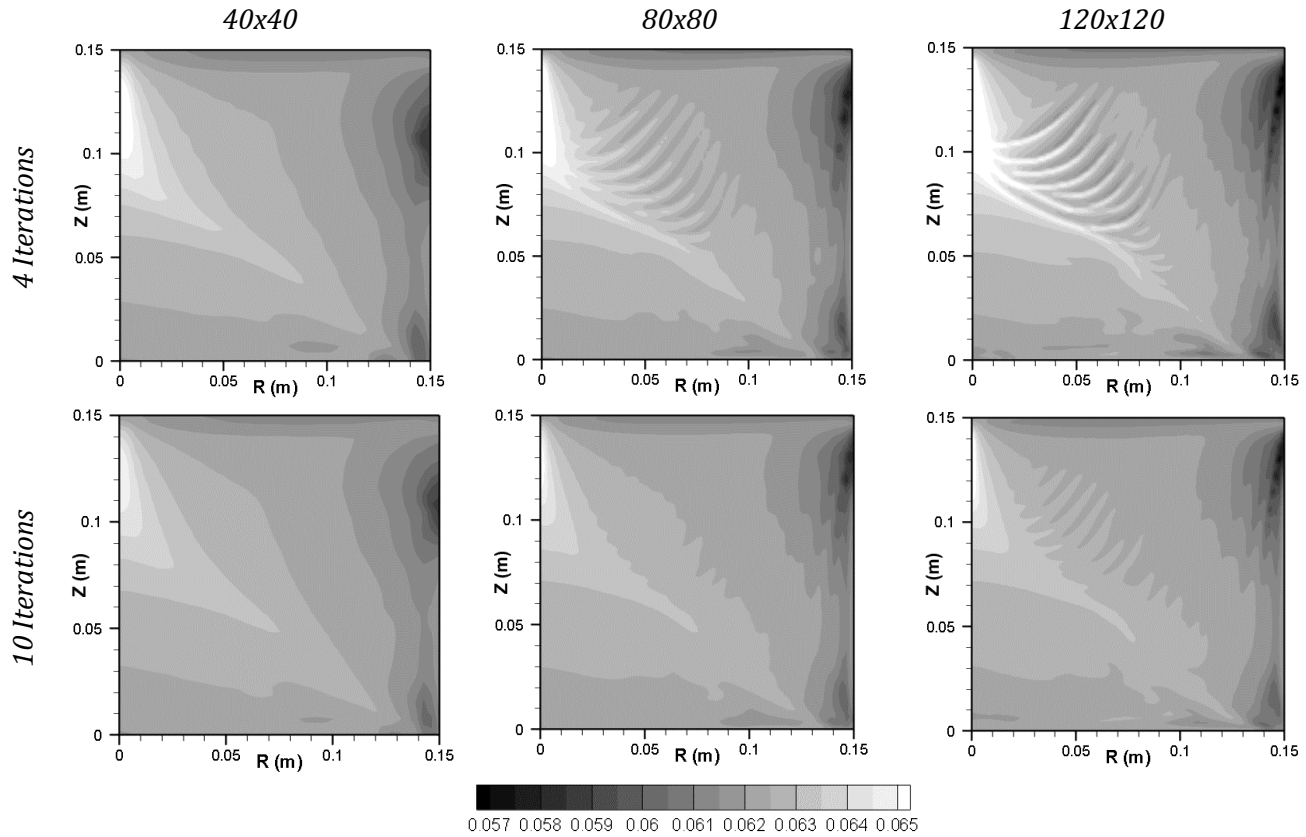

Figure 3.6: Final Zn composition fields (in weight fraction) at various levels of grid refinement for simulations with 4 and 10 iterations per time step.

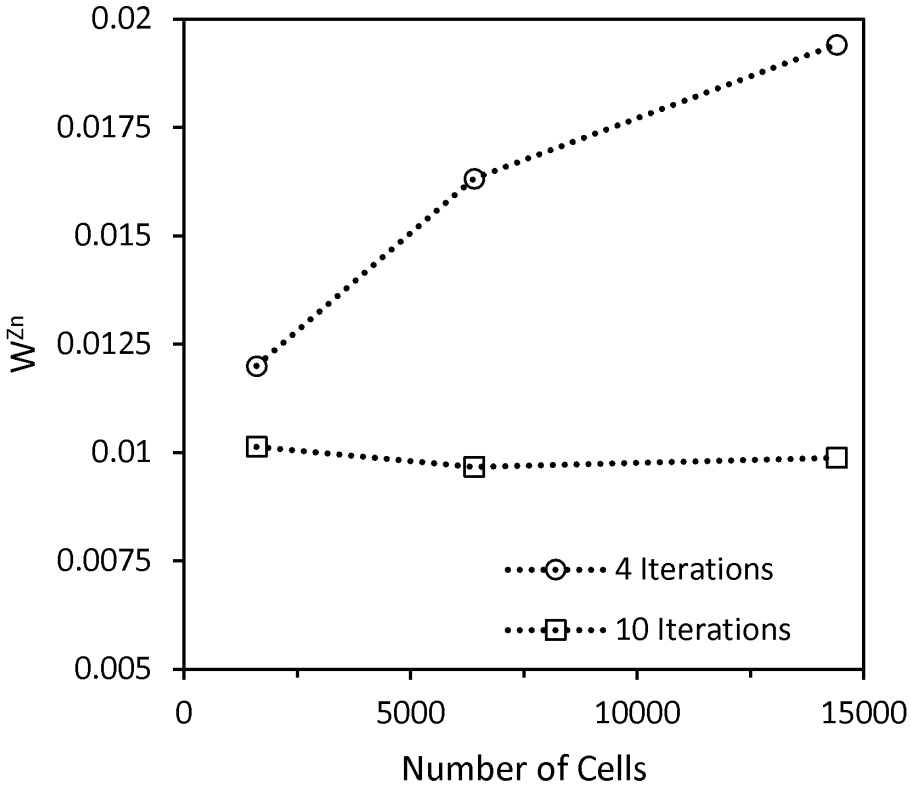

Figure 3.7: The grid dependence of the normalized Weibull deviation showing the zinc composition field is much greater when the number of iterations per time step is severely limited.

3.4 A Note on Length Scale and the Physical Relevance of Freckle Predictions

With the above description of the mechanism behind freckle formation in these simulations, the physical relevance of these predictions may be considered. It is clear that the susceptibility of the model to the growth of instabilities is a relevant physical phenomenon brought about by the coupling of the governing equations. These channels grow from some initial protrusion, which, in the case of numerical simulations, is brought about by small numerical perturbations which grow over time, and may be exacerbated by convergence residuals. If the macroscale phenomena are modeled accurately, then the

most important question is whether the protrusions in the numerical realm are representative of physical reality.

Unfortunately, the length scale of the instabilities in an actual casting may be as small as the dendrite arm spacing. Therefore, for a simulation to correctly predict the initiation of freckles, the cell size must be on a similar or smaller length scale. This conclusion is supported by Sung *et al.* [22] who found realistic predictions in their finite element model only when the element size was smaller than twice the dendrite arm spacing. However, using such a small numerical grid is computationally prohibitive for many commercial castings in which freckle formation may be of interest (e.g. steel ingot casting, electroslag remelting, vacuum arc remelting). There is a competition among the incipient channels, where the initial protrusions occur on the length scale of the dendrite arms but the eventual spacing of the freckles is much larger [11,80]. However, it is difficult at this time to determine the accuracy of simulations that cannot properly consider the initiation phase of freckle development.

Even if macroscale continuum models cannot explicitly predict freckles, there are still two approaches that may produce valid results. The first is the development of models on the dendrite arm length scale that explicitly consider the sharp solid-liquid interface rather than using a continuum solid fraction field. Models such as these have been developed [17,18], but while they do provide insight into freckle formation at the appropriate length scale, they are generally too computationally expensive to use for casting-scale simulations.

The second option is to use the local results of a macro-scale simulation as inputs to a freckle criterion. This approach allows for the comparatively efficient evaluation of large scale castings for their tendency to develop freckles. Unfortunately, while many different criteria exist, they are generally formulated for only a narrow range of casting conditions (usually directional solidification) and alloy compositions. Casting scale simulations such as the one presented here should be used in the future, in conjunction with appropriate validation experiments, to aid in the development of a new criterion that generally considers any alloy system, arbitrary solidification front geometry, and the effect of the bulk fluid flow. The primary concern of this type of simulation then, is to produce reliable predictions of the solidification conditions and bulk fluid mechanics that may be used as inputs for a given criterion, which may then be compared to the appearance of freckles in experimental castings. Therefore, casting-scale continuum simulations should seek to produce converged results in which the composition of any erroneous freckles does not obscure the more general trends in the composition field or other solidification phenomena of interest.

3.5 Recommendations on Obtaining a Converged Solution

To determine if erroneous freckles obscure more general trends in the composition field, Figure 3.8 shows a comparison of vertical Zn composition profiles at the mid-radius for three different iteration levels. With only four iterations per time step, a significant fluctuation in the local composition is seen from about 0.05 m (measured from the bottom of the cavity) to 0.1 m. Adding only one iteration per time step damps the

magnitude of these fluctuations and changes their location slightly. Increasing to ten iterations per time step produces a smooth composition profile. Interestingly, in all cases, the average trend in the composition from the bottom to the top of the domain is consistent. This finding suggests that perhaps even in cases where significant freckling is present, and if these channels are numerical in nature, the more general prediction of the simulation is still valid.

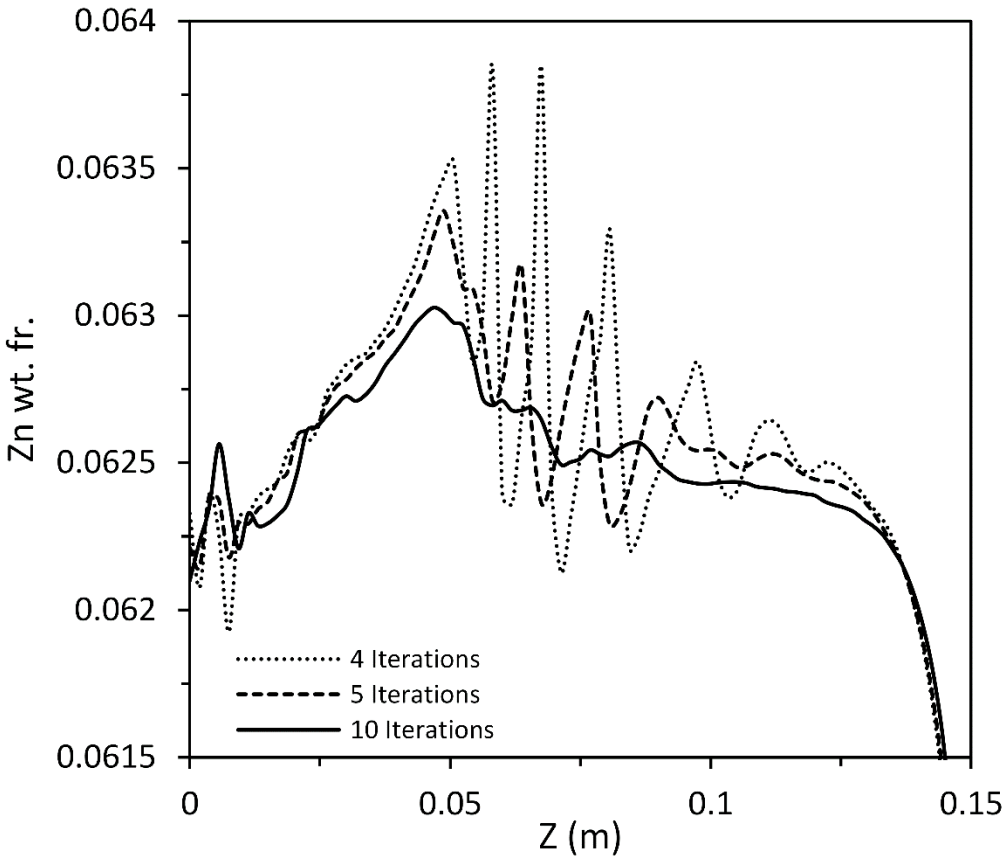

Figure 3.8: Comparison of mid-radius Zn composition profile for three iteration levels. For reference, the nominal Zn composition is 0.062.

For the results described above, each time step was limited to a certain number of iterations, but simply selecting a high number of iterations in this way will lead to unnecessarily long computation times. Instead, to obtain a converged solution without performing too many iterations, the general approach is to define convergence criteria to be applied to each of the scalar variables. One common method of determining convergence is:

$$\frac{\phi_{k+1} - \phi_k}{\Delta\phi_{ref}} < tol \tag{3.1}$$

where ϕ is a scalar variable, $k+1$ the current iteration, k the previous iteration, $\Delta\phi_{ref}$ a reference difference selected for that particular variable, and the left hand side of the equation is compared to some tolerance, tol. Appropriate reference differences and tolerance must be selected for each scalar variable, and once Equation (3.1) is satisfied for all values of interest in each control volume, the solution is considered converged.

In the present model, all of the governing equations are solved during each iteration, regardless of which ones have or have not converged. Therefore, the equation for the scalar variable with the strictest convergence criterion controls the number of iterations for all of the equations. It is therefore of interest to determine which equations are most likely to initiate channels if not properly converged. To test this question, a semi-implicit solver was implemented. Similar to Vušanović and Voller [28], the governing equations were divided into two groups. The first includes the energy equation and the species

equations, both of which interact directly with the thermodynamic model, so they should be iterated together in order to obtain an accurate solid fraction calculation. The second group contains the momentum and continuity equations, which are solved together using the SIMPLER algorithm. The energy and species equations were first iterated while using the velocity field from the previous time step. During each iteration, the thermodynamic model was used to update the solid fraction field. Once a predetermined number of iterations was completed in this manner, the momentum equations were iterated, using the most recent values for temperature and composition for the relevant buoyancy source terms. In this way, the number of iterations for each group could be controlled independently in order to compare the sensitivity of channel formation to the convergence of each group. This method is termed semi-implicit because each governing equation is implicit in itself and in the other variables solved within its group, but explicit in the variables solved in the other group.

Two tests were run, one in which four iterations were performed for the first group (energy, species, and thermodynamics) and ten iterations for the second group (momentum), and vice versa. The final Zn composition plots from these tests are shown in Figure 3.9. It is clear that additional iterations in the energy and species equations, coupled with the thermodynamic model, reduce the appearance of freckles to a much greater extent than additional iterations in the momentum equations.

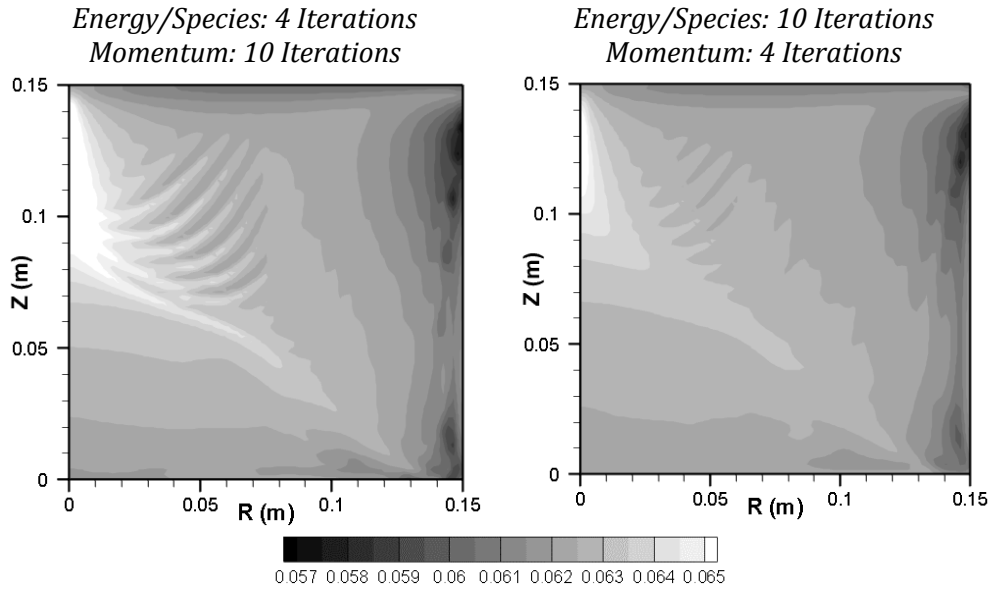

Figure 3.9: Comparison of the semi-implicit scheme for different combinations of iterations.

The final goal of this study is to determine a satisfactory convergence criterion for the fully implicit scheme that minimizes the prediction of channel defects. Rather than attempting to find the best reference difference and tolerance values for all of the equations, it is simpler to apply a strict tolerance to only one equation that will limit convergence and force all of the equations to an appropriate number of iterations. The results of Figure 3.9 show that the momentum and continuity equations approach convergence much more quickly than the energy and species equations do. This result is a consequence of the direct coupling between the temperature and composition fields to the thermodynamic model which controls the solid protrusions that initiate freckle formation. Between the energy and species equations, the energy equation is the most unstable due to the highly non-linear nature of the transient latent heat release.

Therefore, the temperature field was selected for the application of the convergence criterion.

It should be noted here that this conclusion supports the decision by Vušanović and Voller [28] to use an explicit solver for the energy and species conservation equations so that only a single iteration per time step is required. However, the drawback of their approach is that the explicit scheme is only conditionally stable and requires a relatively much smaller time step for finding a stable solution. As a point of reference, Vušanović and Voller [28] used time steps of $2x10^{-4}$ s and $6x10^{-5}$ s for simulating solidification in a square cavity measuring 40 mm on a side for 80x80 and 150x150 numerical grids, respectively. In the same study, an implicit scheme with a time step of 0.01 s (capped at 20 iterations per time step) with a 150x150 grid was also performed. When comparing these cases, it is clear that even with the reduction in the number of iterations used, the necessity of using such a small time step means that the computational expense of the explicit scheme is approximately an order of magnitude higher than that of the implicit scheme. Of course, this may not be the case for all possible conditions. In practice, there is more flexibility in the choice of time step size in the implicit scheme, but larger time steps generally require more iterations to reach convergence.

The first challenge in developing a convergence criterion according to Equation (3.1) is selecting an appropriate reference difference that is characteristic of the system, but is also as adaptable as possible, such that an appropriate tolerance may be selected that does not have to change drastically for different alloys or boundary conditions. For the latter requirement, it is important that this value is a *difference* rather than an absolute

number. For example, the initial temperature of the system might be chosen as a normalizing value. In this case, consider the same alloy solidified with two very different superheats. In the case with a high superheat, convergence will be much easier in general. However, the most important details of the process, namely, alloy solidification, happens over the same range of temperatures. Thus, to properly resolve the temperature field in the range of interest, different tolerance values would be required depending on the superheat. In the case of the energy equation, there is an obvious value to use as a characteristic difference: the alloy freezing range. Since the freezing range describes the set of values over which the most important part of any solidification process takes place, it is generally representative of the system. It is also not a function of changes in initial or boundary conditions, but will be affected by the alloy system under consideration, although this is simply determined within the model based on thermodynamic information. Here, the value is set at the beginning of the simulation based on the nominal composition and held constant and uniform throughout the process.

Now that the reference difference has been selected, an appropriate tolerance must be set. Five different tolerance values were tested and the corresponding final Zn composition results are shown in Figure 3.10. The composition field does not change when increasing the tolerance from $5x10^{-6}$ to $1x10^{-5}$, but there is some change when increasing further to $2.5x10^{-5}$. The solution changes some when increasing the tolerance to $5x10^{-5}$ and freckles become severe for $1x10^{-4}$. These comparisons are made quantitative using the normalized Weibull deviations of the final Zn composition fields and vertical composition profiles at the mid-radius as shown in Figure 3.11. These results

confirm that the final composition field changes little for tolerance values lower than $1x10^{-5}$.

The tolerance levels shown in Figure 3.10 and Figure 3.11 can be further evaluated based on the number of iterations used in each simulation. Figure 3.12 shows the average number of iterations per time step for each tolerance level, where each data point is averaged over the previous 250 time steps. For each tolerance level, the number of iterations is highest at the beginning and end of the process, with lower numbers of iterations in between. At the beginning, additional iterations are required due to the high temperature gradients near the cooling walls, and the fast convective flows that occur as a result. Near the end of the process when most or all of the bulk liquid has been consumed, solute rejection in the remaining mushy zone may have a large effect on the local composition, and through the thermodynamic model, the solid fraction. These changes are amplified by the small volume of the cells near the centerline of the casting. The transient latent heat term in the energy equation is very sensitive to these changes in the solid fraction, and an increase in iterations is require to achieve a converged solution.

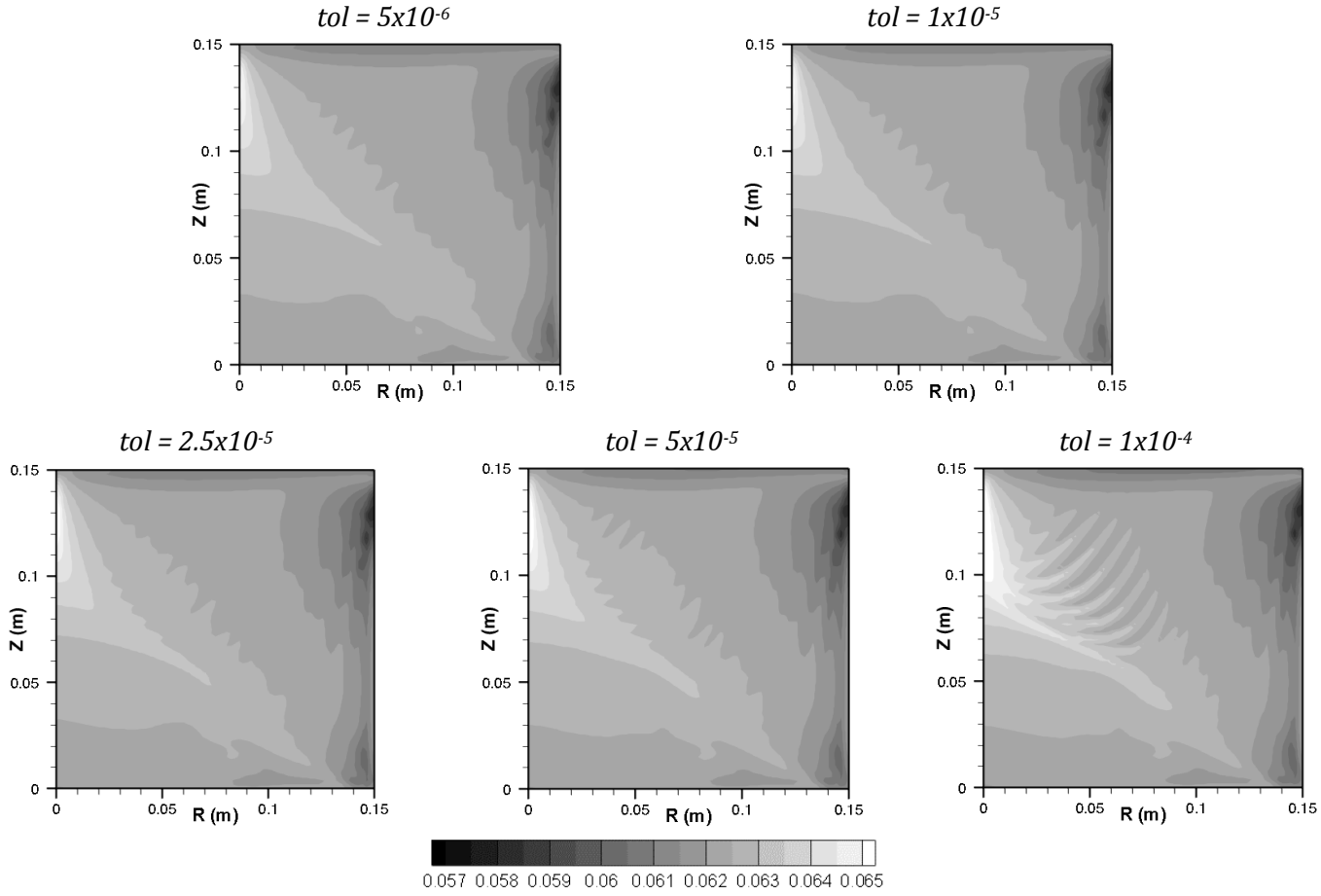

Figure 3.10: The effect of changing the tolerance for convergence of the energy equation on the appearance of freckles.

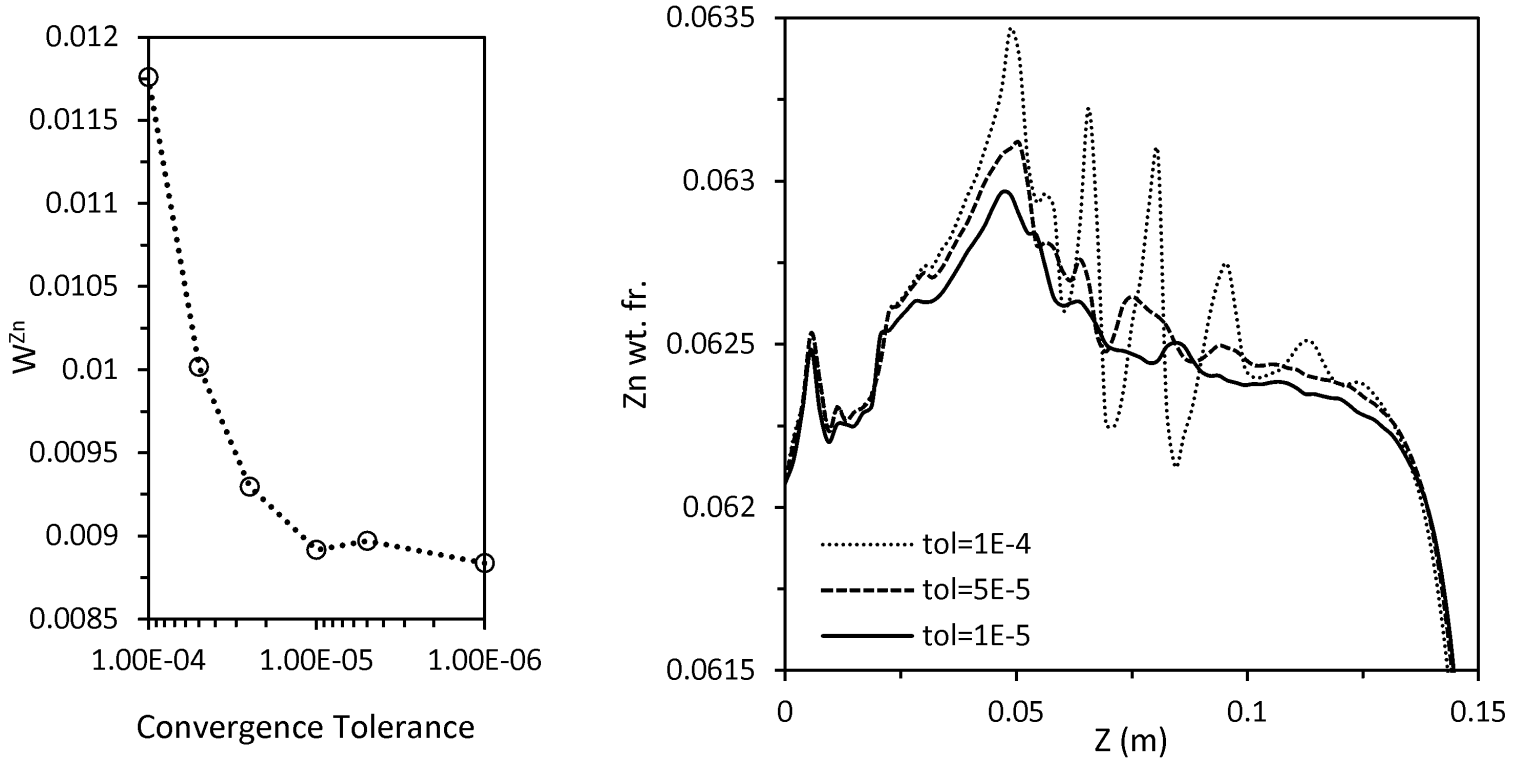

(a) *(b)*

Figure 3.11: Quantitative comparisons of difference tolerances for convergence of the energy equation (a) in terms of the normalized Weibull deviation for the final Zn composition fields and (b) shown as mid-radius composition profiles for three different tolerance levels. For reference, the nominal Zn composition is 0.062.

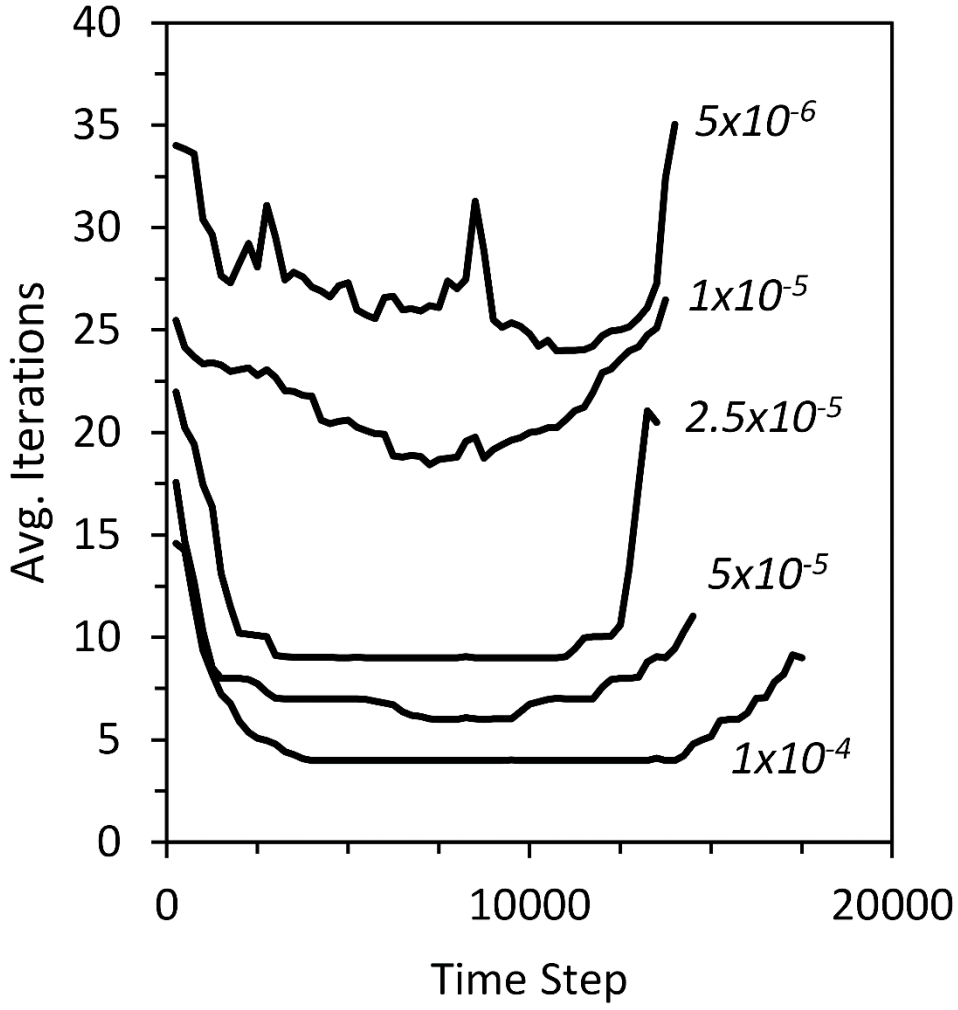

Figure 3.12: Iterations per time step for five different energy conservation tolerance. Each data point is the average of the number of iterations required for the previous 250 time steps.

As shown in Figure 3.10 and Figure 3.11, below a tolerance level of $1x10^{-5}$, there are few changes in the solution, but, as can be seen in Figure 3.12, there is an additional computational cost in the number of iterations required. It is therefore best to select a tolerance value that obtains a properly converged solution without adding unnecessary computation time. For this system, Figure 3.3 shows that convergence of the final

composition field occurs when at least 20 iterations per time step are used, a value that agrees well with the number of iterations required to meet a convergence tolerance of $1x10^{-5}$.

If simulations such as those described here are to be used to predict macroscale phenomena and to evaluate possible freckle criteria, it is important to show that converged results attain adequate grid independence. Essentially, the effect of the grid on the simulation results must be small in comparison to the effect of changes in model and process parameters. Previous work has shown that grid dependence can be judged in solidification simulations using the normalized Weibull deviation for the final composition field [79]. One example of relevant process parameters is the thermal boundary conditions. To demonstrate this, the heat transfer coefficient boundary conditions shown in Figure 2.4 were multiplied by various constants, and the resulting normalized Weibull deviations were recorded for three different grid sizes for the convergence criterion chosen above, as well as the case with only four iterations per time step (Figure 3.13). In general, the macrosegregation decreases as the solidification rate increases with the magnitude of the heat transfer coefficients. When only four iterations per time step are used rather than the convergence criterion proposed above, two major differences are noted. The first is that, for all grid sizes, the Weibull deviation is significantly higher than the converged solution. This difference is caused by the significant level of channel segregation found in the iteration limited case where the wider distribution of composition values gives a larger value of W. Additionally, the effect of the grid is significantly greater, obscuring some of the differences due to changes in the

boundary conditions. This finding is consistent with the grid dependence study in Figure 3.7. In the converged solution, the grid dependence is generally small compared to the effect of the changes in process conditions.

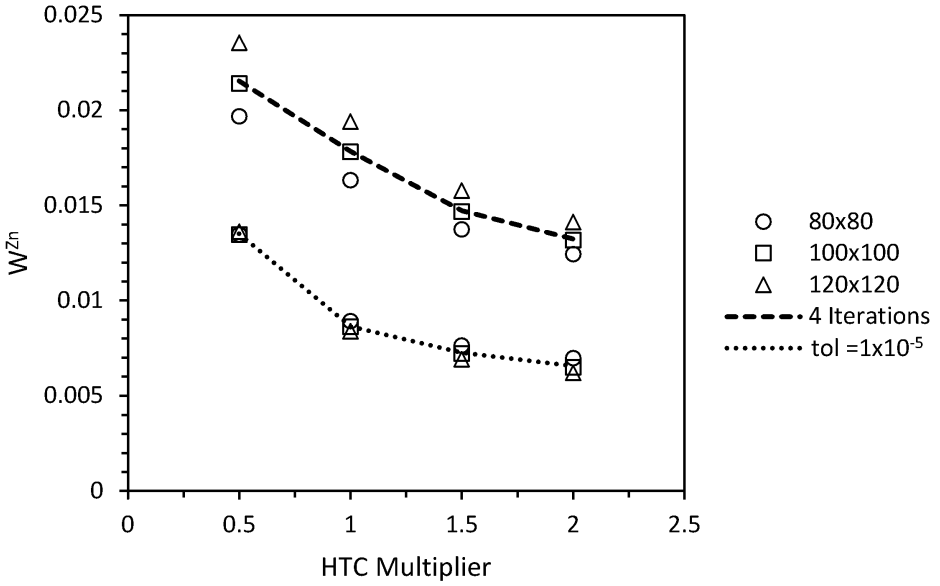

Figure 3.13: The normalized Weibull deviation as a function of boundary conditions for three different grid sizes

3.6 Conclusions

A finite volume based model for transport phenomena in alloy solidification was used to simulate the casting of aluminum alloy 7050. The model exhibited a tendency to predict the formation of freckles, a defect that is commonly observed in experimental castings. However, the model prediction was found to be highly influenced by numerical factors, including the grid spacing and the number of iterations per time step. Through understanding the mechanism of channel formation, it was found that the volume

averaged approach of the present model negates its ability to properly predict freckles. Freckle formation occurs on the length scale of the dendrite arm spacing, but using a numerical grid fine enough to resolve the protrusions that initiate freckles is numerically prohibitive for industrial scale process models. Instead, casting-scale models, such as that presented here, should be used to understand the macro-scale flow, solute transport, and solidification behavior, but must be supplemented with micro-scale models to properly predict freckling behavior. Therefore, macro-scale models should seek to predict smooth composition fields and suppress the formation of channels. To achieve this goal, a convergence criterion for the energy equation was recommended for future finite volume studies of alloy solidification. While this criterion is formulated to be as general as possible, results from similar models should be evaluated with care, and tolerance values adjusted to minimize the severity of freckle predictions. The results found here suggest that previous work that intended to predict freckles using macroscale heat transfer and fluid flow models [22–26,28] are not reliable.

CHAPTER 4. VELOCITY BASED GRAIN ATTACHMENT MODELS IN EQUIAXED SOLIDIFICATION

4.1 Introduction

As described in CHAPTER 1, most models for equiaxed solidification to this point have assumed that dendrite coherency occurs at a particular volume fraction solid or grain envelope fraction that is held constant and uniform throughout the domain. However, it is apparent that the local velocity field may advect solid grains either towards a rigid interface, tending to encourage attachment, or away from it, tending to postpone attachment. Vušanović and Krane [58] suggested a new model, within the mixture formulation for equiaxed solidification, which is intended to account for this effect of the local solid velocity. However, they only investigated the effect of this new attachment model for a single case within a model for horizontal direct chill casting. The purpose of this chapter is to more closely investigate the effect of implementing such a model and one variant (the AVM and FVM schemes, as detailed in §2.2.1) as compared to the more common constant packing fraction (CPF) approach.

4.2 Average Packing Fractions in Velocity Based Models

In the velocity-based models, the local packing fraction will vary throughout the domain based on the velocity and solid fraction fields. For valid comparisons, $g_{s,c}$ values must be chosen so that the average packing fraction ($\bar{g}_{s,p}$) is close to the value used in the corresponding CPF model. Preliminary simulations for the AVM and FVM were run over a range of critical values to establish relationships for the present system between $g_{s,c}$ and $\bar{g}_{s,p}$. An 80x80 uniform grid was used with a particle size of 20 μm and a dendrite arm spacing of 50 μm. Results are shown in Figure 4.1 for the average and standard deviation of $\bar{g}_{s,p}$, compared to the CPF approach represented as a straight line with slope of unity and a deviation of zero.

For both velocity-based models, $\overline{g}_{s,p}$ is always smaller than $g_{s,c}$, due to the imposed upper limit to the volume fraction solid in the slurry, and is lower for the FVM than the AVM because a cell can pack based on any, rather than only one, downstream control volume. This difference is also manifested in an increase in the range of packing fractions in the FVM, shown by larger standard deviations in Figure 4.1b. Overall, AVM average packing fractions are close to $g_{s,c}$, with fairly small deviations. Therefore, it is expected that the resulting macrosegregation for the AVM will much more closely resemble the CPF model than the FVM, in which cells pack over a much wider range of solid fractions.

Vreeman *et al.* [42] argue that, for the CPF model, packing fractions less than 0.3 are reasonable for aluminum alloys. In this study, a value of 0.15 for $g_{s,c}$ was used for comparison with the velocity based models. As shown in Figure 4.1a, the average packing

fraction as a function of $g_{s,c}$ can be adequately fit with a quadratic curve for both models. These function were used to calculate the values of $g_{s,c}$ that would yield $\bar{g}_{s,p}$ values equal to 0.15. The full list of cases, including the calculated values for the critical solid fractions, is given in Table 4.1.

4.3 Development of Macrosegregation in the Base Case

The general aspects of solidification of alloy 7050 and the development of macrosegregation in the domain shown in Figure 2.4 are described here for the base case in Table 4.1. The general shape of the composition field forms in a similar manner for all three packing models. Solidification in the cavity proceeds inward from the bottom and the outer radius. In accordance with the phase diagram, the solid forms depleted in Zn, Cu and Mg relative to the liquid in the same control volume. A buoyancy induced flow develops, moving down the edge of the rigid mushy zone and up the centerline. Figure 4.2 shows these results at several intermediate times for each of the three packing models. Macrosegregation results from any relative motion of the solid and liquid phases. Because these simulations do not include the effects of solidification shrinkage, there are two main contributions to this relative motion: thermosolutal buoyancy driven flow at the edge of the rigid mush, and the settling motion of solid grains. The first solid that forms at the outer radius, where cooling is the fastest, is depleted relative to the nominal composition. The associated enriched liquid is heavier than nominal because it is colder and has a higher composition and therefore, moves downward.

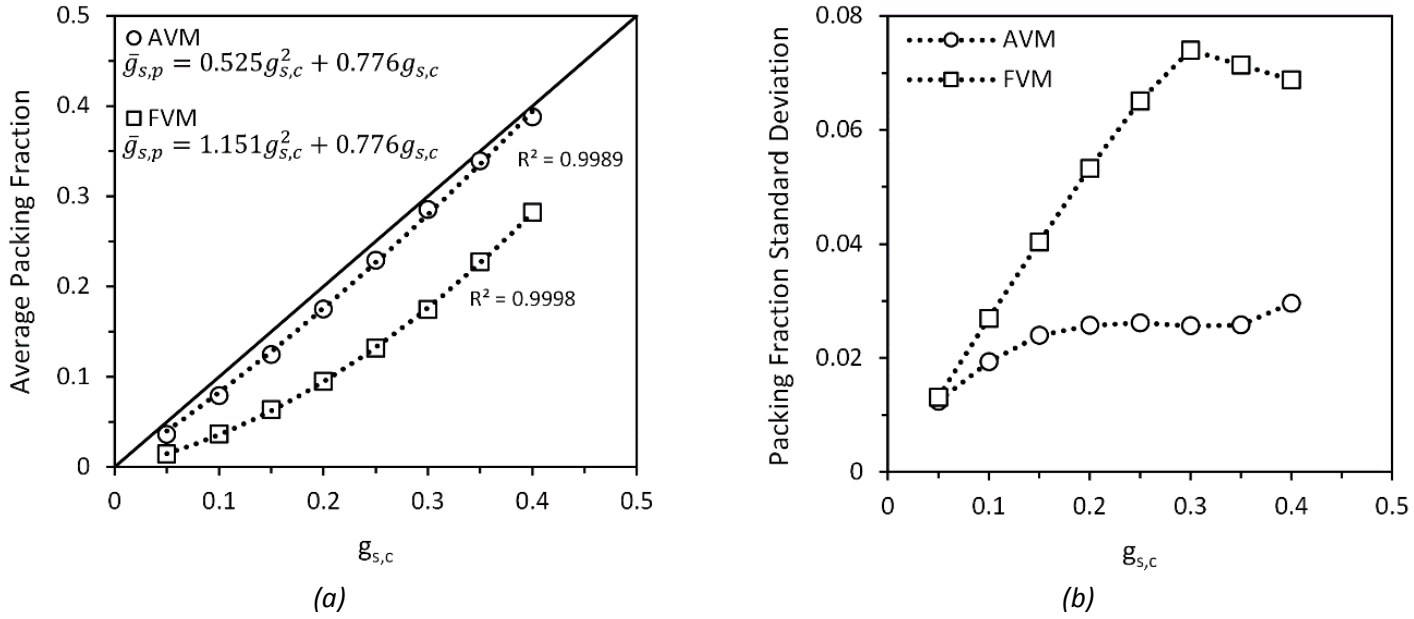

Figure 4.1: (a) Average packing fraction and (b) the standard deviation of the packing fraction as function of the critical solid fraction for the two velocity based methods.

Table 4.1: List of cases run for the parametric study.

	$g_{s,c}$	$g_{s,c}$ (AVM)	$g_{s,c}$ (FVM)	Grid	Particle Size (μm)	DAS (μm)
Base Case	0.15	0.175	0.271	80x80	20	50
Varying Grid	0.15	0.175	0.271	40x40	20	50
	0.15	0.175	0.271	60x60	20	50
	0.15	0.175	0.271	100x100	20	50
	0.15	0.175	0.271	120x120	20	50
	0.15	0.175	0.271	140x140	20	50
	0.15	0.175	0.271	160x160	20	50
	0.15	0.175	0.271	80x80	5	50
Varying Particle Size	0.15	0.175	0.271	80x80	10	50
	0.15	0.175	0.271	80x80	50	50
	0.15	0.175	0.271	80x80	75	50
	0.15	0.175	0.271	80x80	100	50
Varying DAS	0.15	0.175	0.271	80x80	20	20
	0.15	0.175	0.271	80x80	20	35
	0.15	0.175	0.271	80x80	20	65
	0.15	0.175	0.271	80x80	20	80

This effect is only significant at the edge of the rigid mush where the comparatively high permeability allows some enriched liquid to flow into the bulk, whereas the lower permeability deeper in the mushy zone prevents any significant fluid flow. Depleted, unattached solid near the edge of the rigid interface is advected downward and then towards the centerline of the cavity. The particles then resist the slow up-flow of the liquid at the centerline according to Stokes' law (Equation (2.23)), tending to settle instead. The falling solid causes a depleted region at the centerline and displaces the associated liquid, which tends to enrich the region nearer the top of the cavity. These trends can be seen in the final composition fields shown at the bottom of Figure 4.2.

The next notable difference among the three cases shown in Figure 4.2 is the volume and level of negative segregation found at the outer radius. The CPF model and AVM appear to have similar volumes of depleted solid here, although a direct comparison is difficult because of the instabilities in the CPF case. However, the FVM clearly has a much larger volume of negative segregation than the other two models, an observation that is confirmed by plotting the fitted three-parameter Weibull distributions for the final composition fields in Figure 4.3. The y-axis values of the PDFs in Figure 4.3 are related to the volume of material found at a given composition. Note that the fitted PDFs are valid for all real numbers, but here, are terminated at the minimum and maximum final compositions predicted by the model. The CPF model has the longest tail to the left, indicating a small volume of very depleted material, which, as can be seen in Figure 4.2, is located within the channel segregates at the outer radius. Because the two velocity based schemes tend to suppress these channels in this particular case, the magnitude of the negative segregation at the outer radius is lower, resulting in shorter tails to the left. The AVM has a higher peak near the nominal composition ($C_0^{Zn} = 0.062$). This change is a result of the reduction in channel segregation, and a subsequent narrowing of the overall distribution. The FVM distribution has a lower peak than the other two, with a higher tail to the left associated with the large depleted volume near the outer radius, and a more extreme tail to the right than the other models caused by a more enriched region at the top of the cavity. The width of the distributions is quantified by the normalized Weibull deviation which was 0.0100, 0.0067, and 0.0122 for the CPF, AVM,

and FVM composition fields, respectively. The relative values of the normalized Weibull deviations for the three models reflect the differences in the standard deviations of the local packing fractions (Figure 4.1b) as well as differences in the propensity for formation of channel segregates. These relationships between the details of the packing model and the compositions distributions suggest that the manner in which packing occurs has a strong effect on the formation of macrosegregation.

The similarity between the local packing fraction, shown for the velocity-based models in Figure 4.4, to the final composition fields is striking, and is related to the initial permeability of the rigid solid when it first packs. In the velocity-based models, high temperature gradients, and therefore high solid fraction gradients, favor low packing fractions near the cooling walls because there is a greater probability that a control volume will neighbor a cell with a solid fraction greater than $g_{s,c}$. This effect is more extreme in the FVM than AVM because multiple downstream cells may trigger packing, generally increasing the likelihood of packing at lower solid fractions relative to the AVM. Solid that packs with a very low packing fraction has a correspondingly high permeability compared to regions with high packing fractions. This higher permeability allows enriched liquid to more easily flow into the bulk and be replaced by fresh liquid nearer the nominal composition. In cells with high packing fractions, the reduced permeability restricts advection of enriched liquid. The result is that control volumes with low packing fractions tend to be depleted in composition, and control volumes with higher packing fractions

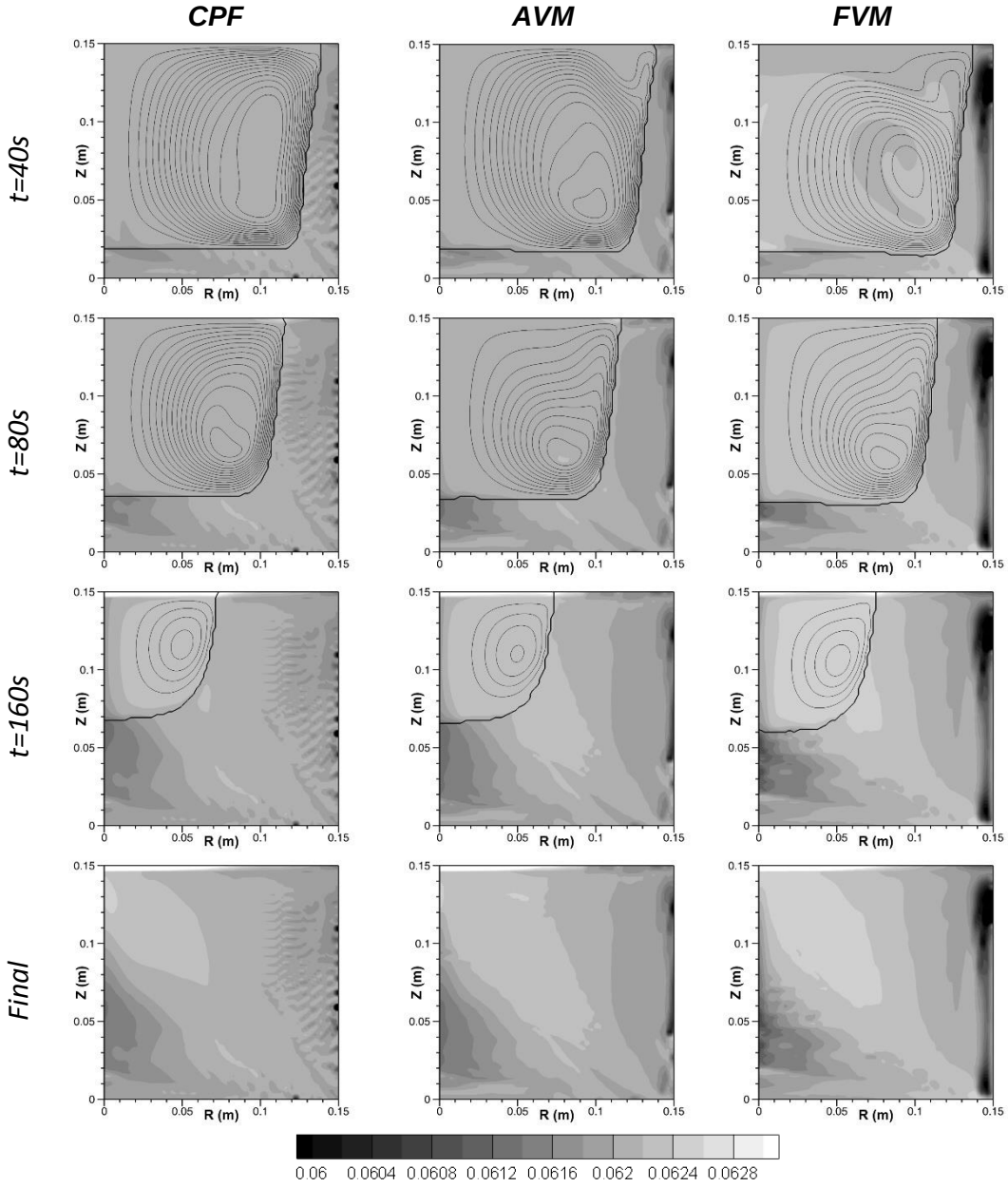

Figure 4.2: The Zn composition field, flow field, and packed interface at three times during solidification for the three different discrete packing models. Thin lines show streamlines in the clockwise direction and the bold line is the packed interface. The packing fraction for the CPF model was 0.15 and the average packing fraction was 0.147 for the AVM and 0.148 for the FVM.

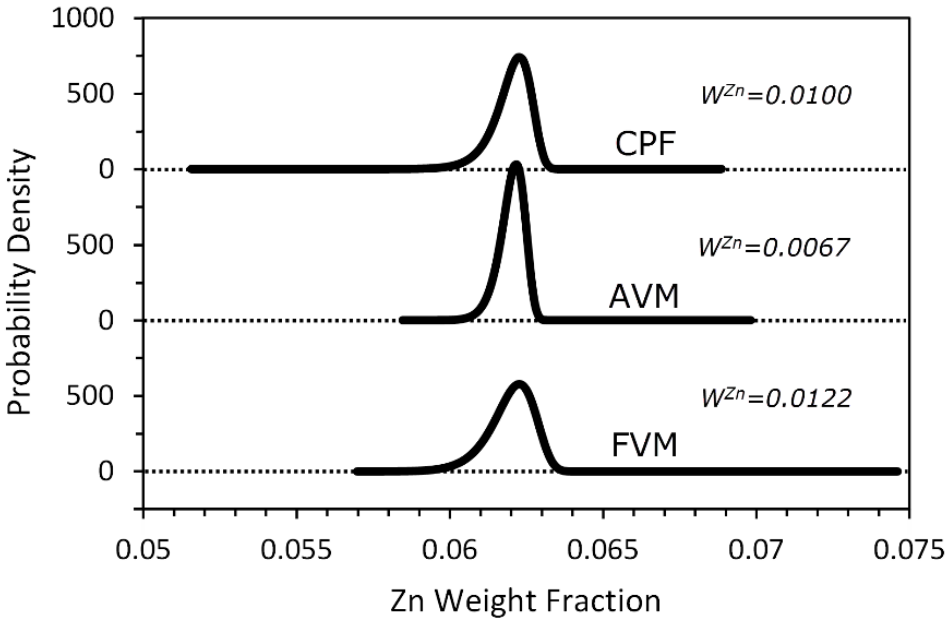

Figure 4.3: Fitted three-parameter Weibull distributions for the base case of each packing model.

tend to be enriched. This relationship explains why the FVM model, with a wider range of packing fractions, also exhibits a wider composition distribution (Figure 4.3).

The negative region at the outer radius is also shifted upwards slightly for both velocity-based cases compared to the CPF model. This upward shift is the result of the flow field which moves radially outward near the top of the cavity. In the CPF model, any solid advected with the outward flow is swept downward along the outer radius by the natural convection loop, and the solid advection does not affect packing unless it causes a buildup of solid in a particular cell that exceeds $g_{s,c}$. However, in the velocity-based models, this outward flow increases the likelihood of packing at the top of the domain against the outside of the cavity or against any solid that has already packed here. This

packing is reflected in the lower packing fraction of this region, shown in Figure 4.4. Since the solid that packs here is initially at a lower solid fraction, it has a higher permeability and allows the enriched liquid to flow out of the rigid mush to be replaced by fresh liquid that is lower in composition, decreasing the overall composition of the cells in this region.

4.4 Grid Dependence

Contour plots showing the final composition profile for several different grid sizes are given in Figure 4.5. The first feature to note is that due to the settling of solid particles that have a lower composition than the liquid, the centerline of the ingot tends to be depleted, and the vertically displaced enriched liquid is the last material to freeze at the top of the casting, forming a region of positive segregation. The level of enrichment in this upper layer is inversely related to the size of the control volumes over which the composition is averaged, so that the composition of this region is higher for finer grids. This strong grid dependence of the maximum composition was previously reported by Voller and Vušanović [43] for simulations of columnar solidification. The results in Figure 4.5 also demonstrate the grid dependence of the appearance and size of channel segregates, or compositions instabilities, which can be primarily seen propagating inward from the outer radius, although some instabilities also develop nearer the centerline. In the CPF model, these instabilities are present for all cases, and their spacing is highly grid dependent. In the AVM model, instabilities very similar to those seen in the CPF model develop for coarse grids, but are suppressed with intermediate grids. Instabilities reappear for fine grids, but their propagation is limited compared to the CPF model.

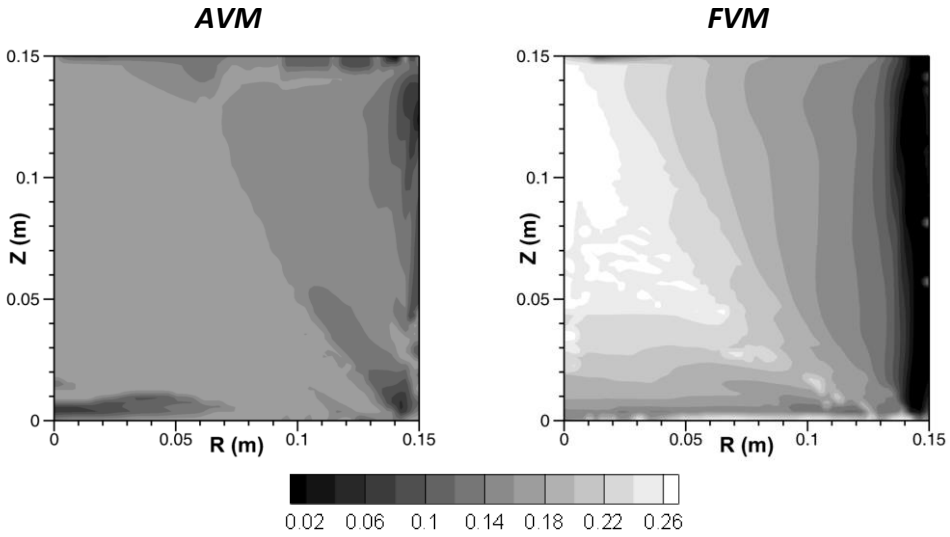

Figure 4.4: Distribution of local packing fractions ($g_{s,p}$) for the base case with the AVM and FVM packing protocols.

The FVM also appears to show some reduction in instabilities (especially near the outer radius) when going from a coarse grid to an intermediate grid, but develops severe instabilities at fine grid sizes. While these instabilities cause grid dependent cell-to-cell variations in the composition field, the overall macrosegregation level, characterized by the normalized Weibull deviation, is less sensitive to grid size than it might first appear. As shown in Figure 4.6, after an initial change in these macrosegregation metrics for coarse grids, some level of convergence does begin to appear for finer grid sizes. The reason for the grid convergence in these metrics is that even though the range of compositions in the final casting is growing wider, the extremely enriched and depleted regions are occurring over smaller volumes as the grid is refined. The compositional extremes therefore affect the tails of the composition distribution less and less as the grid size decreases, leaving the bulk of the macrosegregation pattern mostly unchanged.

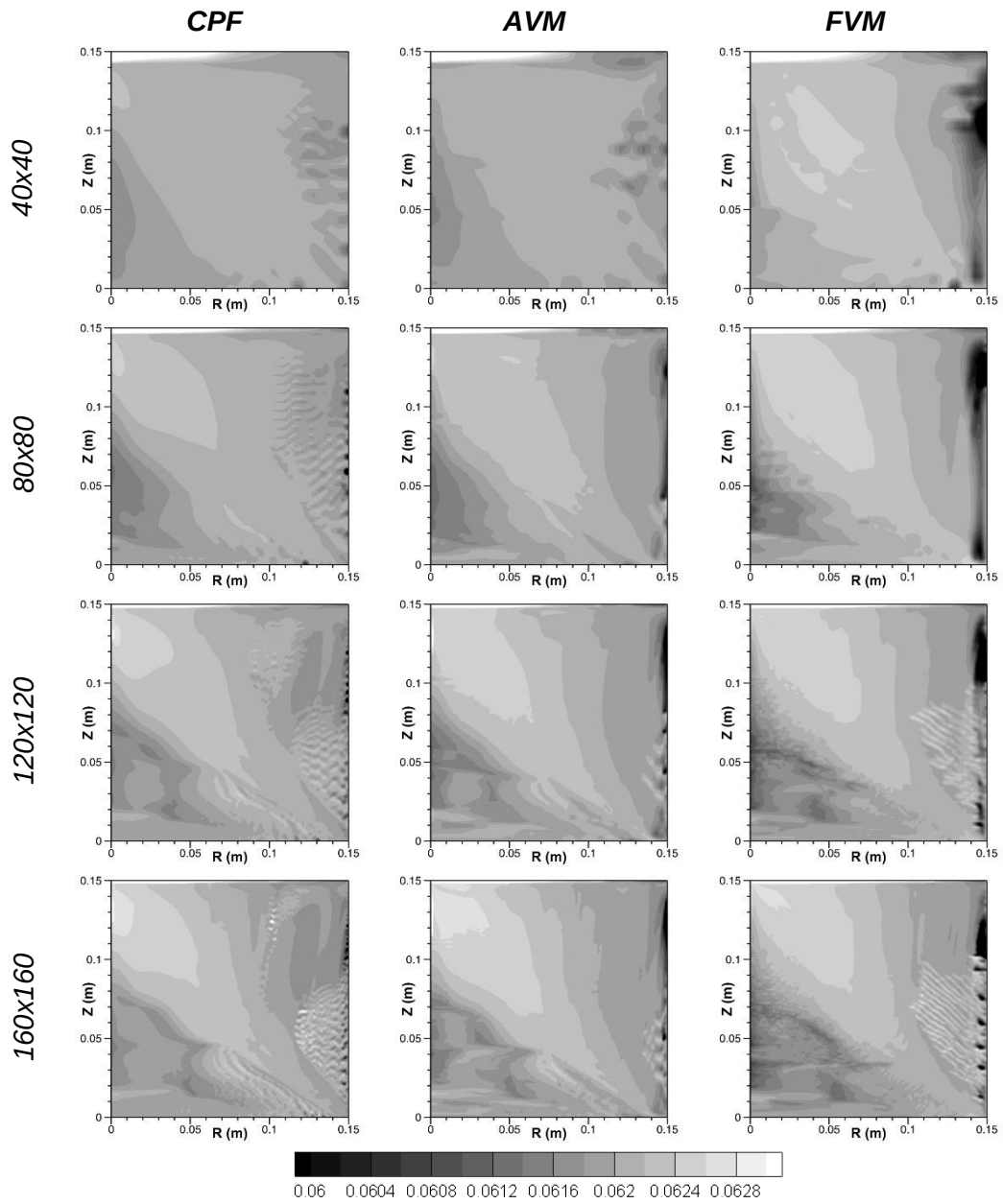

Figure 4.5: Grid dependence of final Zn composition fields (in wt. fr.) for each packing model, showing results of simulations with 40x40, 80x80, 120x120 and 160x160 control volumes.

Unfortunately, the spacing and severity of the channel segregates do not approach grid independence. The details of the formation of these defects is the subject of CHAPTER 5, but some general conclusions may be drawn from the data presented here. First, the primary cause of these compositional differences is likely due to advection over diffusion, simply by noting the order of magnitude of the mass diffusivity. Therefore, the coupling between the momentum conservation equations and solute advection must be carefully considered to determine the source of their grid dependence. As seen in Figure 4.5, the packing scheme undoubtedly has an effect on the formation these channels. This effect is not surprising in light of the dependence of the flow field and consequent solute transport on the permeability in the mushy zone, the application of which is controlled by the packing model. The larger question of course, is whether the prediction of these channels is realistic. If they are a numerical artifact, then a numerical model that suppresses these channels is desired. If they are found in experimental castings, then developing a numerical model that accurately predicts their occurrence will be of the utmost importance.

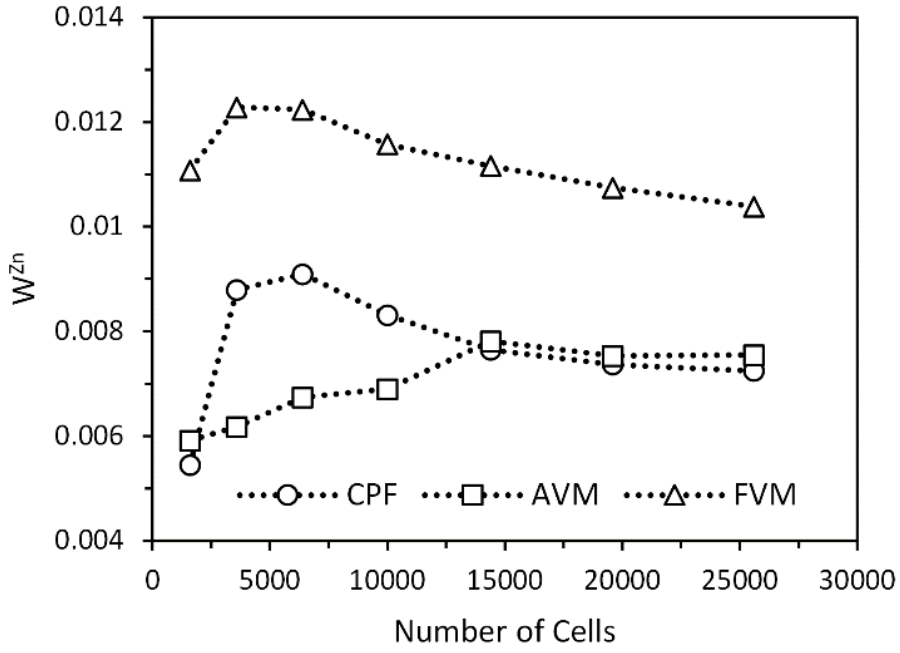

Figure 4.6: Quantification of macrosegregation in each of the three packing models using the normalized Weibull deviation for Zn.

4.5 Particle Size Dependence

The size of the free-floating grains in the present study is set at a single, constant value, an approach which is a simplification of the reality of equiaxed grain growth with its transient distribution of sizes throughout the domain. However, this simplification allows for a look at the effect of average grain size on macrosegregation development. According to Stokes' law the difference in solid and liquid velocities in the direction of gravity goes as the square of the particle diameter. At smaller diameters, particles mostly move with the liquid, and this absence of relative motion between the solid and liquid prevents macrosegregation development in the slurry region. At larger diameters, however, the particles settle very quickly, severely depleting the bottom of the slurry

relative to the transient location of the solidification front. The corresponding enriched liquid is displaced towards the top of the casting. The larger the particles, the more dramatic this compositional stratification due to settling becomes, and as a consequence, the composition distribution broadens, as shown for extreme particle sizes for the three packing models in Figure 4.7a. This broadening is also reflected in an increase in the normalized Weibull deviation and the macrosegregation number, as shown in Figure 4.7b. A similar result was observed for composition distributions in DC casting by Vreeman and Incropera [8]. Generally, the three packing models are all affected similarly by changes in particle size.

4.6 Dendrite Arm Spacing Dependence

One of the main driving mechanisms for macrosegregation is the relative motion of solid and liquid at the edge of the rigid mushy zone. The primary factor that influences the tendency for fluid motion here is the permeability of the dendritic array, which is modeled here using the Blake-Kozeny relationship and increases with the square of the dendrite arm spacing. A lower permeability provides less resistance to the downward thermosolutal buoyancy of the cooler, enriched liquid that drives the natural convection flow cell. As the dendrite arm spacing and therefore the permeability increases, the flow rate of enriched liquid away from the rigid, depleted solid also increases. This increase in the relative velocity between the solid and liquid of differing composition increases the level of segregation in the domain. The difference in segregation is visualized in Figure 4.8 using the normalized Weibull deviation for the final predicted Zn composition fields for

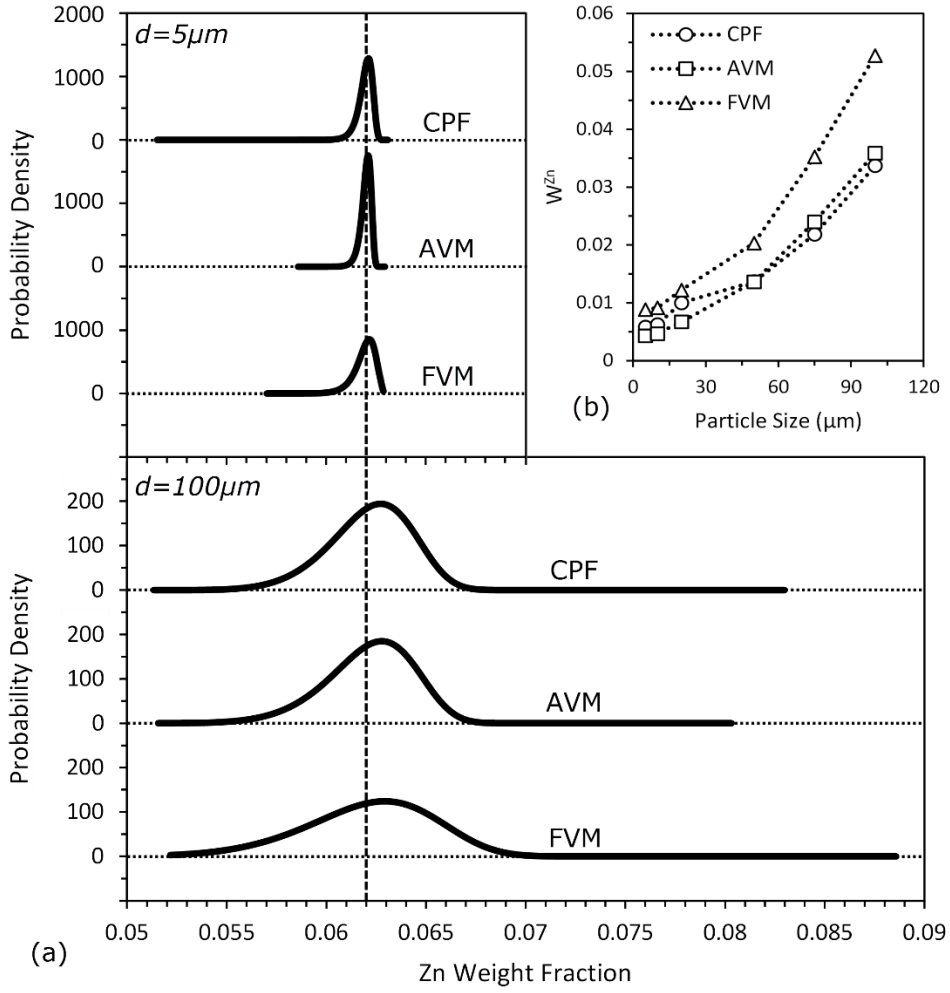

Figure 4.7: (a) Comparison of fitted three-parameter Weibull distributions for the final Zn compositions fields of the three packing models at extreme particle sizes and (b) a plot of the normalized Weibull deviation over the full range of particle sizes. Note the difference in scale of the y-axis between the top and bottom plots in (a).

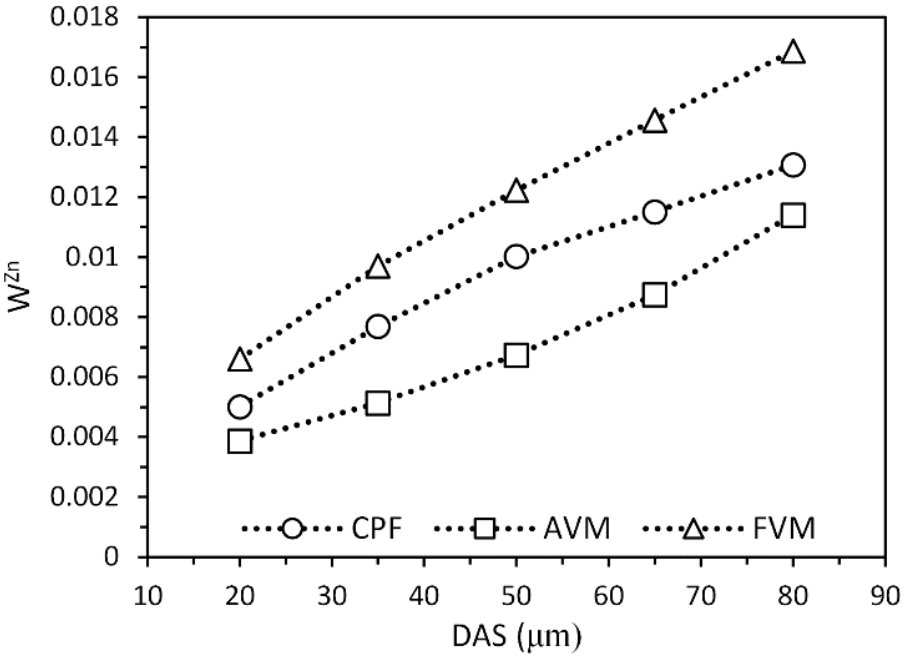

Figure 4.8: The normalized Weibull deviation for the final Zn composition field predicted by each packing scheme as a function of dendrite arm spacing.

each packing scheme. As expected, the width of the composition distributions increases with dendrite arm spacing.

4.7 Conclusions

The effect of two velocity-based packing schemes, namely the average velocity method (AVM) and the face velocity method (FVM), on the development of macrosegregation have been described and compared to the standard constant packing fraction model. The different models were implemented in a simulation of cylindrical static casting of a commercial aluminum alloy (AA7050). A parametric study was performed to investigate the effect of model parameters including the critical solid

fraction, the grid size, the free-floating particle size, and the dendrite arm spacing. In many cases, the velocity-based models, and particularly the FVM, have a dramatic effect on the resulting composition fields. In some cases these effects can be related to the range over which solid packs throughout the domain. It is extremely difficult, however, to comment on which of the models best represents reality because presently no detailed experimental data is available in the literature for validation. Experimental data suitable for model validation must measure packing fraction and the composition field in the context of the coupled effects of cooling conditions, dendrite morphology, and grain refiner additions.

A further complicating factor is the susceptibility of the present solidification model to the appearance of channel segregates. The extreme grid dependence of these defects suggests a possible numerical origin, even though similar defects (e.g. A-segregates, freckles) have often been observed experimentally. Curiously, the velocity-based methods seem less prone to develop compositional instabilities than the constant packing fraction approach, particularly for moderate grid sizes. The purpose of CHAPTER 5 is to determine whether or not any of these models are an accurate representation of the physical system and whether the prediction of channel segregates is a physical phenomenon or a numerical artifact.

CHAPTER 5. CHANNEL SEGREGATION IN EQUIAXED SOLIDIFICATION

5.1 Introduction

In CHAPTER 4, channel segregates were observed in the predicted composition fields of equiaxed solidification simulations and were found to exhibit an extreme grid dependence. These defects are similar in appearance to freckles that form in columnar castings, but no experimental observations support their prediction in equiaxed cases. The purpose of this chapter is to more closely investigate the initiation and propagation of these channel segregates for the CPF and AVM grain attachment models in order to determine the physical relevance of these predictions.

5.2 Initial Simulations: Dependence on Grid Size and Packing Rules

To begin, the motion of the solidification front, flow patterns, and the development of macrosegregation are shown in Figure 5.1 for the CPF model. Solidification proceeds inward from the outer radius and upwards from the bottom. Because Zn preferentially partitions to the liquid, the first solid to form has the lowest composition in the domain. Thermosolutal buoyancy drives natural convection flow in a clockwise direction. The free-floating solid particles, being denser than the liquid, resist the upward flow at the centerline according to Stokes' law. These solid particles are depleted in Zn relative to the

liquid and therefore, when they settle, they deplete the bottom of the cavity relative to the transient location of the solidification front. This motion of the solid particles displaces comparatively enriched liquid, eventually leaving a region high in Zn at the top of the casting. In addition to these general trends in macrosegregation, the presence of channel segregates is clearly evident beginning at the outer radius of the casting and propagating inwards.

Figure 5.2 shows final Zn composition profiles for the CPF model at various grid sizes. The overall shape of the macrosegregation is not significantly affected by the grid size. In all cases, the outer radius and bottom of the casting near the centerline are depleted, and the top of the ingot near the centerline is enriched. However, the morphology of the channel segregates has an extreme grid dependence. Channels form for all grid sizes, but the distance between the channels is on the order of the grid spacing in all cases. Additionally, the level of segregation within the channels increases for finer grids.

Figure 5.3 shows the grid refinement results for the AVM packing rules. Again, the general shape of the macrosegregation profile is only weakly dependent and is similar to the CPF results, but the effect on the channel segregates is surprising. For coarse grids, segregates appear on the scale of the grid spacing as expected, but they are more isolated and sporadic than those that appear in the CPF model. For the moderate grid size, the segregates are almost completely suppressed, but a few reappear at the outer radius in the fine grid.

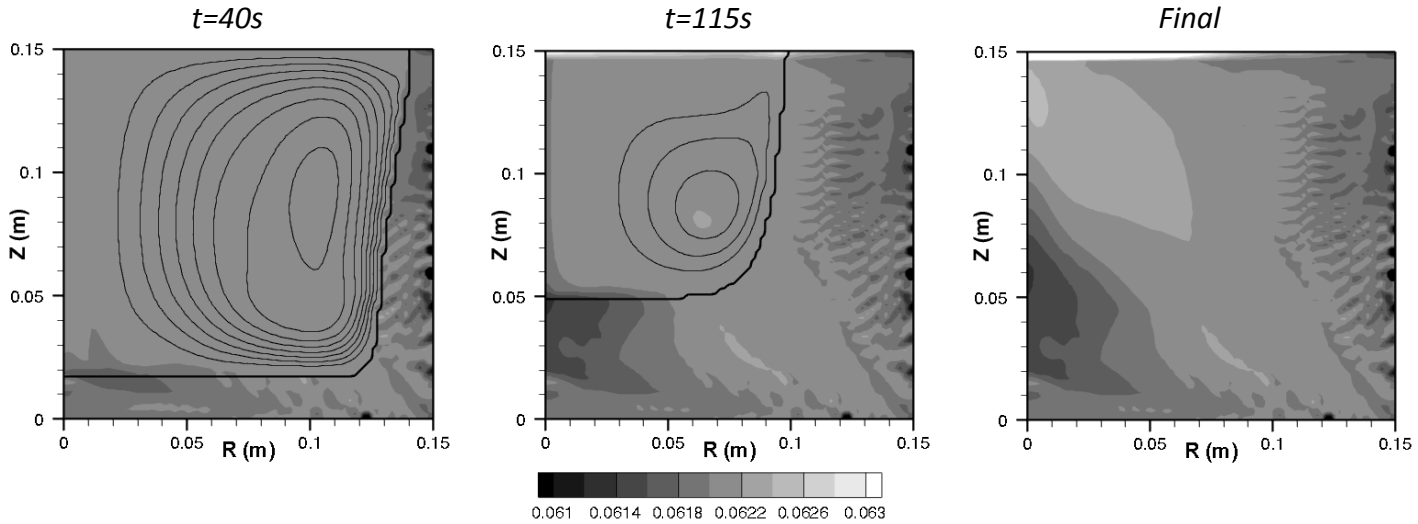

Figure 5.1: Zn composition fields and streamlines showing the advancing solidification front and macrosegregation development at intermediates times throughout the process. The bold line shows the interface between the slurry and rigid packed region, and the light lines are clockwise streamlines from 0.02 to 0.22 kg/s in $\Delta(\rho\psi) = 0.02\ \mathrm{kg/s}$ increments. The numerical grid is 80x80 cells.

.

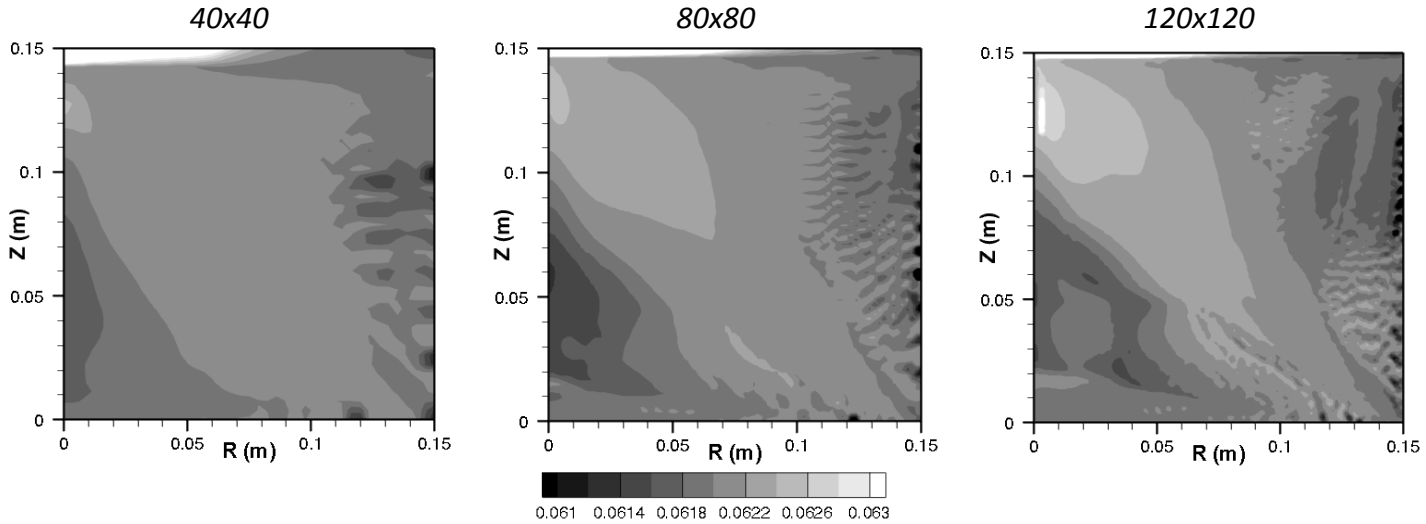

Figure 5.2: Final Zn composition fields showing the grid dependence of channel segregates predicted with the CPF model.

This dependence on grid size and packing model, as was previously reported in [81] , raises the concern that these types of defects are numerical artifacts without physical relevance. These results suggest that there is a combined dependence on the numerical length scale and the transition from the slurry region to the rigid dendritic network, but in order to confirm these suspicions, the mechanism for channel formation must be more closely investigated. If these defects are numerical artifacts without physical relevance, then it may be of interest to determine the conditions under which a smooth composition field, such as that shown for the 80x80 grid in Figure 5.3, occurs, and whether and how the simulation may be appropriately tuned to avoid the development of segregates.

5.3 The Mechanism of Channel Formation

In an attempt to identify the mechanism by which channel segregates initiate and propagate, the CPF model was carefully observed. Because these compositional instabilities first appear at the outer radius where solidification begins, this region was monitored near the start of the process. A series of contour plots showing the initiation of channel segregates is shown in Figure 5.4 for the CPF case with an 80x80 grid. Note that the view of these plots is an extreme close-up of the bottom right corner of the domain, allowing for observation on a cell-by-cell basis. The contour indicates the Zn compositional field, the vectors the solid (not mixture) velocity, and the bold lines demarcate the slurry and packed regions.

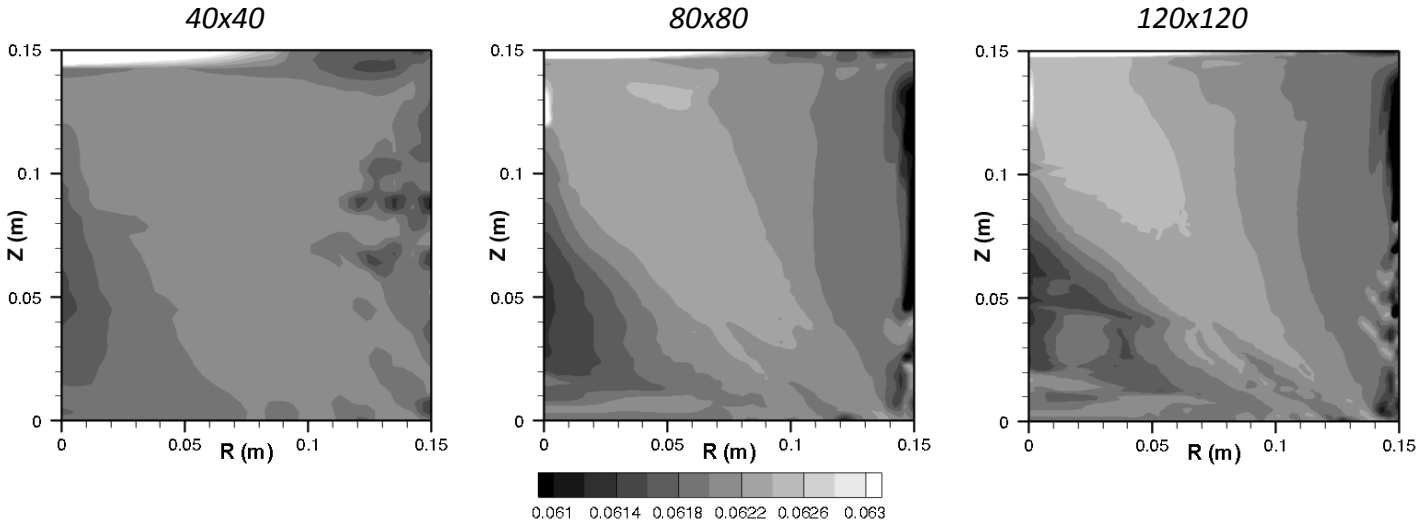

Figure 5.3: Final Zn composition fields showing the grid dependence of channel segregates in the AVM packing model.

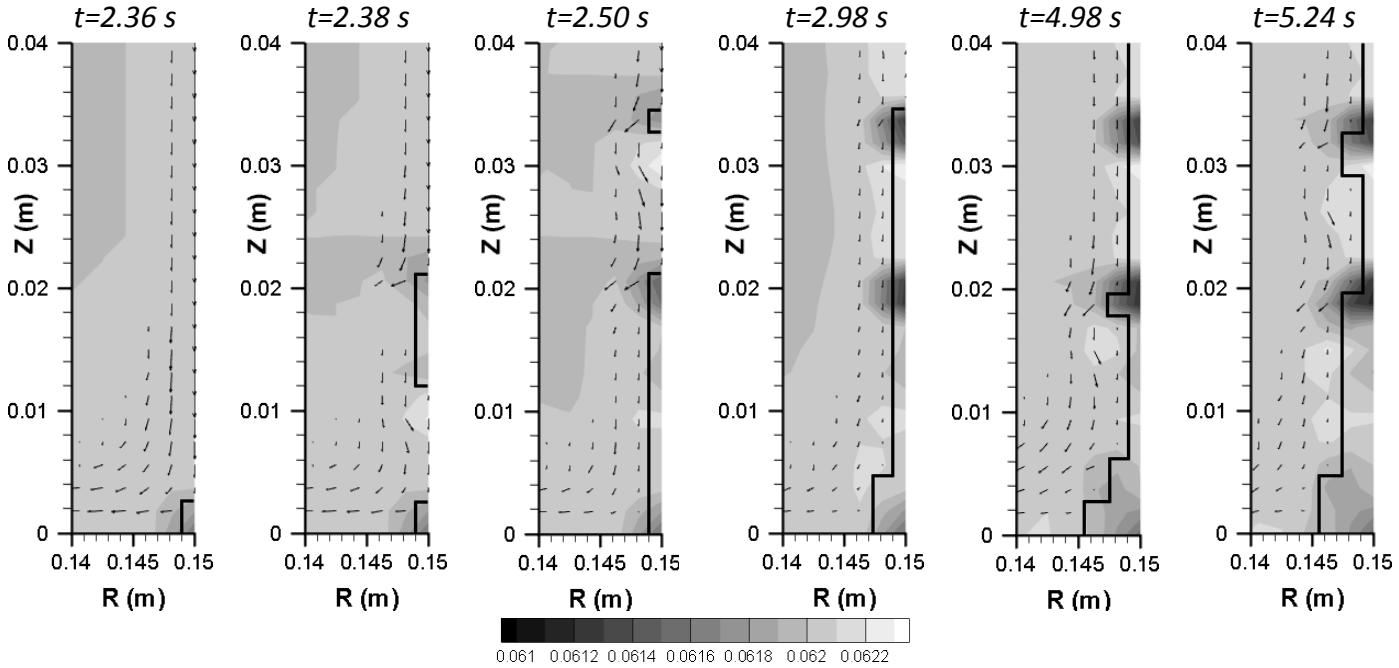

Figure 5.4: Initial development of channel segregates at the outer radius at the beginning of the process for the CPF model. The contour is the Zn wt. fr., the vectors show the solid velocity, and the black line indicates the interface between the slurry and rigid solid regions.

At the very beginning of the process, thermally induced natural convection drives fluid downward at the outer radius while at the same time, the solid fraction is slowly increasing. Equiaxed particles move with a downward velocity slightly larger than the liquid (with the difference in velocities dependent on the particle size according to Stokes' law). The compositional field is relatively uniform until the fraction solid in one or more of the cells reaches the packing fraction. Some cells will pack such that they jut out into the slurry region, such as those shown at $t = 2.38\ s$ in Figure 5.4, and disrupt the local flow field. These rigid protrusions affect the flow because solid is not able to flow into or out of these cells according to the definition of the rigid mushy zone, and because the limited permeability of the rigid solid acts as a barrier to flow of the bulk fluid.

This sudden change in the flow conditions around these rigid protrusions has a dramatic effect on the local composition. The depleted solid within the cells is forced to remain stationary, but the slight permeability of the cell allows some enriched liquid to continue flowing downstream, to be replaced by upstream fluid of a composition nearer the nominal. Additionally, because the cell is packed, solid particles from upstream are blocked and tend to collect in the upstream cell or are forced to flow around the packed cells as seen by the solid velocity vectors in Figure 5.4, especially at $t = 2.38$ s, 2.50 s and 4.98 s. The result is that the cell downstream from the packed region becomes enriched from liquid flowing out of the packed cell while the upstream cell becomes depleted, creating a banded composition field that acts as an initiation site for a channel. Once a vertical column of control volumes is packed, the mechanism repeats when rigid

perturbations jut out from the packed interface into the next column of control volumes such as those shown at times $t = 4.98$ s and $t = 5.24$ s.

Once initiated, channel propagation occurs through coupling of the banded composition field with the thermodynamic model, explaining why, in the CPF model, the next column of control volumes tends to build on existing channels rather than forming new compositional streaks at random positions. An example of propagation is shown in detail for the CPF model in Figure 5.5. When neighboring control volume (in the radial direction) are enriched or depleted, as shown at $t = 24.86$ s, their liquidus and solidus temperatures are changed as well. The liquidus temperature in enriched cells is depressed while it is increased in depleted cells. For a given temperature, these changes correspond to an increase in solid fraction in depleted cells and decrease in enriched cells. In the CPF model, packing is based solely on the solid fraction of the cell of interest, so that the depleted cells with a higher solid fraction will become packed sooner, becoming rigid perturbations and advancing the channel through the same mechanism discussed above (Figure 5.5).

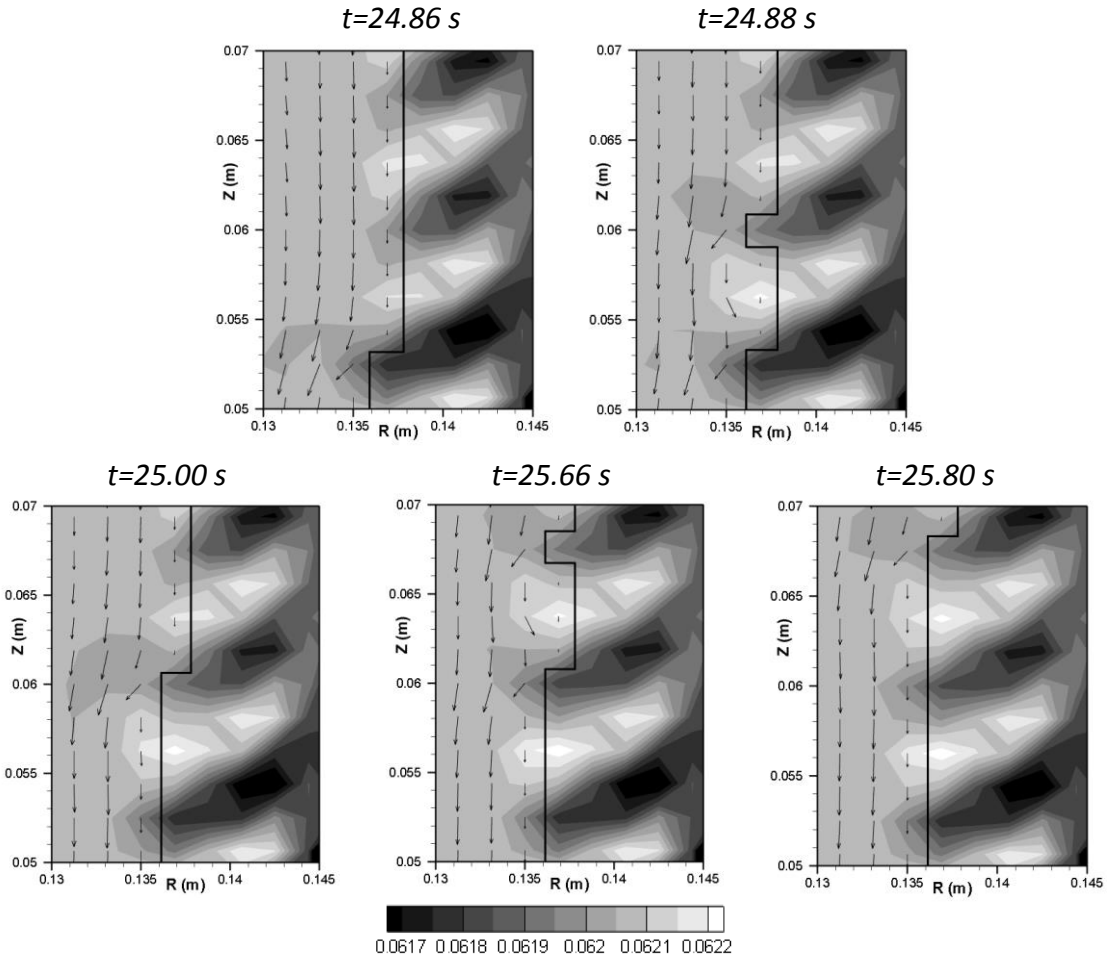

Figure 5.5: Propagation of channel segregates in the CPF model. The color contour is Zn wt. fr., the vectors show the solid velocity, and the dark line is the border between the rigid mush and the slurry region.

Now that the mechanism for the formation and propagation of these channels is understood for the CPF model, it is interesting to investigate further the case of the AVM packing model in which channels do not form. The region near the outer wall is shown in Figure 5.6 at the beginning of the process for the AVM, again showing the Zn composition field, solid velocity vectors, and the border between the slurry and packed regions of the domain. Initially, a rigid protrusion forms on the outer wall, seen at $t = 2.48\ s$. However,

unlike the CPF model, the packing of subsequent cells is not based on the condition of the cell itself, but on the condition of the downstream cell. Therefore, it is common for cells to pack consecutively upwards due to the primarily downward solid velocity rather than forming a series of rigid protrusions. Channels do not form in this case because each cell packs in a similar manner relative to its neighbors, affecting the surrounding composition field in a similar way, resulting in a mostly smooth segregation pattern.

Unfortunately, the balance between the velocity field, composition field, and packing model is precarious. A slight change in any of a variety of variables can result in the formation of rigid protrusions and the reappearance of channels. Changing the grid size changes the length of the offset in the packing model, and when coupled with the effect of the composition on the local solid fraction field along the direction of the solid motion, protrusions may begin to form. This particular case is seen for the both coarser and finer grids in Figure 5.3. Changes in the solid fraction and flow fields can also result in channel formation. For example, as shown in Figure 5.7, increasing the magnitude of the heat transfer coefficient boundary conditions speeds the flow and increases the solidification rate. Here, the formation of a channel, as opposed to a smooth composition field, can clearly be seen.

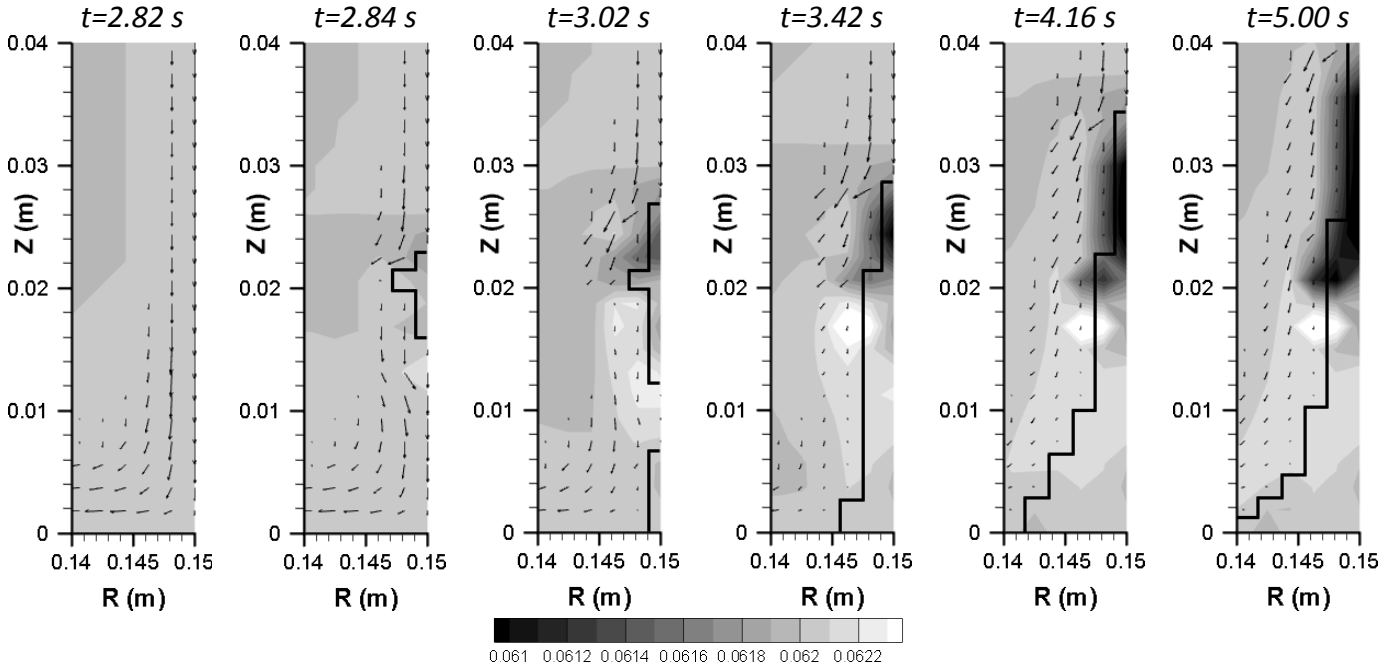

Figure 5.6: Zn composition fields in the AVM showing the initial development of the packed region at cooling wall at beginning of the process.

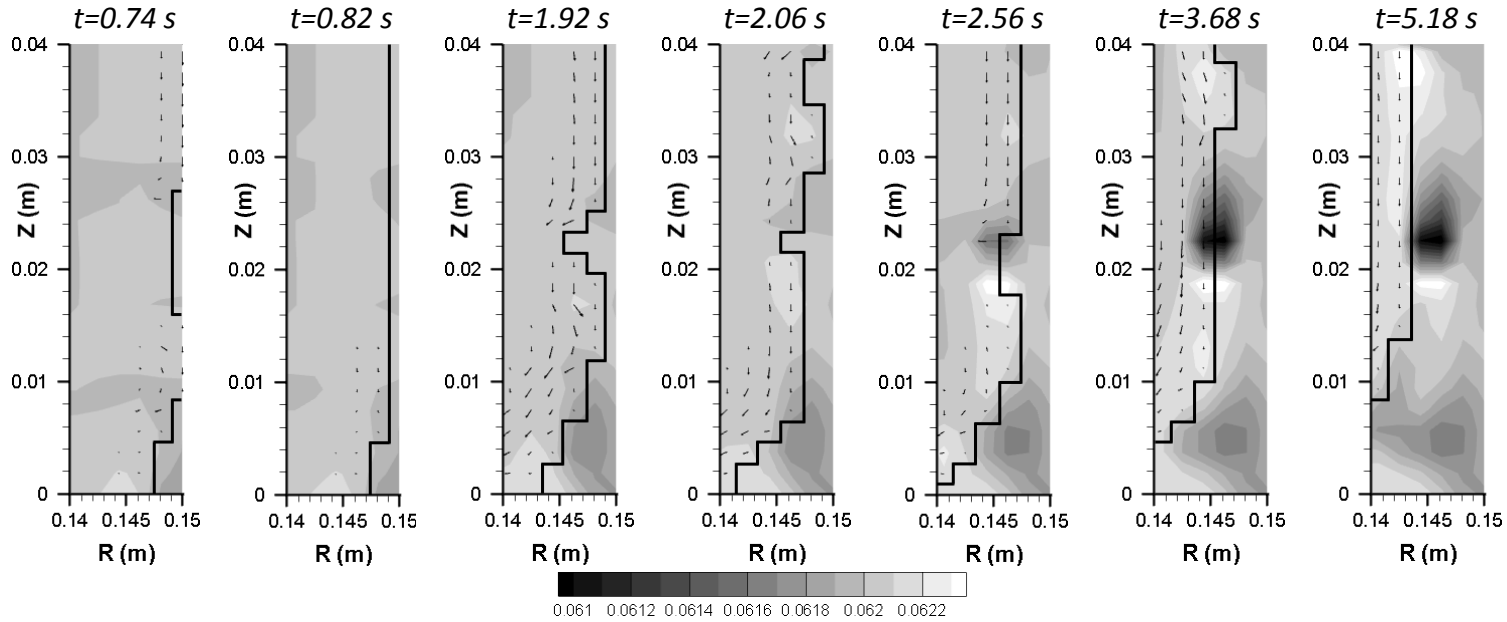

Figure 5.7: Zn composition fields in the AVM with larger heat transfer coefficients of 2500 W/m^{2}K and 1250 W/m^{2}K at the outer radius and bottom, respectively.

Figure 5.8 schematically shows a summary of the difference between packing sequences that do and do not result in channel segregate initiation and propagation. In Figure 5.8a, the rigid protrusions have an effect on the surrounding flow that causes enrichment or depletion of the downstream and upstream cells, respectively. These compositional differences that occur in the vicinity of the perturbations are frozen in place by subsequent packing events and an associated sudden decrease in the permeability and limitation in the local solute advection. Compositional differences then affect the solid fraction of the next column of cells, where depleted control volumes develop into new perturbations, allowing the channel to propagate.

However, in the packing sequence shown in Figure 5.8b in which the cells pack consecutively along the direction of the local fluid flow, the transient velocity field and local solutal transport for each cell develops in a similar way as its neighbors. The result is a smooth composition field free of channel segregates. But in order to maintain this smooth packing sequence, the length scale of the solute transport and its effect on the solid fraction field through coupling with the thermodynamic model must balance with the grid spacing over which the packing criterion is offset.

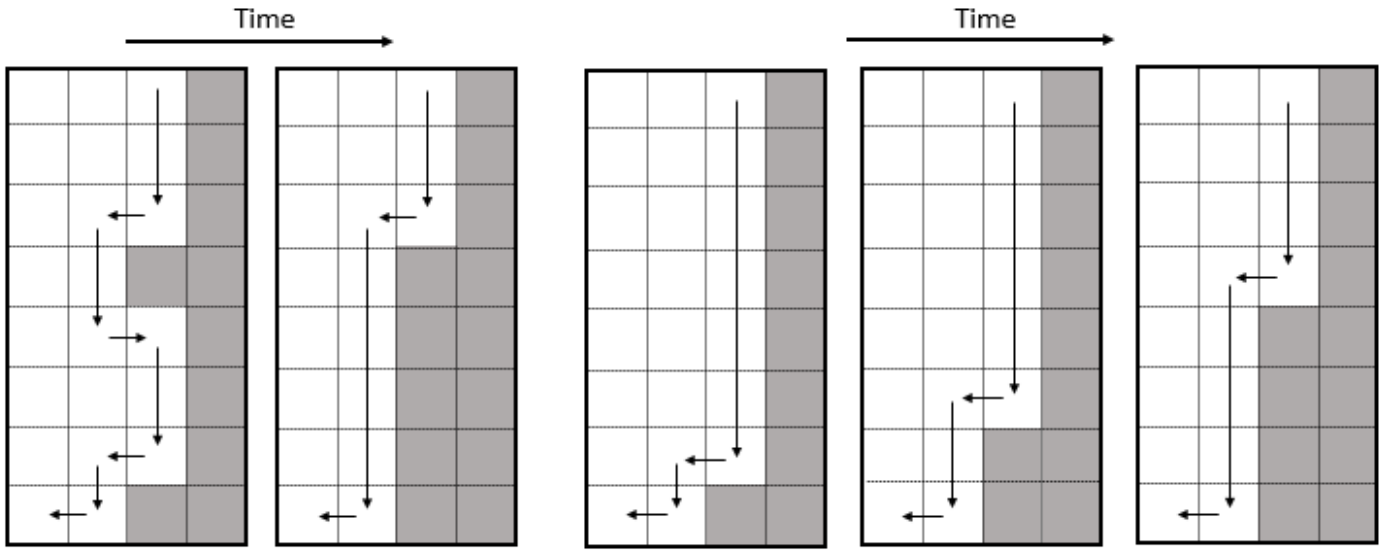

Figure 5.8: Comparison of packing sequences that (a) form channel segregates and (b) form a smooth composition field. Shaded cells are packed, and arrows indicate the general direction of the flow.

5.4 The Effect of the Permeability Model

One interesting consequence of the above proposed mechanism for channel formation is that if channels occur due to solutal advection on a cell-to-cell basis at the edge of the rigid mush, then the appearance of freckles is a function of any parameter that affects flow in these select cells. The most important subset of parameters are those that affect the permeability of these cells. If the permeability is high, then advection of enriched liquid from the rigid protrusions will occur readily. However, if the permeability of these cells is very low, then flow is essentially halted and the compositional differences characteristic of channel segregates are not able to form. In addition, the strength of the advection is a function of the thermosolutal buoyancy force driving the fluid flow. Therefore, channels are most likely to occur in regions where this driving force is high, such as near the outer radius where flow is heavily influenced by the heat transfer boundary condition. Nearer the center of the casting, the effect of thermal buoyancy is reduced and the flow slows, as can be seen by the streamlines in Figure 5.1. Because there is variation in the driving force for flow it is expected that channels will appear most readily at the outer radius, and become less prominent as the solidification front proceeds towards the centerline. Changes in the permeability at the edge of the rigid mush will interact with the liquid momentum to produce varying levels of segregation. If the proposed mechanism is correct, then a higher permeability in the rigid protrusions will cause channel formation nearer the center of the ingot while low permeability will limit their appearance to the outer radius only.

Two factors that change the permeability at the edge of the packed mush will be examined here, both within the CPF model, although the same principles may be applied to the velocity-based model as well. The first is the critical solid fraction. Physically, this parameter is related to the morphology of the grains. Highly dendritic grains will have a lower packing fraction than a globular microstructure. The morphology is subsequently affected by a variety of conditions, including alloy composition, solidification rate, and grain refiner additions [41–43]. Within the model, the selection of a particular packing fraction represents an assumption about the combined effects of these factors. A major result of changes in the packing fraction is on the permeability of a control volume when it first becomes rigid, determined here by the Blake-Kozeny model. Higher packing fractions result in a lower permeability of the cells that form the rigid perturbations that initiate channels, meaning that a larger buoyancy driving force is required for significant solute advection to occur. The effect of packing fraction on channel segregates is shown in Figure 5.9. Clearly, as the packing fraction increases, the reduced permeability at the edge of the mush limits the ability of channels to form and propagate.

Similarly, the permeability is affected by the dendrite arm spacing (λ). Increasing the DAS increases the permeability of the mush, independent of the packing fraction. Results for three λ values with a packing fraction of 0.15 are shown in Figure 5.10. Again, increases in permeability allow channels to develop further from the outer radius of the ingot, and for those channels to be more severely segregated.

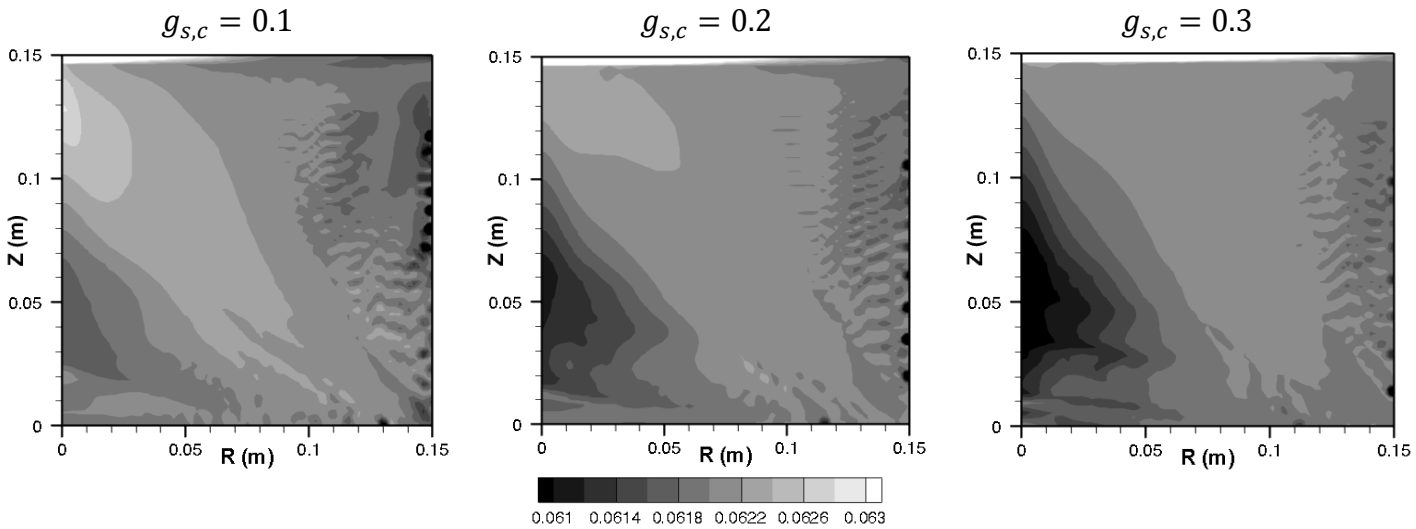

Figure 5.9: Final Zn composition fields showing the effect of changing the critical solid fraction in the CPF model.

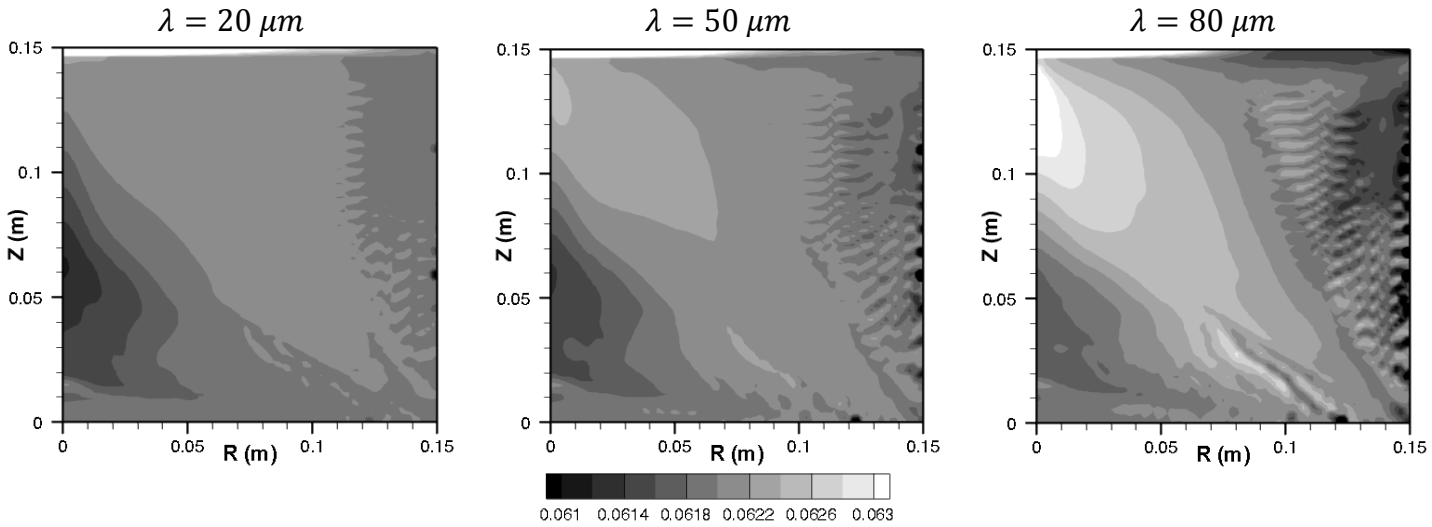

Figure 5.10: Final Zn composition fields showing the difference in channel propagation as a function of changes in dendrite arm spacing (λ) for the CPF model.

5.5 Physical Relevance and the Discrete Nature of the Packing Models

With an understanding of the mechanism behind predictions of channel formation, it is of interest to consider the physical relevance of their appearance in simulations such as those described here that utilize a mixture formulation of the governing conservation equations. It seems that the mechanism of the initiation and propagation of these channels is based on the physical phenomena described by the model. That is, they are a function of the permeability and the effect of local composition on the alloy freezing range. However, as indicated by the grid dependence (Figure 5.2 and Figure 5.3) and the discrete cell-by-cell basis upon which the mechanism for channel formation operates (Figure 5.8), the length scale over which these defects occur is set by the numerical grid.

A similar conclusion was reached for freckle predictions in continuum model of columnar solidification [82]. In that situation, channels were initiated by instabilities that are due to inaccurate solutions to the governing equations during the iterative solution procedure, and which necessarily occur on the length scale of the numerical grid. In that case, it was possible to damp the appearance of channels by tightening the convergence criterion for the energy equation. Unfortunately, such a solution is not possible in this case with free-floating solid. In columnar solidification, the permeability at the edge of the mushy zone is treated as a continuous variable and a function of the smooth solid fraction field. Therefore, the representation of the solidification front is smooth in that each cell has an average solid fraction and average permeability. In the present mixture formulation of the governing equations for equiaxed solidification, each cell is treated as either packed or unpacked without a continuum of states in between. The interface

between the slurry and rigid solid regions is therefore forced to fall on the faces of the control volumes, and the shape of the interface is only approximated on the length scale of the grid. As seen in this study, such a rough approximation has a dramatic impact on the flow field and therefore, the solute advection, causing channel initiation and propagation on a cell-to-cell length scale.

If channel formation is only due to the unnatural approximation of the shape of the interface, then a smooth interface might damp the artificial formation of channels. In multi-phase models, the transition from free-floating to rigid solid is accomplished through a single interfacial drag term that approaches Stokes' law at low solid fractions and the Blake-Kozeny permeability model at high solid fractions [49]. In this case, the interface is represented through a continuum of intermediate states, and indeed, although this particular problem has not been studied in detail, reported simulations of static castings using this method do not exhibit proliferation of extreme channels characteristic of the present mixture model [47].

Understanding of the source of such channel segregates in the context of the numerical methods hints at their physical relevance. In actual castings, packing occurs by the attachment of each grain onto the rigid interface, consistent with the negligible effect of the solid particle interactions (described by the solid viscosity) except at solid fractions near the dendrite coherency point. This attachment mechanism acts on a length scale much smaller than that of the numerical grid, both by computational necessity and by the nature of the volume averaged governing equations. The averaged nature of these simulations is acknowledged in the treatment of the solid fraction field as a continuous

variable even though the solid-liquid interface is sharp at the micro-scale. The same cannot be said for dendrite coherency because a control volume in the current schemes is not allowed to be only partially packed.

An obvious solution to the problem of these numerical artifacts is to adopt of the continuous formulation of the interfacial drag on the solid particles formulated by Wang *et al.*[49]. However, this approach requires significant information about the morphology of the equiaxed particles that, in the case of these models, is obtained via numerous supplemental relationships and the multi-phase approach. This method is therefore not easily implemented in the present mixture model, and use of a multi-phase model would increase the computational expense of macrosegregation conditions and the number of inputs that are not well known experimentally. It is unclear at this time if the difficulty and added expense of implementing such a model produces more physically accurate results. An alternative approach would be to change the treatment of the transition from free-floating to rigid solid in the context of the mixture model by allowing the source terms in the momentum equations to vary continuously within cells that are only partially packed rather than forcing these terms to be fully activated or deactivated. Such an approach is the subject of CHAPTER 6.

5.6 Conclusions

The present study has examined the appearance of channel segregates in the simulation of equiaxed solidification for a cylindrical static casting of aluminum alloy 7050.

The model used was based on a mixture formulation of the governing equations for conservation of mass, momentum, energy, and species. Two different models for grain attachment were implemented, one that assumed that grains packed at a constant and uniform volume fraction solid, and another that accounted for the local solid velocity field. In both cases, the appearance of channel segregates was found to be extremely grid dependent. Interestingly, in the case of the velocity-based packing scheme, channels were mostly suppressed for intermediate grid sizes. The mechanism for channel formation was examined in detail for both grain attachment schemes, and it was found that channels are initiated by the formation of rigid protrusions on the packed interface into the neighboring flow field, and the subsequent disruption of the solute advection. Channel propagation then occurs through the coupling of the composition field with the local solid fraction in the thermodynamic model, and the effect on the permeability of the rigid mush. This mechanism was used to explain the effect of the packing fraction and dendrite arm spacing on channel appearance. It was concluded that these channels are primarily numerical artifacts caused by the discrete nature of the packing models that result in unrealistic shapes of the interface between the slurry and rigid mush regions. The effect of this unnatural geometry on the flow field is significant, and necessarily occurs on the length scale of the numerical grid, explaining the grid dependence of channel appearance.

CHAPTER 6. A CONTINUUM GRAIN ATTACHMENT MODEL

6.1 Introduction

At the core of the mechanism for the formation of channel segregation defects in equiaxed solidification models as described in CHAPTER 5 is the misrepresentation of the shape of the interface between the slurry and rigid solid regions. When this interface is forced to fall on the boundary between control volumes, the damping effect of the permeability of the rigid solid has a dramatic effect on the local flow field and subsequently, on the solute advection. A possible solution to this problem is to break the assumption that the solid within a given cell is either completely free-floating or completely rigid, and instead, to allow control volumes at the interface to contain both states. A continuum attachment model was developed for this purpose as described in §2.2.1.3. The basis of the model is that the transition from free-floating to rigid solid is smoothed over a range of solid fractions (dictated by the packing range, Δg_s) rather than occurring discretely at the critical solid fraction $g_{s,c}$. The relative amounts of free-floating and rigid solid are described by the packed fraction P of a given cell, which varies continuously from zero to one as a function of $g_{s,c}$ and Δg_s (Equation (2.19)). The weighting function F (Equation (2.13)) is then used to control the relevant source terms

in the momentum conservation equations. In addition, solid advection at the interface is limited according to a simple modification of Stokes' law (Equation (2.23)).

The purpose of this chapter is first to explain the rational for the inclusion of a weighting function and other choices that were made during the formulation of continuum model. Additionally, the effect of the new model parameters (n and Δg_s) are evaluated and the continuum model is compared to the discrete CPF scheme. In particular, the effect of the continuum model on the formation of channel segregates is assessed.

6.2 The Sharpness of the Rigid Interface

One of the underlying assumption used in Vreeman's [71] implementation of the discrete CPF model is that the interface between the slurry and rigid solid regimes is sharp. This assumption is strongly supported by rheological measurements in solidifying alloys, in which the shear strength of the material increases sharply at the packing fraction [37–40]. Furthermore, it is consistent with the model used for the viscosity of the solid pseudo-fluid which exhibits a sharp slope as the solid fraction approaches the critical solid fraction (Figure 6.1). This result is particularly true for the more common case of dendritic solidification (i.e. relatively small critical solid fraction), although it is still a reasonable approximation even for the limiting case of spherical grains ($g_{s,c} = 0.64$). The purpose of this assumption in Vreeman's work was to rationalize the use of a representative average solid viscosity. Because the solid viscosity becomes significant compared to the liquid viscosity only in a very small region (presumably smaller than a control volume), then, it

was reasoned, its effect may be considered negligible, and the overall effect of the viscous forces between solid and liquid phases in the slurry may be approximated using a representative solid viscosity integrated over an arbitrary (i.e. 70%) fraction of the slurry region. This approach has the added benefit of eliminating the numerical complication that the solid viscosity model approaches infinity as the solid fraction approaches the critical solid fraction.

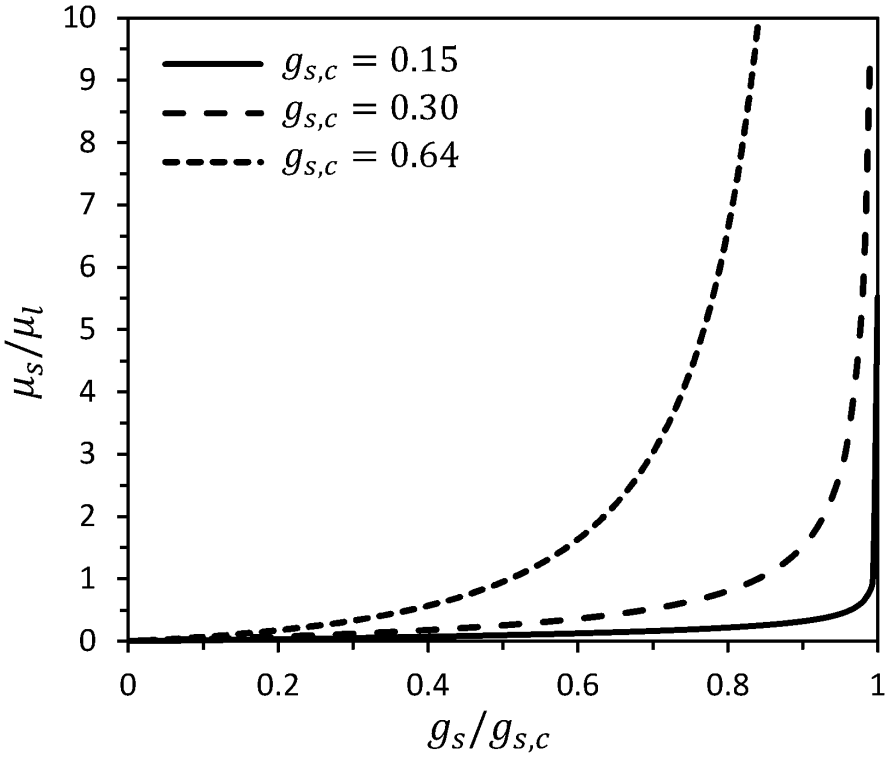

Figure 6.1: A comparison of the solid and liquid viscosities over the solid fraction range leading up to the critical solid fraction value.

However, there is one additional consequence of this assumption that was not considered by Vreeman is his formation of the packing model. If the interface between

these two regions is considered sharp on a length scale smaller than the size of a control volume, then it is inappropriate to assume that a cell transitions instantaneously from a collection of free-floating particles into a rigid solid structure. Instead, control volumes at the interface between the regions *must* be treated as if they contain some amount of both conditions. This reasoning explains why the discrete grain attachment models are not an accurate representation of the geometry of the rigid interface and the necessity for developing an alternative continuum scheme.

6.3 The Need for a Weighting Function

Next, it is necessary to justify the use of the weighting function. In order to achieve a smooth transition between the free-floating and rigid solid states, the relevant source terms in the momentum conservation equations must all be active in cells at the interface between these two regions. Through the range of solid fractions over which the transition occurs, the source terms for the rigid solid are introduced according to the value of the weighting function ($F = P^n$) while the slurry terms are removed accordingly ($1 - F$). The natural choice for this transition is a linear weighting of the terms (i.e. $n = 1$). However, the source terms involved often differ by several orders of magnitude. To demonstrate this, a simple scaling analysis of these terms was performed by considering a simplified system and replacing each variable with a representative difference.

The selected system is Cartesian, with a vertical solidification front. A summary of the simplifying assumptions used to ease the evaluation of these expression is given below:

1. The system is in Cartesian coordinates.
2. The solidification front is one-dimensional so that the vertical gradients of the fraction solid are equal to zero.
3. The solid velocity is similar in magnitude to the liquid velocity (the fourth source term for the slurry region is equal to zero).
4. The alloy under consideration is AA7050.
5. Only the primary alloying element, Zn, is considered in the solutal buoyancy terms.

By applying the above assumptions to Equations (2.9) and (2.10) and scaling the differentials, the following order of magnitude approximations are found:

$$S_{slurry} \sim \frac{-\mu_l f_s \Delta \mathrm{u}}{\Delta x^2} + \frac{\bar{\mu}_s g_s \Delta \mathrm{u}}{\Delta x^2} + g_s \Delta\rho g - g_s \rho g\left[\beta_{T,s}\Delta T + \beta_{S,s}^{Zn}\Delta C\right] - g_l \rho g\left[\beta_{T,l}\Delta T + \beta_{S,l}^{Zn}\Delta C\right], \tag{6.1}$$

and

$$S_{rigid} \sim -\frac{180\mu_l g_s^2}{\lambda^2(1-g_s)^3}\Delta u - \rho\vec{g}\left[\beta_{T,l}\Delta T + \beta_{S,l}^{Zn}\Delta C\right], \tag{6.2}$$

where Δu is a representative velocity difference, Δx a representative length scale related to the thickness of the transition from the slurry to rigid regions, ΔT a representative

temperature difference, and ΔC a representative composition difference. The purpose of this exercise is to understand the general effect of the weighting function on the relative magnitudes of these source terms through the transition region. Therefore, only order of magnitude estimates of each of these values are necessary. The values used to evaluate these terms are summarized in Table 6.1.

Table 6.1: Summary of values used to evaluate scaled source terms through the slurry to rigid transition region.

Critical Solid Fraction ($g_{s,c}$)	*0.15*
Packing Range (Δg_s)	*0.05*
Velocity Difference (Δu)	*1 cm/s*
Transition Thickness (Δx)	*1 cm*
Temperature Difference (ΔT)	*10 K*
Composition Difference (ΔC)	*1 wt.%*
Dendrite Arm Spacing (λ)	*50 μm*
Density (ρ)	*2500 kg/m^3*
Liquid Viscosity (μ_l)	*1.3x10^{-3} kg/m-s*
Avg. Solid Viscosity ($\bar{\mu}_s$)	*1.6x10^{-3} kg/m-s*
Solid Coef. Therm. Exp. ($\beta_{T,s}$)	*1.5x10^{-5} K^{-1}*
Solid Ceof. Sol. Exp. ($\beta_{S,s}^{Zn}$)	*-0.65*
Liquid Coef. Therm. Exp. ($\beta_{T,l}$)	*2.3x10^{-5} K^{-1}*
Liquid Coef. Sol. Exp. ($\beta_{S,l}^{Zn}$)	*-1.43*

The two source terms were evaluated across the transition region, and then modified by the weighting function in the same way shown in Equation (2.7). The ratio of the two terms (multiplied by negative one so that the resulting values are positive) is shown in Figure 6.2 for three different values of the weighting exponent, n. Values of this ratio greater than one indicate that the rigid source terms dominate the behavior of the

equation, while values less than one mean the slurry terms are larger. For a linear weighting function (i.e. $n = 1$), the slurry terms are prominent only near values of P close to zero, but the ratio quickly becomes much larger than one. For small values of n, the behavior of cell is within the rigid region almost instantaneously upon entering the transition region. With increasing values of n, the rigid behavior is damped at lower values of P and the cell will act more as a mixture of rigid and free-floating solid.

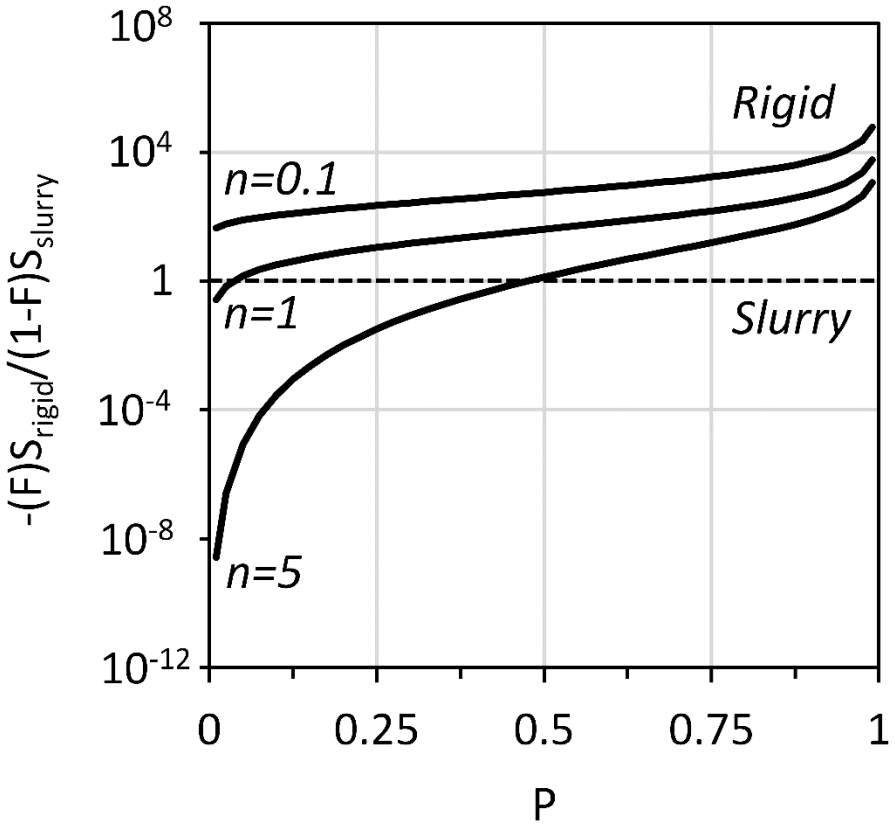

Figure 6.2: Scaled comparison of the orders of magnitude of the weighted source terms for the slurry and rigid regions through the packing range for the axial momentum equation with various values of the weighting function exponent.

Based on the data in Figure 6.2, it is clear that changing the weighting function exponent is an effective method of tuning the behavior of the transition between free-floating and rigid solid grains. However, it is difficult to determine what value of n yields the most realistic results. Instead, a range of values will be investigated and the differences between them discussed. It must be noted that the necessary drawback in adding additional details to any model such as that described here is the increased input uncertainty in any new input parameters. The uncertainty added to the model by the new parameter (n and Δg_s) will be quantified in CHAPTER 7. This complication, however, supports the use of a power-law form of the weighting function which provides a simple way of tuning the behavior of the system with the introduction of only a single new parameter.

6.4 Macrosegregation Development and Grid Dependence

Before examining the effect of the packing range and the weighting exponent, the overall macrosegregation development in the continuum model and its grid dependence is compared to the discrete CPF model for a linear weighting of the source terms. The Zn composition field, flow field, and rigid solid front position are shown for both the CPF and continuum attachment models in Figure 6.3. In both cases, the general shape of the final composition field is similar, and its development occurs in a comparable manner. The solidification front proceeds inward from the outer radius and upward from the bottom of the cavity. The combined driving forces of thermal and solutal buoyancy generate a

clockwise flow cell. The partition coefficient for Zn (and the other major alloying elements) in this alloy system is less than one, meaning that solid initially forms at a composition depleted relative to the nominal, and solute is rejected into the liquid. The first solid to form at the outer radius quickly become rigid. There is some permeability to the rigid structure, and some of the associated enriched liquid is advected away, driven by its thermosolutal buoyancy, to be replaced by fresh liquid from upstream nearer the nominal composition. The overall result is that the lowest composition in the domain, in all cases, is the first solid to attach to the vertical wall at the outer radius. As solidification continues, new depleted solid particles form near the rigid interface and are advected downward at a velocity slightly larger than that of the liquid as described by Stokes' law. The solid particles, however, resist the upward flow at the centerline of the cavity, resulting in a depleted region here near the bottom of the domain. The settling motion of the solid particles displaces the associated enriched liquid, causing an enriched region to form at the top of the domain.

There are, however, some marked differences between the two models. One of the primary effects of the range of solid fractions over which the continuum model transitions from free-floating to rigid solid is a gradual introduction of the permeability source term which acts to damp the flow. Therefore, the flow cell in the continuum model is slightly weaker than that of the discrete model. This gradual slowing of the solid also has an effect on the composition field. As the particles flow down the vertical solidification front they are slowed and tend to collect at the corner in the bottom right of the slurry region. The associated enriched liquid, however, continues to move through the permeable solid. The

result is a depleted region that extends upwards and inwards from the bottom right corner of the domain with a neighboring enriched region that runs in parallel. Generally, the flow of enriched liquid through the relatively permeable solid in the regions near the bottom of the packing range is an effect that does not exist in the discrete model and accounts for much of the difference in the composition fields. This effect allows for more enriched liquid to flow from the edge of the mush into the bulk fluid, as is clearly evidenced by the greater enrichment of the slurry and liquid regions through the process in Figure 6.3.

While the subtle effects of the continuum attachment model on the general shape of the composition field are of interest, the most notable difference from the discrete packing model is the absence of channel segregate defects. As described in CHAPTER 5, these defects are primarily a numerical artifact. It was concluded that the mechanism behind their formation was the unnatural representation of the interface between the rigid and slurry regions in the discrete models because it was forced to fall on the boundaries between control volumes, and the extreme effect of the difference in permeability on either side of the interface on the fluid flow and subsequent solute advection. Part of the motivation for developing the continuum model was to improve the representation of this interface, and from Figure 6.3, it appears that this change has a dramatic effect on the formation of these channels.

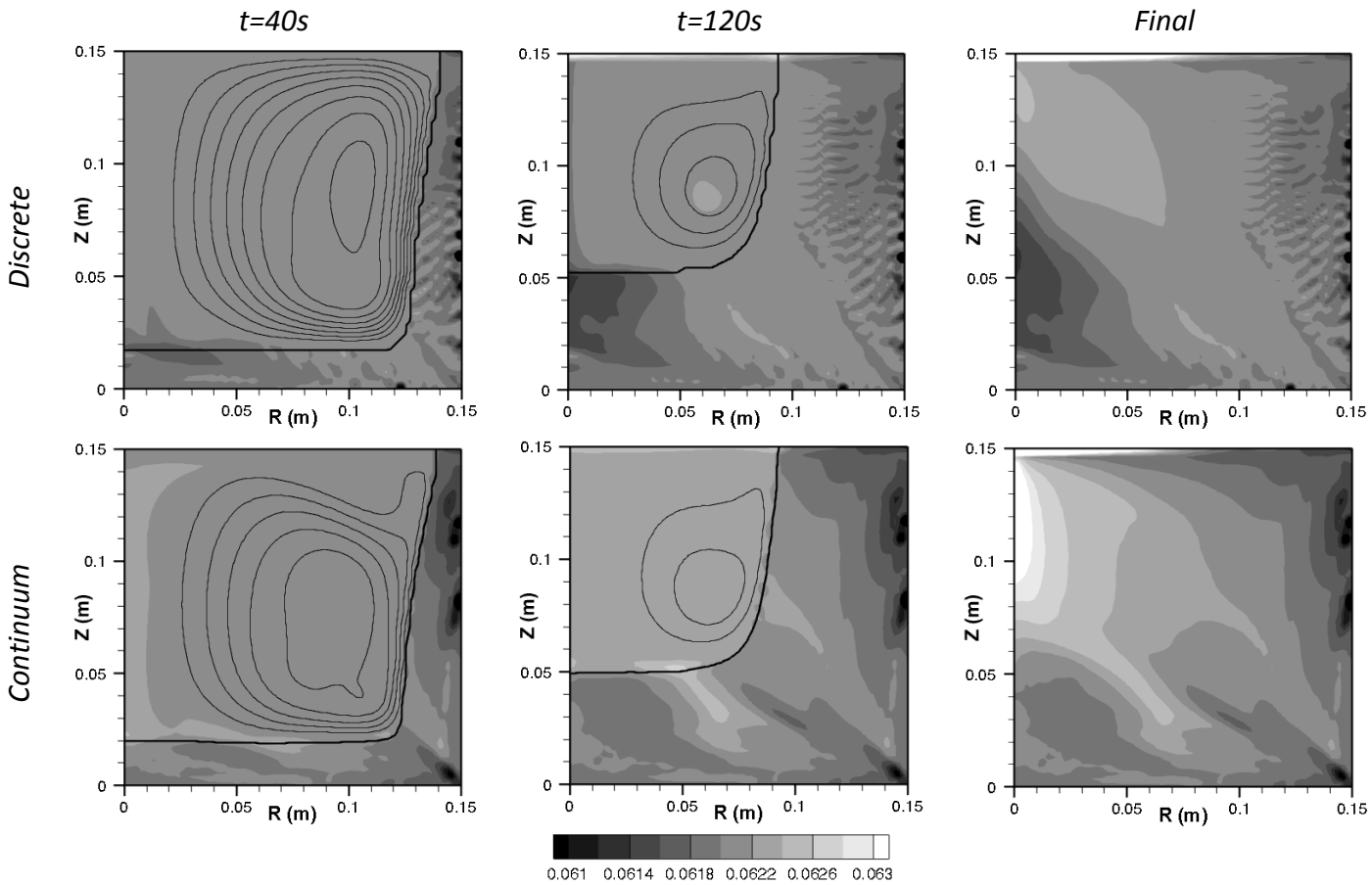

Figure 6.3: Zn compositions fields at intermediate times during the process for the discrete and continuous packing models. The dark line shows the interpolated $P = 0.5$ interface, and the lighter lines are streamlines varying from 0.02 to 0.22 kg/s in 0.02 kg/s increments. Simulations were performed with an 80x80 numerical grid.

Next, it is important to determine whether the suppression of channel segregates is grid dependent, and overall, whether the grid dependence of the continuum model is an improvement over the discrete model. A grid study is shown in Figure 6.4 for both model types. First, it is apparent that the continuum attachment model maintains a comparatively smooth composition field throughout the range of grid sizes studied, although some sites of instability are seen for the finest grid. On the other hand, the channel segregates in the discrete model are severe in all cases, and their spacing is very grid dependent. The advantage of the continuum model then, is that refinement of the grid appears to add more detail to the composition field without also generating additional numerical artifacts that obscure the solution. This conclusion can be supported by examining the normalized Weibull deviation over a range of grid sizes, as shown in Figure 6.5. Here, the results of both model types share similar trends, but the continuum model is clearly much less sensitive to change in the grid. The remaining results in this study were produced using an 80x80 numerical grid.

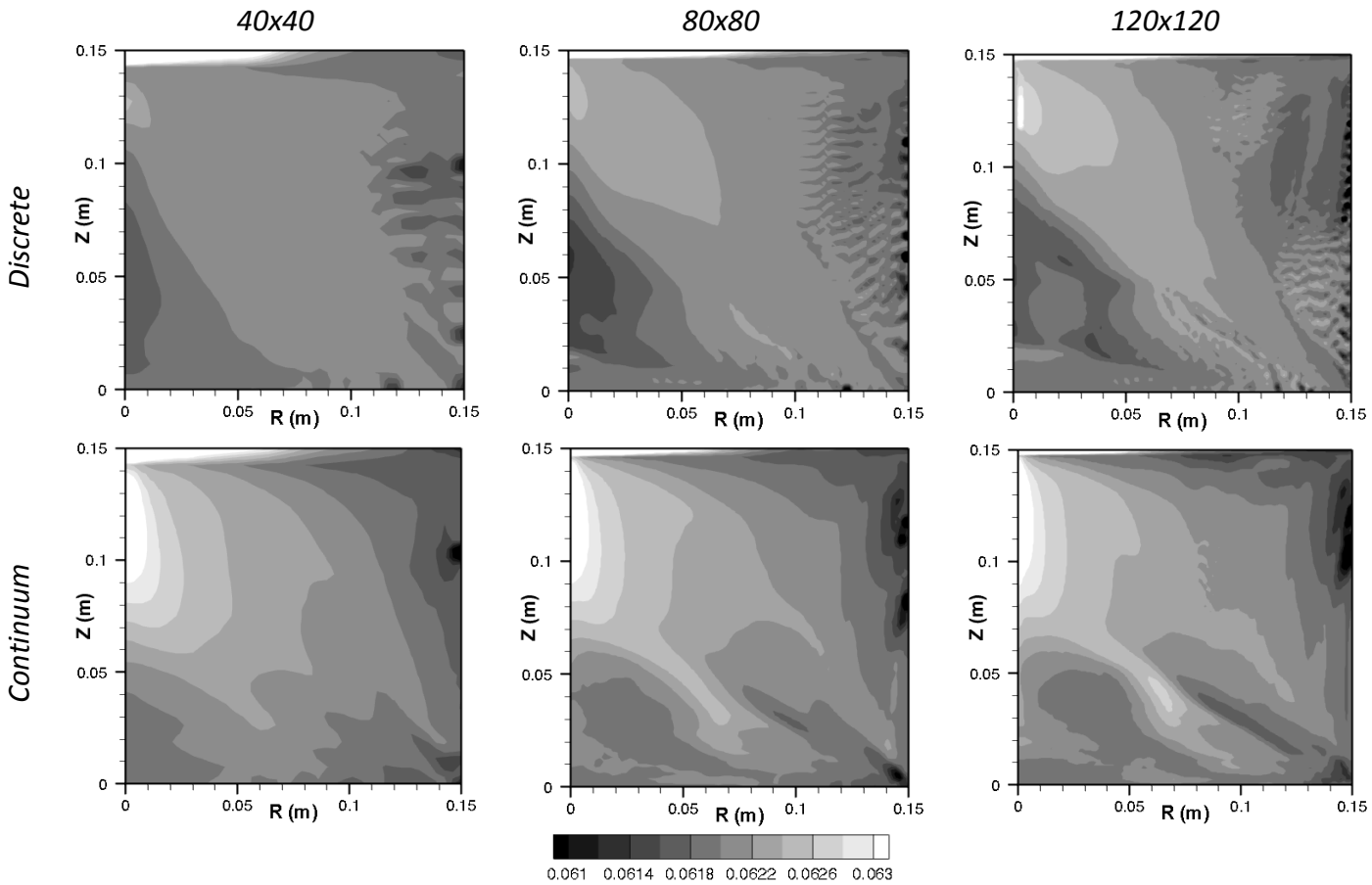

Figure 6.4: Comparison of the grid dependence of the final Zn composition field for the discrete and continuous grain attachment models.

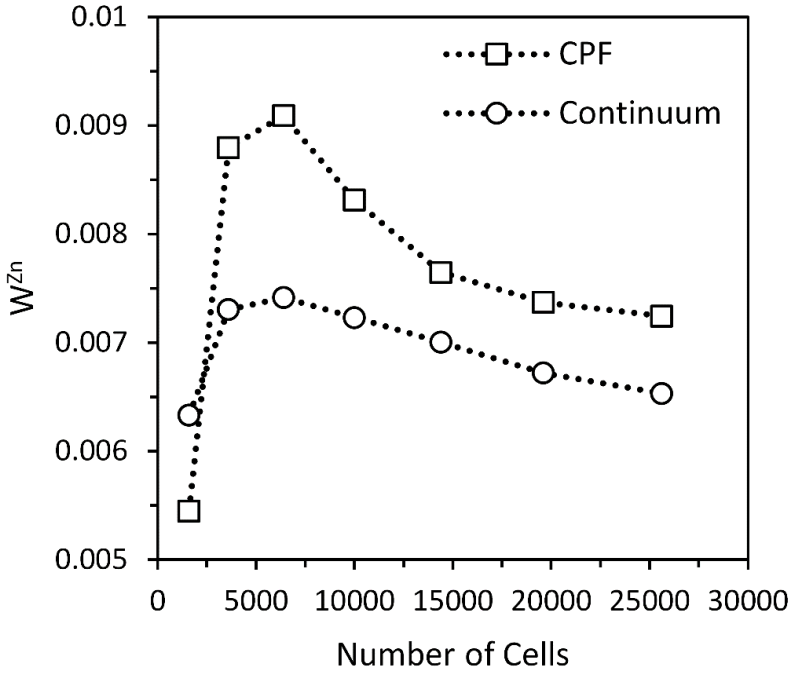

Figure 6.5: The normalized Weibull deviation for the final Zn composition field for the discrete and continuum attachment models as a function of the number of numerical cells.

6.5 The Effect of the Weighting Function Exponent

In the above results, only a linear weighting function ($n = 1$) was used. In this case, the weighting function is simply equal to the packed fraction. However, as shown in Section 6.3, other values of n may more accurately represent the transition from free-floating to rigid solid. One complication of using weighting exponents other than unity is the calculation of the solid velocity using Stokes' law. In Equation (2.23), the solid velocity across the boundary between two cells is multiplied by $1 - P$, where P is the packed fraction at the control volume interface. However, it is also possible that using the weighting function (i.e. $1 - F$ instead of $1 - P$) is the appropriate multiplier of Stokes'

law. To this point, using a linear weighting function has made this choice immaterial because the weighting function is simply equal to the packing fraction. However, if exponents other than one are to be used, the effect of using either of these modification must be evaluated.

To begin with, Stokes' law was changed to be modified by the weighting function, and various values of the weighting exponent were tested. The final Zn composition fields for these cases are shown in Figure 6.6. For small values of n, this approach begins to produce channel segregates similar to those in the discrete attachment model. This effect is because at small values of *n*, the solid velocity quickly approach zero near the low end of the packing range, returning to the sudden transition between slurry and rigid states that is characteristic of the discrete model.

Interestingly, for large values of n, the segregation near the outer radius begins to reverse from being primarily depleted to enriched. The reason for this change in segregation pattern is the effect of the weighting function on the relative solid and liquid velocities. The permeability term in the momentum equations quickly becomes large even for relative high values of n. On the other hand, Stokes' law is affected in a much more direct manner. The result is that for large values of n, in regions near the edge of the mush, the restraining effect of the permeability terms actually causes the liquid to move more slowly than the solid. Essentially, enriched liquid is immobilized at the outer radius while the depleted solid is advected away. This situation is obviously not physically realistic because it is essentially acting as if the liquid is becoming rigid rather than the solid.

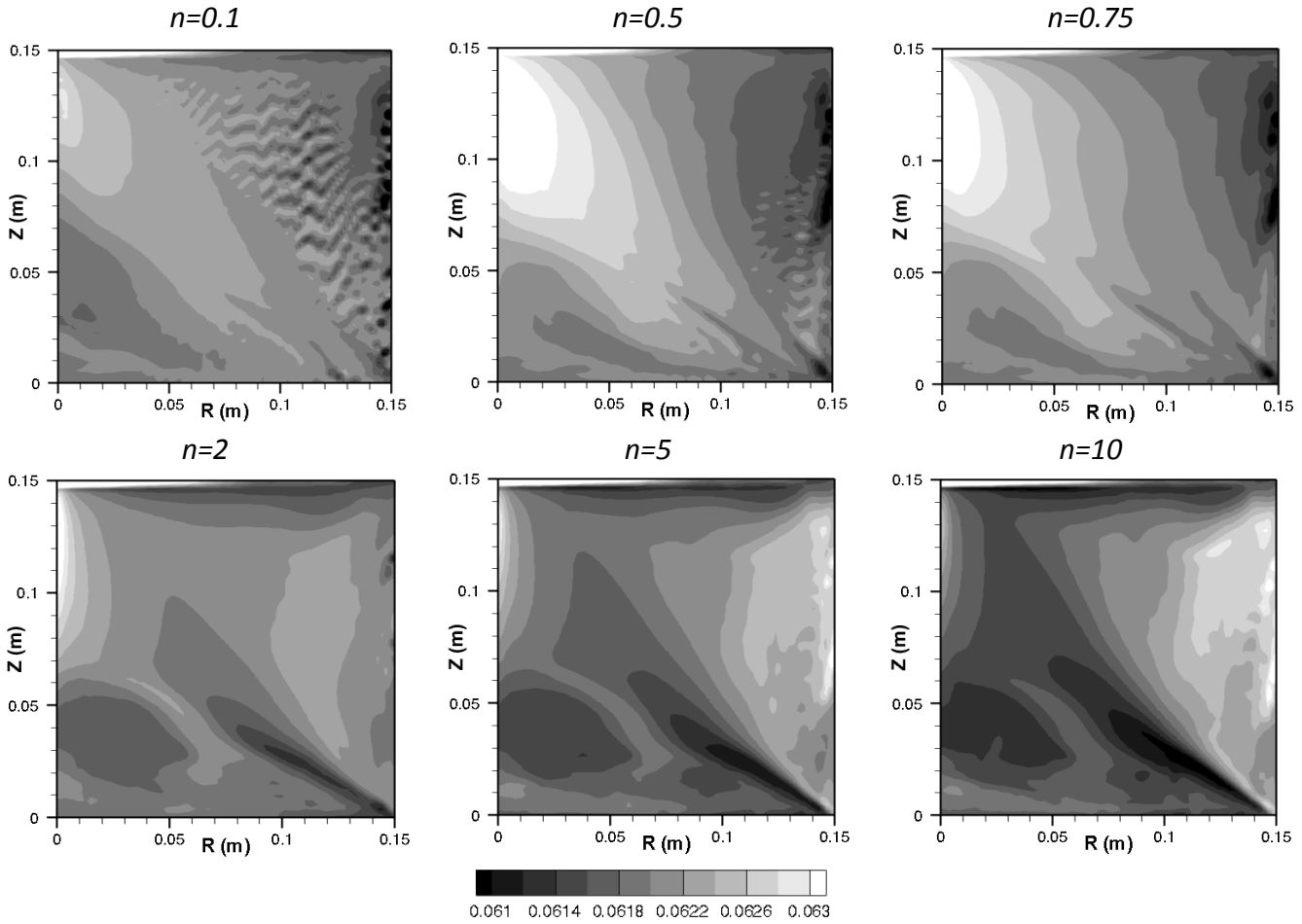

Figure 6.6: The effect on the final Zn composition field of changing the weighting function exponent when Stokes' law is multiplied by $1 - F$.

If instead, the packed fraction is used to modify Stokes' law, then the effect of the weighting exponent is as shown in Figure 6.7. In this case, the level of packing within a given control volume has a direct relationship with the flow rate of solid in and out of that cell. This approach is more physically meaningful on a conceptual level. For example, if a cell is half packed, then across a given boundary, the flow rate of solid will be half of that if the cell was unpacked. Using the weighting function for Stokes' law would, in this case, predict too low of a flow rate for weighting exponents less than one, and too high of a flow rate for exponents greater than one. The result of using the packed fraction in Stokes' law is clear in Figure 6.7, in that the changes in the weighting exponent do not change the shape of the composition field, but only the magnitude of the segregation. Changes in the level of segregation are easily explained by the relationship of the weighting function to the permeability term. For large values of n, the permeability term is damped near the lower end of the packing range, allowing a greater amount of enriched liquid to flow out of the edge of the mush. Decreasing the value of n causes this flow to be more quickly cut off, reducing the relative motion of solid and liquid that causes macrosegregation. Lastly, this approach has one more obvious advantage over the use of the weighting function in Stokes' law in that channel segregates do not begin to form at small values of n.

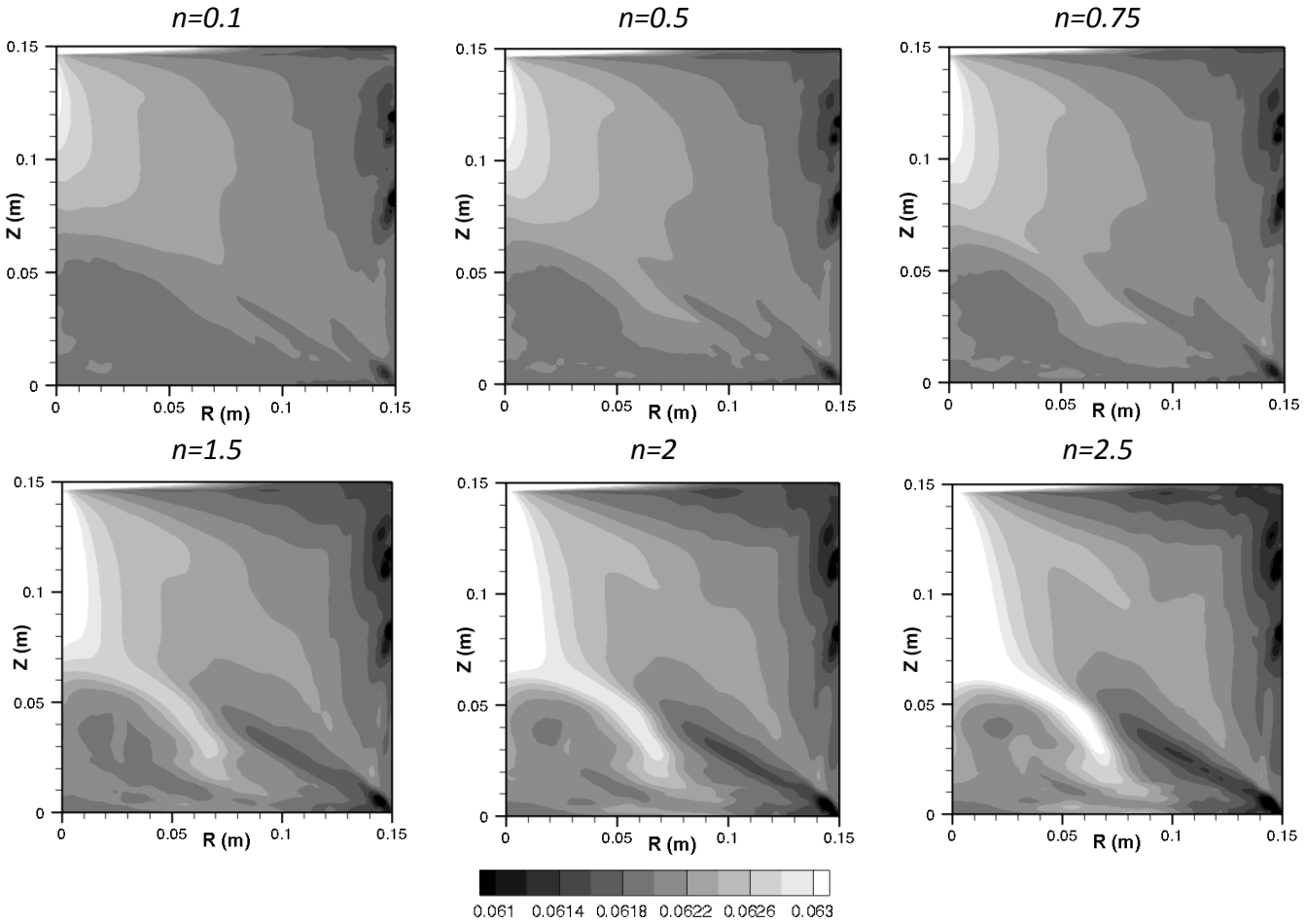

Figure 6.7: The effect on the final Zn composition field of changing the weighting function exponent when Stokes' law is modified by $1 - P$.

The effect of the weighting exponent on the normalized Weibull deviation for both versions of Stokes' law are shown in Figure 6.8. When the weighting function is used, the two segregation regimes are clearly visible with a transition region between them. For small values of the weighting exponent, the system acts similar to the discrete model with a critical solid fraction value near the bottom end of the packing range, and in these cases, the segregation is significantly impacted by the presence of channel segregates. At higher exponent values, the macrosegregation is dominated by the motion of solid particles, while the liquid is (erroneously) restricted by the permeability terms in the momentum equations. For exponent values near unity, there is a transition between these two behaviors. When the packed fraction is used in Stokes' law, the solid velocity is always affected similarly over the packing range, but changes in the weighting exponent adjust how strongly the permeability of the solid affects the fluid flow. Basically, low values of the exponent increase the effect of the permeability of the mush, while large values reduce this effect.

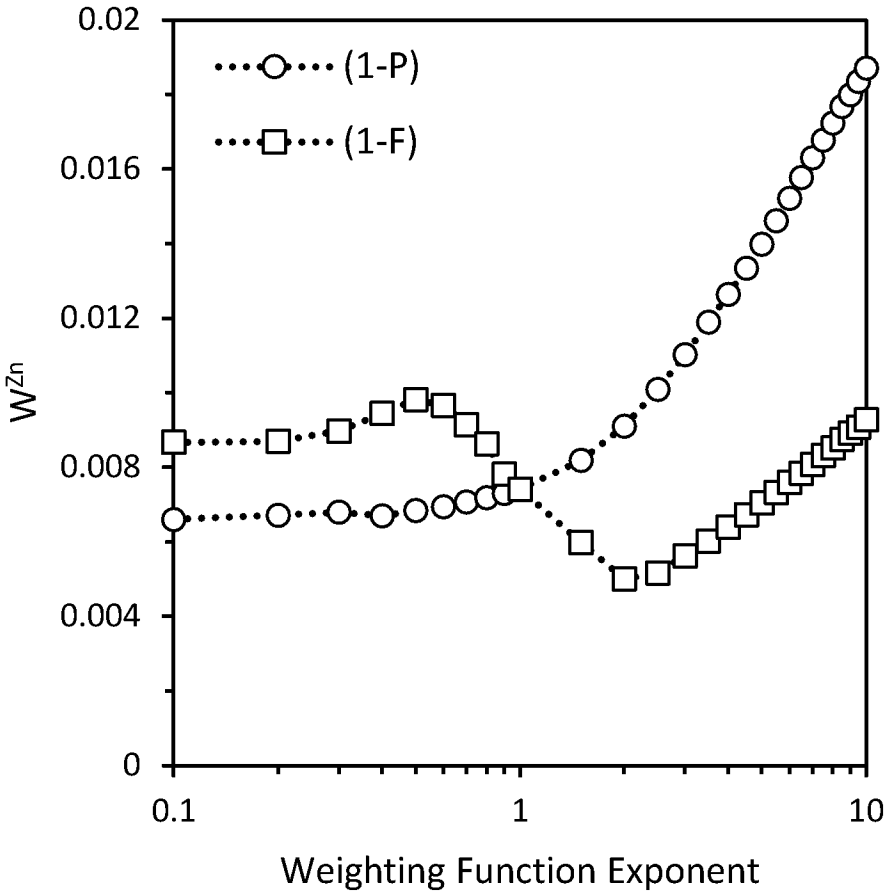

Figure 6.8: The effect of the weighting function exponent on the normalized Weibull deviation for the final Zn composition field for each of the possibilities for weighting Stokes' law.

6.6 The Effect of the Weighting Range

The other parameter introduced in the continuum model is the range of solid fractions over which the weighting function is applied, Δg_s. A larger value will result in a more gradual transition between the free-floating and rigid solid states, while it is expected that very small values will begin to approach the discrete model in which the

transition occurs very suddenly. These results are confirmed by the final Zn composition profiles shown in Figure 6.9. For a small packing range of 0.01, the channel segregates that are characteristic of the discrete model begin to reappear.

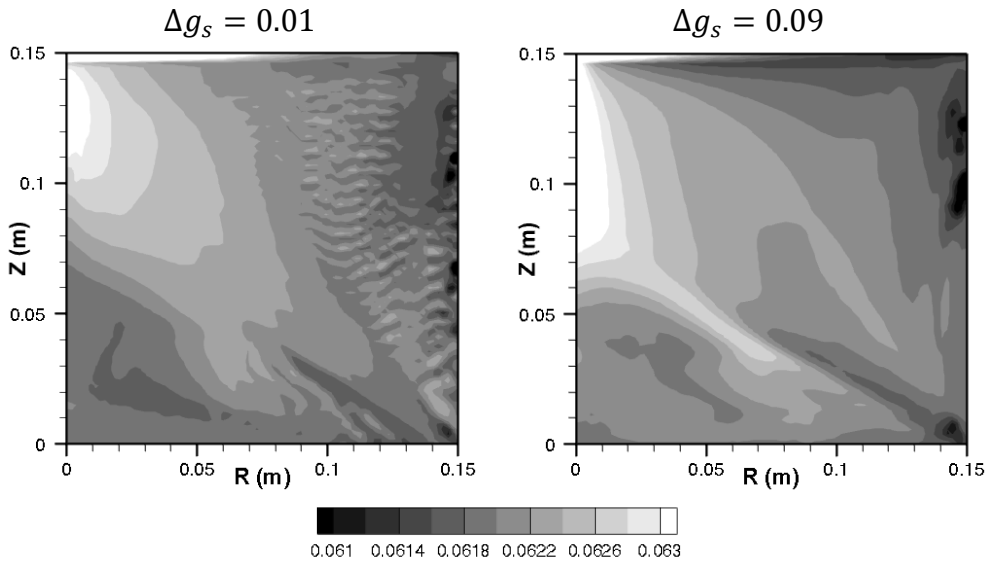

Figure 6.9: The effect of changing the range of volume fraction solid values over which the weighting function is applied on the final Zn composition field.

For larger ranges, the composition field is significantly smoother. For a given critical solid fraction, $g_{s,c}$, it is expected that larger packing ranges will damp the flow via increases in the magnitude of the permeability term in the momentum conservation equations over a larger portion of the domain. The result of this increased damping of the flow is an overall weaker flow cell, a reduction in solute advection, and therefore, generally less macrosegregation. These results are shown in Figure 6.10 for the normalized Weibull deviation of the final Zn composition fields as a function of the

packing range for a constant critical solid fraction of $g_{s,c} = 0.15$. Clearly the general trend is a decrease in segregation with packing range. The appearance of channel segregates also contributes to the spike in these values for small packing ranges.

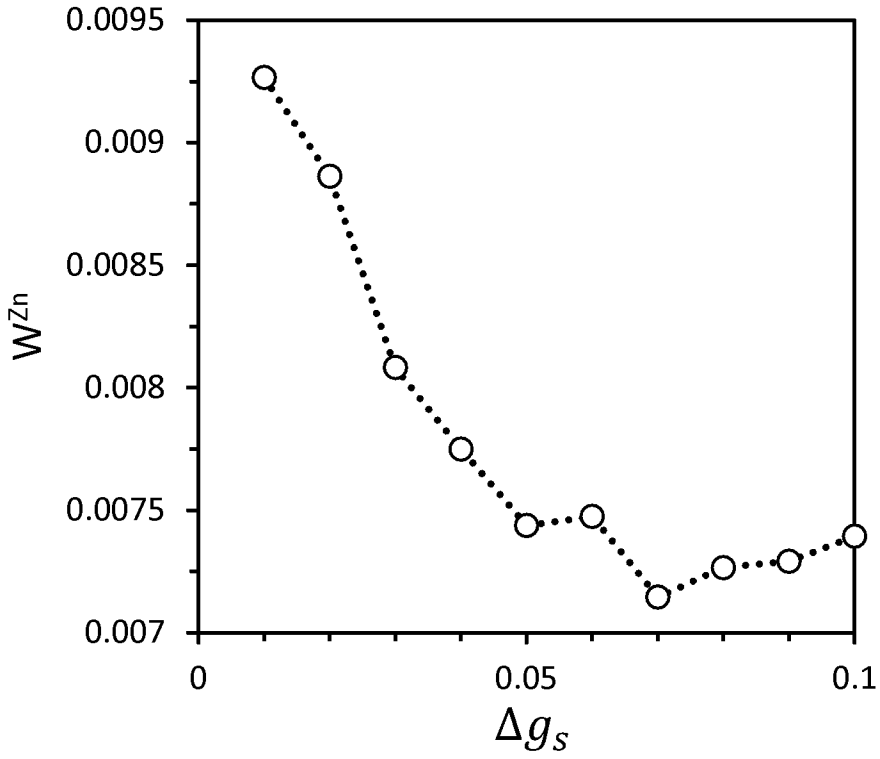

Figure 6.10: The effect of changes in the weighting range on the normalized Weibull deviation for the final Zn composition field.

6.7 Conclusions

In CHAPTER 5, the discrete nature of packing criteria in numerical simulations of equiaxed solidification had been identified as a fundamental mechanism causing

numerical artifacts in fluid flow and macrosegregation predictions. The present work introduced a continuum grain attachment model in an attempt to suppress these numerical artifacts, and was largely successful in doing so. Previous models had assumed that each cell in the numerical domain contained solid that was either fully free-floating or fully rigid, an assumption that lead to a poor prediction of the shape of the interface between the two regions and dramatic effects on the fluid flow and solute advection. The present model allows cells to be partially packed by treating the packing criterion as a continuum over a finite range of solid volume fractions. The core of this approach is to use a weighting function to control the relative magnitudes of the source terms in the momentum conservation equations. The flow of solid is also adjusted throughout the packing range via a simple modification to Stokes' law. This approach has successfully suppressed the formation of erroneous channel segregates to produce smooth composition fields.

There are two main disadvantages to the new model. The first is that the form of the weighting function in this case was assumed to be a power-law relationship with the packed fraction within a given control volume. This choice allows for significant flexibility through the choice of the weighting exponent, but it is unclear if other forms of the weighting function might yield more realistic results. Second, by introducing parameters that control the weighting function (in this case, the weighting exponent n and the range of solid fractions over which the model is applied, Δg_s) uncertainty in the values of these parameters is also introduced to the model. In CHAPTER 7, the CPF, AVM and continuum attachment models will be compared in the context of the uncertainty of the model inputs.

CHAPTER 7. QUANTIFICATION OF EPISTEMIC UNCERTAINTY IN GRAIN ATTACHMENT MODELS FOR EQUIAXED SOLIDIFICATION

7.1 Introduction

Based on the work presented in the preceding chapters, there are now several choices of possible grain attachment models that may be used for simulating equiaxed solidification using the mixture formulation: constant packing fraction, velocity based, and continuum. While results thus far have demonstrated the differences in these models for a relatively small set of cases, it is unclear whether these models actually make different predictions over a wider range of inputs, and if they do make different predictions, if any one model is more physically realistic than the others. This type of uncertainty is referred to as epistemic, or reducible, in that improved knowledge of the physical system through careful experimentation would theoretically enable determination of which model is the most accurate. Unfortunately, such validation data is not presently available. Moreover, the uncertainty in which attachment model to select is complicated by the uncertain nature of other model inputs. Essentially, the predictions from one model may not be significantly different from another when taken in the context of uncertainty in input parameters, including the dendrite arm spacing, critical solid fraction, free-floating particle size, material properties, and boundary conditions.

Here, three grain attachment models (CPF, AVM, and continuum) will be compared by obtaining output distributions for each and quantifying the likelihood that a given output will be the same for the different models. If these models produce largely similar results, then the focus of future research must be on obtaining more accurate input data or other model improvements that narrow the output uncertainty bands, or, if the level of uncertainty is acceptable, then the model that is most convenient from a numerical perspective may be selected. If, however, the models produce very different results, then emphasis should be put on obtaining validation data to support the selection of one model over another.

To this end, this chapter has two main objectives related to the epistemic uncertainty of the grain attachment models. First, what is the magnitude of the effect of the velocity field on macrosegregation predictions? If the constant packing fraction and velocity-based models produce the same outputs, then the inclusion of the solid velocity field in the packing criteria may be safely neglected. Otherwise, it is implied that the velocity field has a significant effect on grain attachment and the resulting macrosegregation, and the velocity-based model should be compared to corresponding validation data. Second, does the continuum packing model produce different results than the constant packing fraction model? (The continuum packing model is not compared to the velocity based model in this case because the continuum approach is not intended to account for the velocity field.) There are several interesting components of this objective. First, the continuum scheme is not intended to produce significantly different results from the constant packing fraction model, only to eliminate unwanted

numerical artifacts. Therefore, it is of interest if the outputs are also changed significantly as a result. Second, what is the effect of the new parameters introduced with the continuum model that do not apply to the discrete models? If the model is very sensitive to these parameters, then the overall distribution of the outputs may widen significantly, representing a need for new information about the appropriate values of these parameters.

This chapter will begin by describing the methods used for uncertainty quantification. A preliminary analysis of the three models will be performed using uncertainties in a wide variety of model inputs to identify those that are the most important. Using this information, the computational expense of the uncertainty analysis will be improved by limiting the input uncertainties to only those parameters to which the models are the most sensitive.

7.2 Description of Uncertainty Quantification

The PRISM center at Purdue University developed the PRISM Uncertainty Quantification (PUQ) [63] framework as an alternative to direct Monte Carlo sampling for propagating uncertainty in computationally expensive models. PUQ uses the Smolyak sparse grid algorithm to select a comparatively small number of model configurations from the input probability distributions and fits Legendre polynomials to the resulting outputs using generalized polynomial chaos (gPC). The number of data points in the sparse grid correspond to the order of the polynomial response function. A level 1 sparse grid fits a linear function for each of the input parameters, a level 2 fits a quadratic

function, etc. The quality of fit of the response surface to the model data is quantified using the root mean squared error (RMSE). Latin hypercube sampling of the response surface is used to construct the output probability distribution function (PDF). The first advantage of this approach is that it is non-intrusive, in that it does not require any changes in the underlying simulation in order to propagate uncertainty through the model. The second is a considerable savings in computation time because the model need only be evaluated at selected points based on the sparse grid algorithm and the sampling required for construction of the output distribution is performed exclusively on the inexpensive surrogate model.

The primary results from the uncertainty quantification are the probability distribution of output parameters and the sensitivities of the outputs to each of the inputs. The output PDFs are calculated by sampling from the response surface. The sensitivities are calculated using the elementary effects method [83,84]. In this approach, an elementary effect is the partial derivative of the output of interest with respect to a particular input as calculated between a neighboring pair of points in the sparse grid. The mean sensitivity, u^*, is non-dimensional (normalized by the PDF range for the input in question to allow comparisons between inputs), positive, and calculated using an arithmetic average of the associated elementary effects. Any higher order effects caused by a non-linear output relative to that input, or interacting effects with other inputs, are characterized by the standard deviation of the elementary effects, σ^*. For k neighboring pairs of points for a given input (with all other inputs being held constant), the mean sensitivity may be expressed as

$$u^* = \frac{\Delta x_{input}}{k} \sum_{i=1}^{k} \left| \frac{\Delta y_i}{\Delta x_i} \right| \tag{7.1}$$

where Δx_{input} is the normalizing range for the input probability distribution of interest (equal to 6.15 times the standard deviation for a Gaussian distribution), Δy_i the difference in outputs for the ith pair of points, and Δx_i the difference in the input variable for the ith pair of points. Note that these point are taken directly from the model solutions on the sparse grid and therefore, the sensitivity results are independent of the fitted surrogate model.

For this study, it is of interest to quantitatively compare the output distributions of the various grain attachment models. To do so, the Bhattacharyya coefficient will be used to describe the amount of overlap between two output distributions. For two continuous distributions *p* and *q*, both with respect to an output variable *x*, it is defined as:

$$BC(p, q) = \int_{-\infty}^{\infty} \sqrt{p(x)q(x)}\, dx \tag{7.2}$$

The coefficient varies from zero to one, in which a value of one indicates two identical distributions, and a value of zero two distribution that do not overlap at all. The output distributions in the present study are not continuous since they consist of discrete bins of data. Additionally, these bins are not of equal size or location between different

distributions. As a result, Equation (7.2) is calculated by numerical integration over the two distributions, using a step size much smaller than either bin size and representing each bin as a constant value over its width.

This discussion of uncertainty quantification so far applies generally to any output of interest. To make the analysis specific to macrosegregation necessitates some metric to describe the composition field. Here, the normalized Weibull deviation of the final Zn composition fields for AA7050, as described in §2.5, will be used.

7.3 Initial Uncertainty Quantification

The mean case used for this uncertainty analysis is the same as presented in Figure 2.4 using the properties for AA7050 given in Table 2.1. The responses of the three models (CPF, AVM and continuum) for this case with an 80x80 numerical grid are shown in Figure 7.1. For the continuum model, a weighting exponent of unity and a packing range of 0.05 are shown. In all cases, because the partition coefficient for Zn is less than one (true for the three main alloying elements), the first solid to form at the outer radius is depleted. Thermosolutal buoyancy drives a flow cell that develops in a clockwise direction. The magnitude of the flow is similar for the CPF and AVM schemes, but slightly slower for the continuum model due to a gradual introduction of the permeability term at solid fractions below $g_{s,c}$. As the rigid solid advances upwards and to the left, the flow carries enriched liquid from the rigid interface into the bulk, replaced by liquid from upstream nearer the nominal composition. Solid is also advected in the flow cell, but the downward buoyancy of the dense solid particles resists the upward flow at the centerline, resulting in a

depleted region caused by particle settling. This solid motion displaces an associated amount of enriched liquid, which eventually collects at the top of the domain and becomes the last solid to freeze.

The general trends in the final composition fields are largely similar for the three attachment models. The largest differences are in the channel segregates that tend to form near the outer radius. These channels are the most severe in the CPF model. They are suppressed for this particular case in the AVM model, but as demonstrated in CHAPTER 5, tend to reappear for different grid sizes or changes in boundary conditions. The continuum model, as discussed in CHAPTER 6, mostly suppresses these channels over a wide range of conditions.

In order to use PUQ to compare the grain attachment models, some decisions must be made on the inputs of interest and their probability distributions. Because the differences between the grain attachment models are the main concern of this study, inputs that directly relate to grain attachment are of the greatest interest. However, differences between the grain attachment models are negligible if uncertainties in the material properties and boundary conditions affect the result much more than the attachment models do. Unfortunately, the solidification model is too computationally expensive to consider a large number of parameters at once, due to an increase in the number of data points required by the sparse grid algorithm. Therefore, the best approach is to first use a low level uncertainty analysis to determine the importance of the grain attachment inputs relative to material properties and boundary conditions, and then to reduce the number of inputs in order to perform higher level analyses.

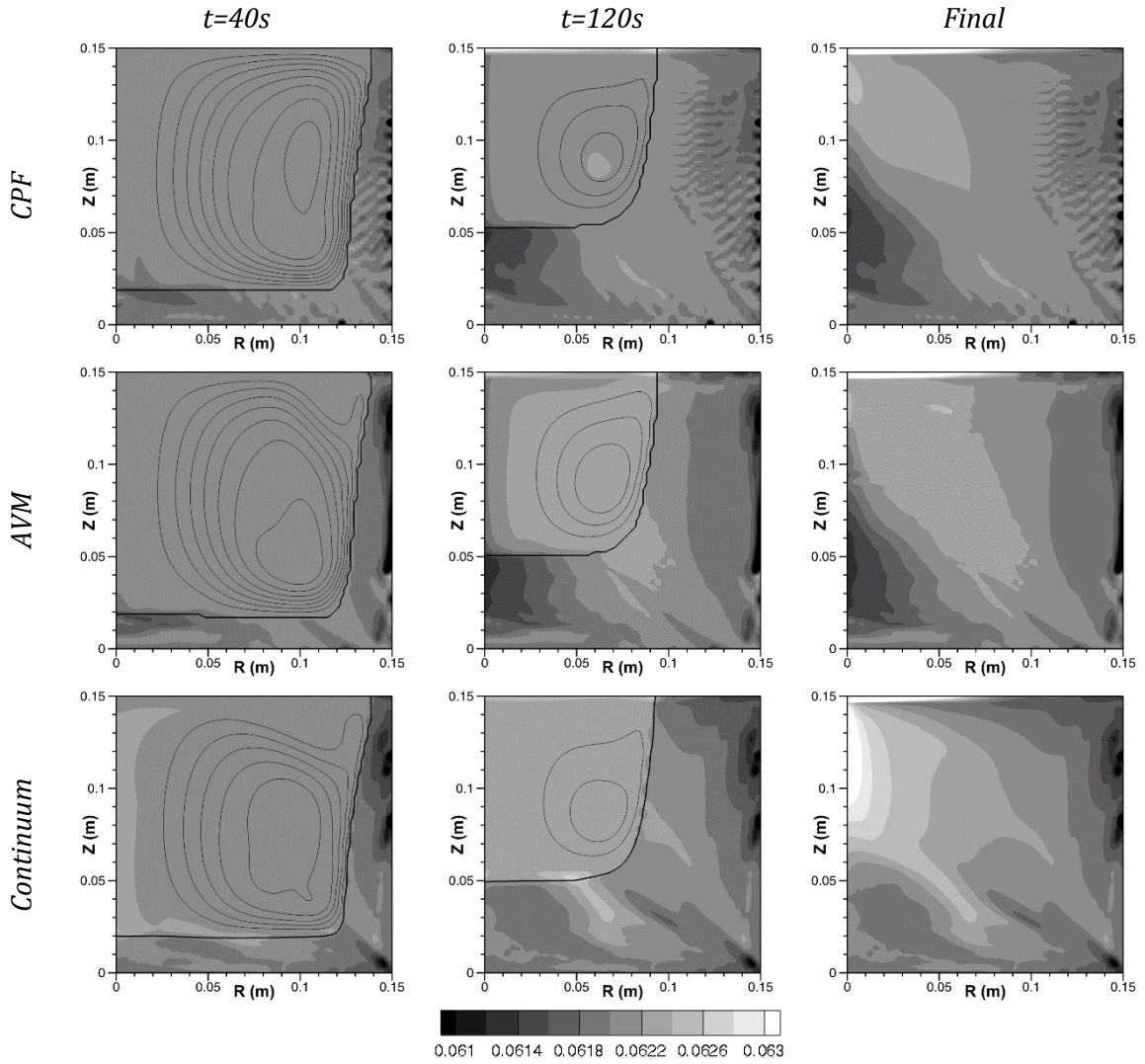

Figure 7.1: Zn composition fields at intermediate times during the process for the discrete and continuous packing models. The dark line shows the interpolated *P*=0.5 interface, and the lighter lines are streamlines varying from 0.02 to 0.22 kg/s in 0.02 kg/s increments. Simulations were performed with an 80x80 numerical grid.

Normal distributions were chosen to represent all of the inputs because they only require two parameters (mean and standard deviation) and using mean values equal to those given in Table 2.1 and Figure 2.4 means that the most probable outcome is that shown in Figure 7.1. The inputs that will be considered for level one analysis and the parameters of their probability distributions are given in Table 7.1, divided into categories for grain attachment, material properties, and boundary conditions. The primary inputs that affect solid motion and grain attachment are the packing fraction, the average particle size, and the dendrite arm spacing. These parameters are assumed uniform and constant throughout the domain, but due to local difference in cooling conditions, composition, and the number and size of grain refiner particles, in reality, they may vary widely. Therefore, fairly large standard deviations were selected for these input distributions (Table 7.1). The material properties and boundary conditions, while not known with complete accuracy, do not vary throughout the domain. Therefore a somewhat arbitrary choice was made to give these inputs standard deviations equal to five percent of the mean value. The probability distributions for each input parameter are summarized in Table 7.1. For the purposes of this analysis, the weighting range and weighting exponent for the continuum model are assumed constant, where $n = 1$ and $\Delta g_s = 0.05$.

Table 7.1: Input probability distribution parameters.

Variable Type	Input Variable	Distribution Parameters	
		Mean	**Std. Dev.**
Attachment Model	$g_{s,c}$ (CPF and Cont.)	0.15	0.0375
	$g_{s,c}$ (AVM)	0.175	0.04375
	d (μm)	30	5
	λ (μm)	50	10
Material Properties	k_s (W/m K)	149.4	7.47
	k_l (W/m K)	83.2	4.16
	c_p (J/kg K)	1141	57.05
	ρ (kg/m^3)	2515	125.75
	Δρ (kg/m^3)	-229.1	11.45
	μ (Pa-s)	$1.3\text{x}10^{-3}$	$6.5\text{x}10^{-5}$
	L_f (J/kg)	$3.75\text{x}10^{5}$	$1.88\text{x}10^{4}$
	β_T (K^{-1})	$1.5\text{x}10^{-4}$	$8\text{x}10^{-6}$
Boundary Conditions	h_R (W/m^2)	1000	50
	h_B (W/m^2)	500	25

Due to the computational expense of using so many input uncertainty distributions, only a level one analysis was used, corresponding to linear response functions with respect to each input. The resulting sensitivities for each attachment model are shown in Figure 7.2 where the height of the bars represent the mean elementary effect of the normalized Weibull deviation for the final Zn composition field with respect to a given input, and the error bars indicate the standard deviation of the elementary effects. Based on these results for all three attachment schemes, the sensitivity of the simulations to parameters that directly influence free-floating solid and grain attachment are comparable or much greater than to the material properties and boundary conditions. For subsequent analysis, in order to reduce the number of model evaluations for higher order response surfaces, the material properties and boundary

conditions will be assumed constant, and only the input uncertainties for the packing fraction, particle size, and dendrite arm spacing will be used.

7.4 Uncertainty Quantification of the Discrete Attachment Models

The first comparison of interest is between the two discrete grain attachment models. The purpose of the AVM scheme proposed by Vusanovic and Krane [58] was to include the effect of the local velocity field on the likelihood of free-floating grains attaching to the rigid solid interface. However, it is of interest to determine how much of a difference the inclusion of this effect actually has on the macrosegregation prediction. If the solutions are very different, then it must be determined which one more accurately reflects the physical system. If they are largely the same (for some set of input uncertainties), then one model might be selected over another for other considerations, such as numerical stability or computational expense.

By reducing the number of inputs to only those directly affecting the grain attachment model (packing fraction, particle size, and dendrite arm spacing), the uncertainty analysis was able to be increased to level three, significantly reducing the error in the fit of the response surface to the model data points collected from the sparse grid. The resulting probability distribution functions for the normalized Weibull deviation of the final Zn composition fields are shown in Figure 7.3. The two models have slightly different mean values (10.5×10^{-3} for the CPF model and 8.94×10^{-3} for the AVM) but mostly overlap. The Bhattacharyya coefficient for these two distributions is $BC = 0.871$.

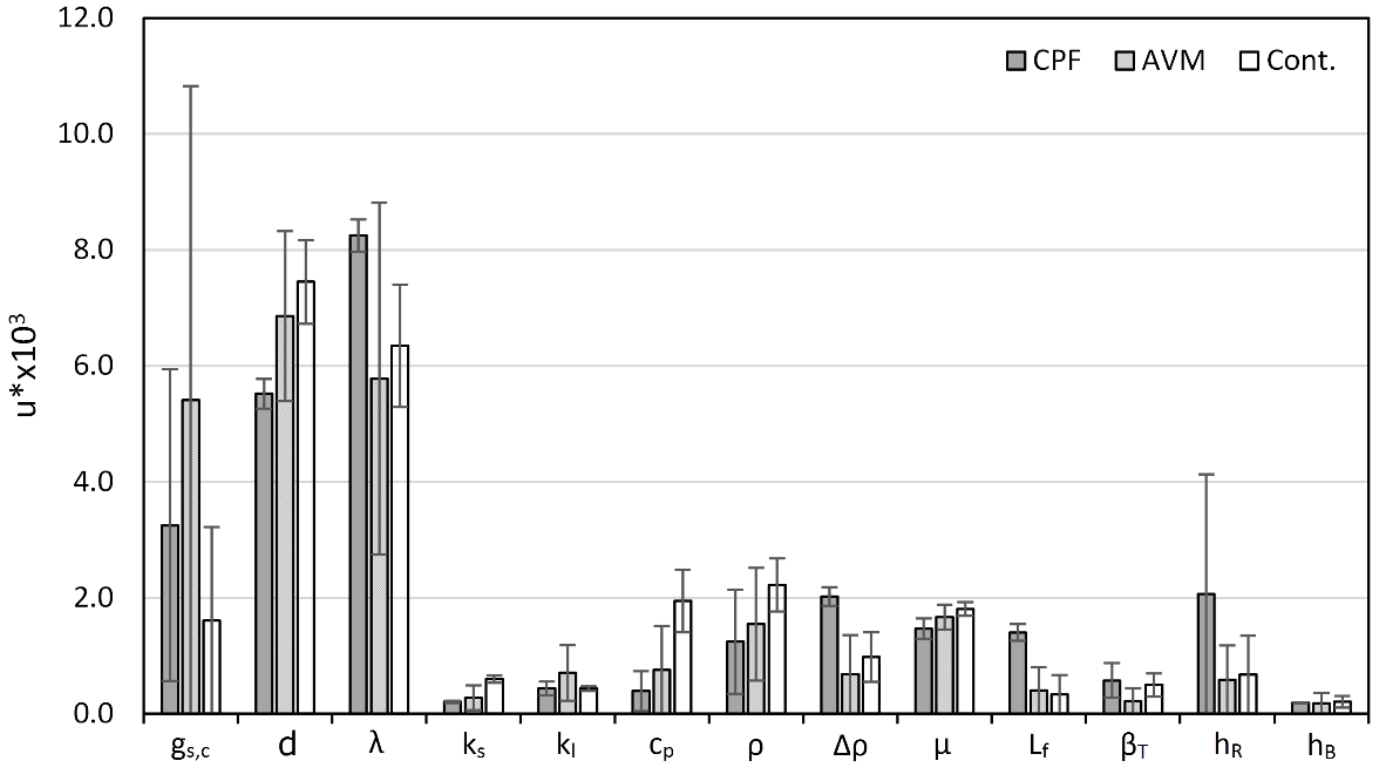

Figure 7.2: Sensitivities from the level 1 analysis of the three attachment schemes for the input distributions given in Table 7.1.

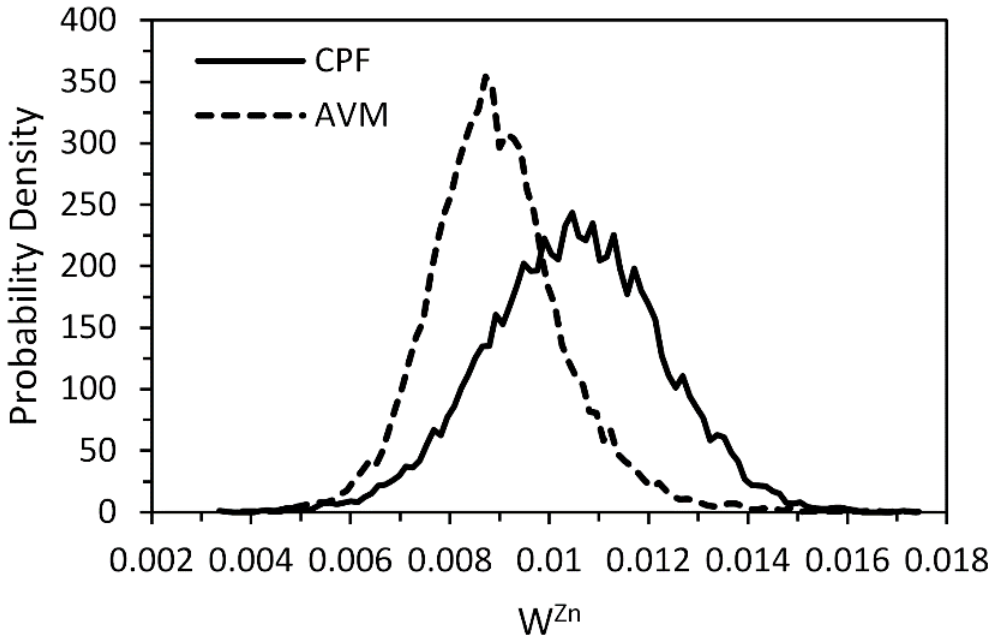

Figure 7.3: Level 3 analysis of the CPF and AVM models for input ranges in the attachment model parameters. The RMSE for the CPF model is 5.58% and for the AVM model is 5.13%.

Considering that these two attachment models yield mostly the same results for the given input uncertainties, an interesting question is with what level of certainty must these inputs be known in order for the differences in the attachment models to become significant? To address this question, the standard deviations of the input distributions were multiplied by factors less than one, and the overlap in the output distributions were monitored as the input uncertainties were decreased. The Bhattacharyya coefficient (measuring the amount of overlap between the distributions) as a function of the standard deviation multiplier is shown in Figure 7.4 along with examples of the output PDFs at selected points. As expected, when the input uncertainties are decreased, the overlap between the output PDFs also decreases. When the input standard deviations

reach one tenth of the values given in Table 7.1, there is no overlap between the output distributions. The consequence of this analysis is that, if the uncertainty in the outputs do not achieve some level of accuracy in which they do not significantly overlap, then they may be said to produce essentially the same results. In this case, selection of one model over the other can be based on concerns such as ease of implementation or numerical efficiency, rather than on physical accuracy. However, if this is not the case and the two models are significantly different, then one must be selected over another based on their physical relevance.

A more traditional manner of comparing the results of the two discrete attachment models is by comparing the means and standard deviations of the output distributions as a function of the input deviation multiplier (Figure 7.5). As the level of input uncertainty is reduced, the mean output values of the models (particularly the AVM scheme) change some, but more significantly, the standard deviations become much smaller as the input uncertainty is reduced. This manner of representing the data is a convenient way to compare to experiments that have their own set of error bars.

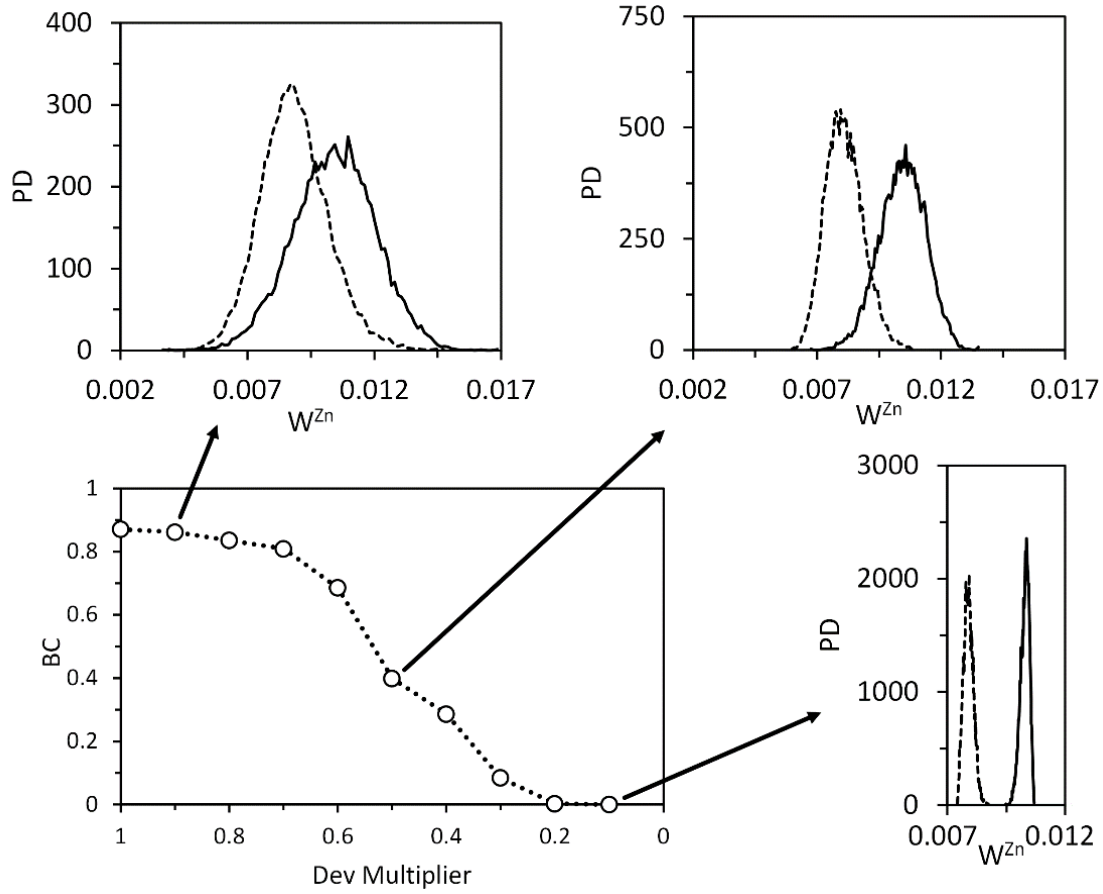

Figure 7.4: The Bhattacharyya coefficient comparing the CPF and AVM schemes as a function of the width of the input uncertainty distributions and insets showing the output probability distribution functions for the normalized Weibull deviation for the final Zn composition fields for three different input uncertainty levels.

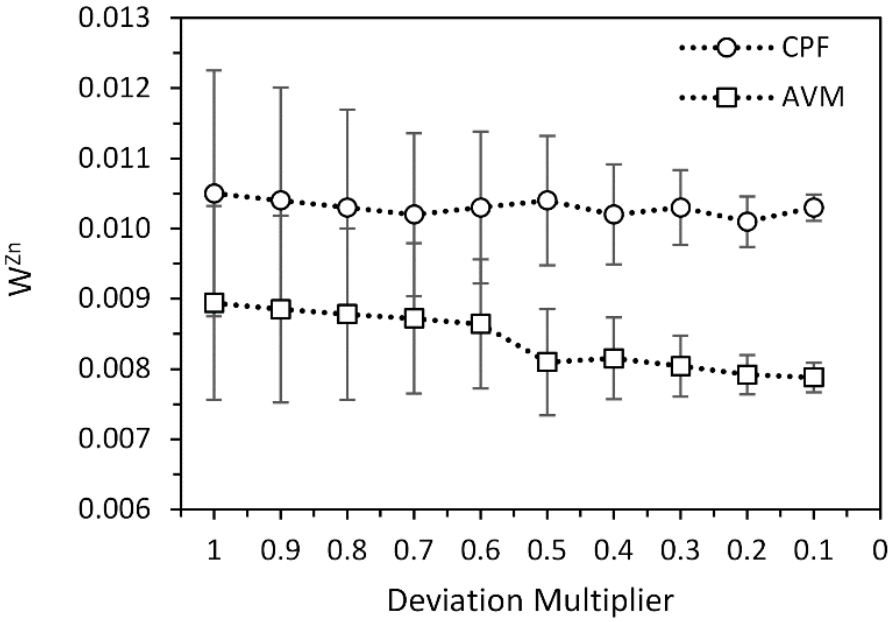

Figure 7.5: The mean and standard deviation of the normalized Weibull deviation for the CPF and AVM attachment models at various uncertainty levels.

There are essentially three different sources of the output uncertainty shown in Figure 7.3 through Figure 7.5. The first is the lack of knowledge of the appropriate values of the critical solid fraction, dendrite arm spacing, and particle size. This source of error is significant, but reducible through improved experimentation. Second, any experimentation used to determine these inputs contains irreducible error in the limitations of the measurement technique, generally referred to as aleatoric uncertainty.

The last type of error is related to the model limitations in that both the CPF and AVM schemes assume that the these inputs are constant and uniform over the domain. However, the critical fraction solid and dendrite arm spacing are related to the grain

morphology which is subsequently a function of the local cooling conditions, solute field, and details of the grain refiner additions. The particle size is a representative average, but in reality, the free-floating grains nucleate at some size and then grow over time, resulting in a time-varying distribution of sizes over the domain. If these spatial distributions are well known before hand, then it is a simple extension of the model to allow these inputs to vary over the domain. However, using new sub-models to predict these distributions represents a significant effort and will introduce new input parameters that must then be determined in some way. The effort required to add new physical phenomena to the model begs the question as to whether it will really improve the macrosegregation predictions. Thankfully, uncertainty quantification allows for this determination before expending the effort. Appropriate experiments will allow for the determination of the spatial variation among these parameters for a particular situation. Using these distributions as input uncertainties will yield some level of output uncertainty. If the level of output uncertainty is still too high, then this result is motivation to add new physics to the model. If the output uncertainty is within a tolerable limit, then the model may be used in its present condition.

7.5 Comparison of Continuum and Discrete Attachment Models

The other model comparison of interest is between the CPF and continuum attachment schemes. The primary question to be answered here how the continuum model changes the macrosegregation predictions relative to the related discrete model. (In this case, the best comparison is not with the AVM scheme because the continuum

model is not intended to account for the local velocity field.) The intention of the continuum attachment model is to reduce the occurrence of numerical artifacts that appear in the discrete models due to the effect of inaccurate geometric representations of the rigid solid interface on the local velocity field and solute advection. In doing so, however, the continuum model may have also significantly changed the overall macrosegregation prediction. If this is in fact the case, then experimental validation data is required to show that the continuum model is more physically accurate. However, if the results of the two models are largely similar, then the continuum model may be used freely in place of the CPF model and the benefits of limiting numerical artifacts gained.

Another concern, however, is that there is uncertainty in the model parameters that were introduced with the continuum scheme that do not apply to the discrete attachment models, namely the weighting exponent and packing range. Two interesting problems arise from this complication. The first is that, in the absence of robust experimental validation data (to which those parameters might be calibrated) it is of interest to determine what input values yield the closest predictions to the CPF model, allowing a fair comparison of the effects of the other various inputs. The second is determining the sensitivity of the model to these new input parameters. If the model is very sensitive to them, then their calibration to experimental results (or the development of a new packing scheme) becomes a priority. If, however, the model is not overly sensitive to these parameters, then less precise knowledge of their values is acceptable.

The first task is to determine the values of the weighting exponent and packing range that yield output distributions with the greatest similarity to the CPF model. This

goal can be accomplished by holding one of the inputs constant while the other is varied (though with zero input uncertainty) and then comparing the output distribution functions against the CPF model. First, the weighting exponent is varied while the weighting range is held constant ($\Delta g_s = 0.05$). An example of three resulting distributions is shown in Figure 7.6, compared against the CPF model. For small values of the weighting exponent, the permeability term in the momentum equations is introduced quickly once the fraction solid of a cell crosses the threshold into the weighting range. The effect of the permeability term is to damp the flow at the edge of the rigid mush, effectively reducing the relative motion of solid and liquid of differing compositions and reducing the overall macrosegregation. High values of the weighting exponent introduce the permeability term slowly, tending to allow more flow at the rigid interface and increasing the macrosegregation. These trends are reflected in the distributions shown in Figure 7.6 which causes higher Weibull deviations with larger exponent values, while generally remaining similar in shape and width. Interestingly, the effect of n is to translate the output probability distribution function for the normalized Weibull deviation without changing its width.

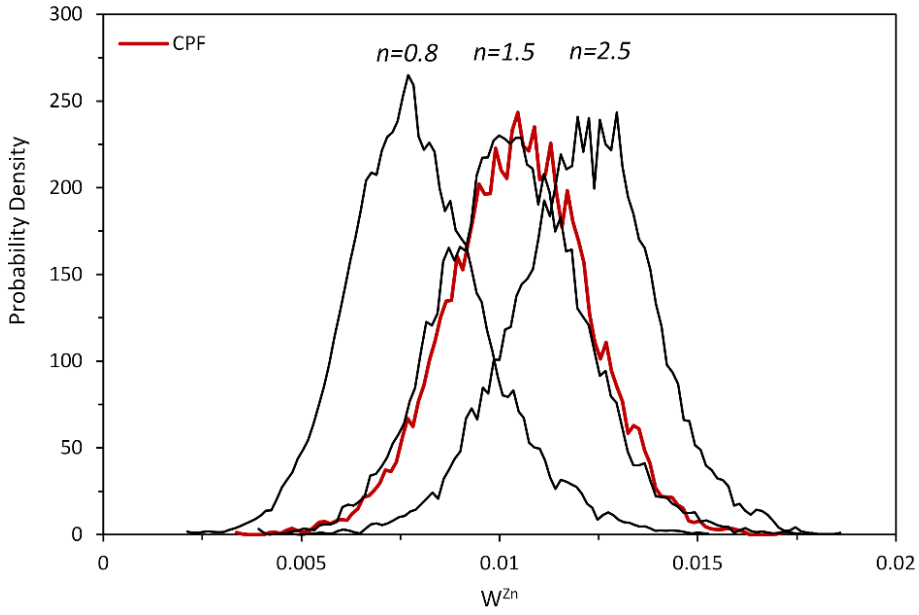

Figure 7.6: Examples of continuum model output distributions for the normalized Weibull deviation for Zn for three different weighting exponent values, compared to the output distribution for the CPF model.

The effect of the weighting exponent relative to the CPF model can also be determined by plotting the mean and standard deviation of the Weibull deviation distributions against that of the CPF model and by calculating the Bhattacharyya coefficient between the continuum Weibull deviation distributions and the output of the CPF model. The results of both approaches are shown in Figure 7.7. Again, as the weighting exponent is increased, the mean of the Weibull deviation increases as well, although the standard deviation of the distribution stays relatively constant regardless of the exponent value. Figure 7.7a shows that several weighting exponents, ranging from about 1.4 to 1.7, give close agreement with the CPF model. The calculation of the

Bhattacharyya coefficient (Figure 7.7b) agrees, and suggests that the best fit to the CPF model is for an exponent value of 1.5 ($BC = 0.995$).

Similarly, the weighting exponent was then held constant ($n = 1.5$) and the weighting range was varied. The comparisons of the resulting Weibull deviation distributions are shown in Figure 7.8. It is obvious from these results that changes in the weighting range have a much smaller effect on the overall macrosegregation distribution than the weighting exponent does. For all values of the weighting range that were tested, the Bhattacharyya coefficient is above 0.94 (Figure 7.8b). The best match with the CPF model is when $\Delta g_s = 0.05$.

Now that the mean values for the new inputs to the continuum attachment model that most closely resemble the CPF model have been determined, a better comparison of the two attachment schemes may now be made. Clearly, if these inputs are held constant, the output of the continuum model is essentially identical to the discrete model. However, if the continuum model is overly sensitive to these parameters, any uncertainty in their value has the potential to negate any benefit derived from its differences with the discrete models. To test this, the input uncertainties shown in Table 7.2 were implemented into the continuum model. While the resulting sensitivities to n and Δg_s (Figure 7.9) are not completely negligible, they are smaller than the sensitivities of the model to the input parameters that are shared with the discrete models. These results show that the continuum attachment model may be implemented in place of a discrete model in order to reduce numerical artifacts and improve convergence without fear of

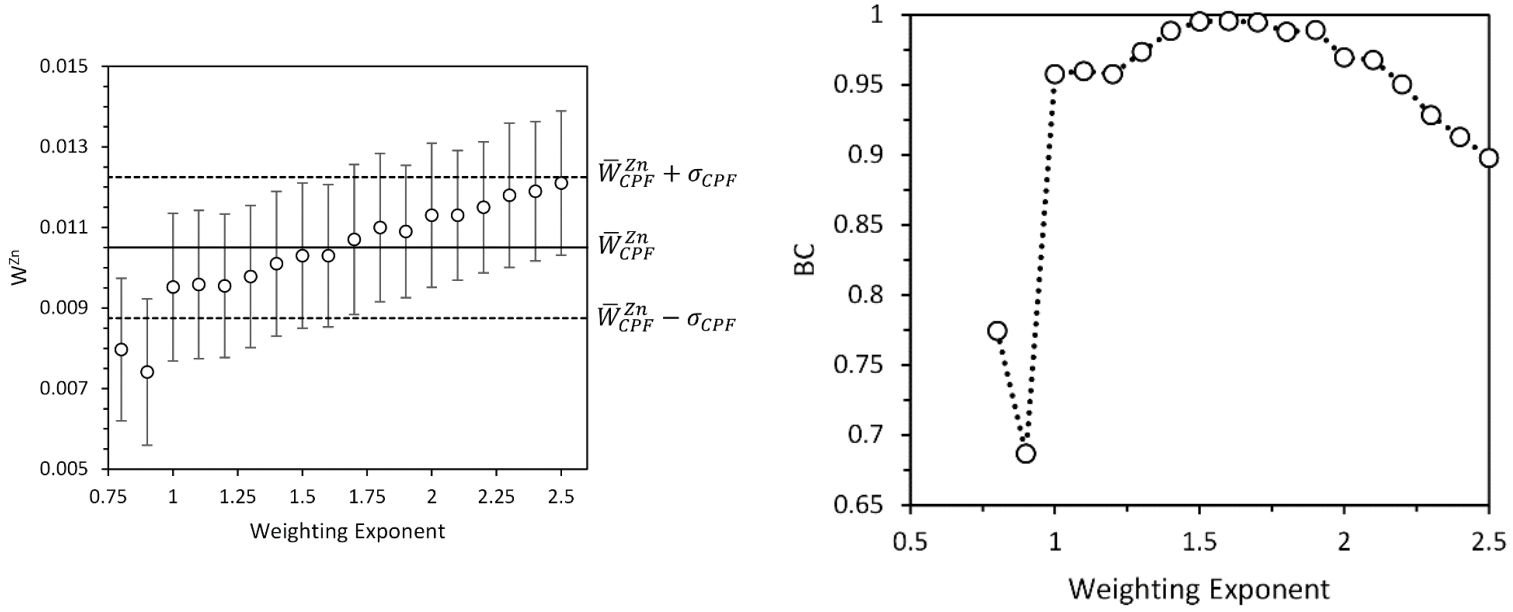

(a) *(b)*

Figure 7.7: Comparison of the output normalized Weibull deviation distributions for the continuum model for various values of the weighting exponent (n) and a constant weighting range ($\Delta g_s = 0.05$) to the CPF model. (a) Mean normalized Weibull deviations for the continuum model with error bars for the standard deviation against the mean CPF value (solid line) and plus and minus one standard deviation (dotted lines). (b) The Bhattacharyya coefficient between each output distribution from the continuum model to the CPF model.

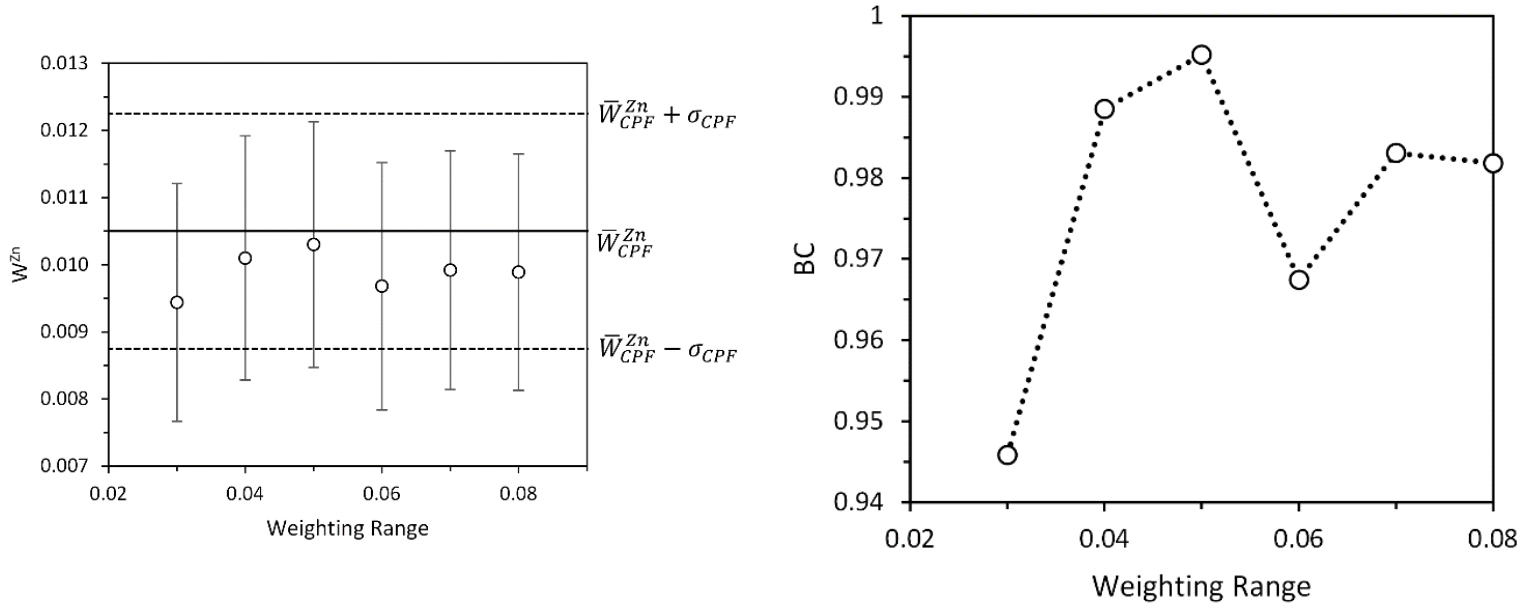

(a) *(b)*

Figure 7.8: Comparison of the output normalized Weibull deviation distributions for the continuum model for various values of the weighting range (Δg_s) and a constant weighting exponent ($n = 1.5$) to the CPF model. (a) Mean normalized Weibull deviations for the continuum model with error bars for the standard deviation against the mean CPF value (solid line) and plus and minus one deviation (dotted lines). (b) The Bhattacharyya coefficient between each output distribution from the continuum model to the CPF model.

significantly altering the model predictions as a function of the uncertainty in the values of the new parameters.

Table 7.2: Input uncertainties used to determine the sensitivity of the continuum attachment model to the new model parameters.

Parameter	Mean	Deviation
$g_{s,c}$	0.15	0.0375
d (μm)	30	5
λ (μm)	50	10
n	1.5	0.25
Δg_s	0.05	0.01

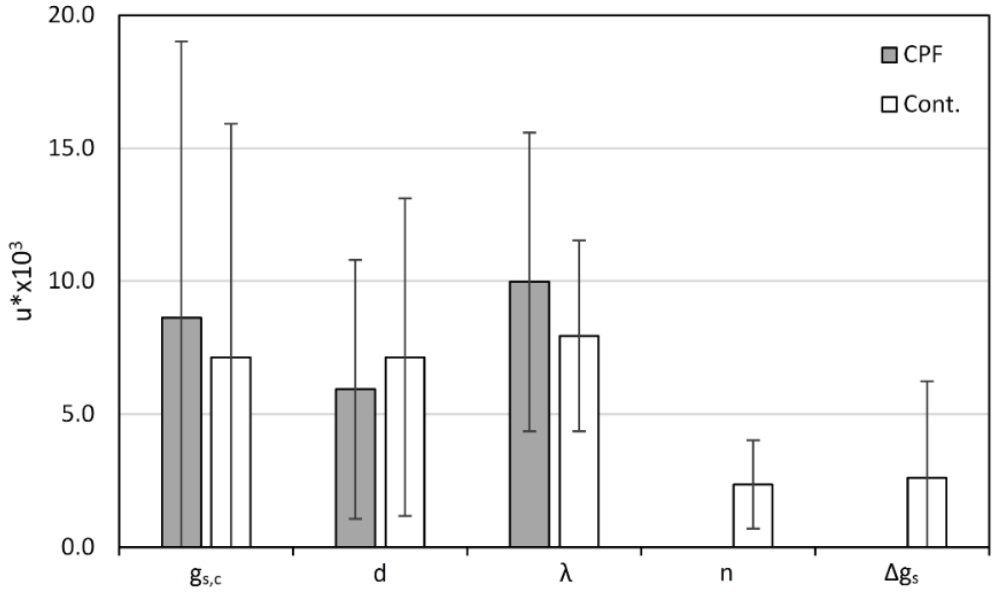

Figure 7.9: Comparison of the sensitivities of the normalized Weibull deviation for the final Zn composition field in the CPF and continuum grain attachment models.

7.6 Conclusions

This study used the PUQ framework, developed at Purdue University, to quantify the epistemic uncertainty in macrosegregation predictions produced by the use of three different grain attachment schemes in a model for equiaxed solidification. The three models, namely, the constant packing fraction (CPF), average velocity method (AVM) and the continuum method, were successfully compared for a base level of input uncertainties in those parameters that most directly affect the attachment of free-floating grains and the resulting macrosegregation (the critical fraction solid, free-floating particle size, and dendrite arm spacing). The macrosegregation was characterized using the deviation of a three-parameter Weibull distribution, normalized by the nominal composition, and the output of the uncertainty quantification was a distribution of these values. The Bhattacharyya coefficient was shown to be an effective metric for comparing the overlap between distributions obtained from different attachment schemes.

The first comparison was between the CPF and AVM models, intended to determine the significance of the velocity field on grain attachment. For the base level of input uncertainties used, there was no significant difference in the distribution of normalized Weibull deviations. However, if these input uncertainties were to be reduced via careful experimental measurements, then it was shown that the differences between the models may become significant. While this result is obvious, the implications are important. Figure 7.4 shows that for significantly different output distributions between the CPF and AVM attachment models, the input uncertainties need to be reduced by approximately 70% from the initial values set here. The input uncertainties include the assumptions that

the particle size and critical solid fraction are constant and uniform when in reality, this is not the case. It is possible that the required reduction in input uncertainty cannot be achieved without breaking down these assumptions and adding additional physical phenomena to the model.

The continuum model was then compared to the CPF model. First, the values of the parameters unique to the continuum model that produced the most similar results to the CPF model were determined by maximizing the Bhattacharyya coefficient between the relevant output distributions. Then, using these as the mean values, uncertainty in these parameters was added back into the system. It was found that the sensitivity to these parameters was less than the sensitivity of the model to the critical solid fraction, free-floating particle size, and the dendrite arm spacing. It was concluded that the continuum model produces similar results to the CPF model while reducing the effect of numerical artifacts. Considering that, given the level of certainty with which the input parameters for equiaxed solidification are known, the AVM, CPF, and continuum models produce mostly the same results, the continuum model is recommended for use in mixture formulations due to its suppression of numerical artifacts that arise from the discrete nature of the other grain attachment schemes.

CHAPTER 8. CONCLUSIONS AND RECOMMENDATIONS FOR FUTURE WORK

8.1 Conclusions

The purpose of this work was to investigate the modeling of flow interactions with the rigid mushy zone in the context of a mixture model for alloy solidification. A model was described that is capable of both columnar and equiaxed grain morphologies and was configured for the cylindrical static casting of aluminum alloy 7050 with heat transfer coefficient boundary conditions at the bottom and outer radius. First, the columnar case was examined. It was found that interactions between the bulk fluid flow and the edge of the mush have a dramatic impact on the prediction of freckle defects. Small rigid protrusions into the bulk natural convection flow cell have a significant and cumulative impact on the local flow field and subsequent solute transport. The coupling of the solute field to the local solid fraction, and therefore, the local permeability, generates a feedback loop that encourages the formation of channels. Unfortunately, the length scale of this effect within the simulations is necessarily constrained to the size of the numerical grid, even though the physical phenomena may happen on a scale as small as the dendrite arm spacing. The conclusion was that these macroscale simulations are not suited for freckle predictions, and instead, should seek to predict smooth composition fields and then be

coupled with an appropriate freckle criterion for defect predictions. To this end, recommendations were made for a numerical convergence criterion that tends to reduce the appearance of rigid protrusions, resulting in more appropriate macrosegregation predictions.

Next, the effect of the local velocity field on grain attachment was evaluated for equiaxed solidification. The average velocity method (AVM) was implemented based on previous work from the literature, and compared a new variant, the face velocity method (FVM), and the more common constant packing fraction (CPF) model. It was shown that the inclusion of the velocity field in the criteria for grain attachment had a significant impact on macrosegregation predictions. The effect of various process parameters on the predicted macrosegregation, including the critical solid fraction for packing, the dendrite arm spacing, and the free-floating particle size, were reported. In particular the tendency for the CPF model to predict channel segregates in the equiaxed macrosegregation pattern was noted. Both of the velocity based models also predicted the presence of channel segregates, although they were suppressed under some conditions in the AVM model. These segregates bore some resemblance to freckles found in columnar castings, but no experimental observations have suggested their formation in equiaxed cases. Further evaluation found that these channels form as a result of the discrete nature of these three packing models. The discrete models assume that a control volume contains only free-floating or only rigid solid without a smooth transition between the two states. When a cell packs, the damping effect of the mushy zone permeability on the momentum conservation equations causes significant changes in the local flow field and solute

advection. However, unlike the columnar case in which additional iterations can smooth out protrusions, the discrete grain attachment models force the geometry of the rigid interface to follow the control volume boundaries, a constraint that is independent of iterations through the numerical solution.

To address the problem of channel segregates in the equiaxed cases due to the discrete nature of the grain attachment models and inaccurate representation of the rigid interface geometry, a new continuum model was developed. This model allows for cells at the interface between the slurry and rigid solid regions to undergo a smooth transition between the two states. The model works by assuming that grain attachment occurs over a finite range of solid fractions and the relevant source terms in the momentum conservation equations are controlled using a weighting function. This approach allows for the grain attachment model to be iterated and under-relaxed in order to damp the formation and propagation of rigid protrusions. The continuum model was found to effectively suppress the formation of channel segregates, and the effect of the new model parameters (the packing range and weighting function exponent) on the macrosegregation development were described.

Finally, three of the grain attachment models (the CPF, AVM, and continuum model) were compared to one another in the context of uncertainty in various input parameters using the PRISM Uncertainty Quantification (PUQ) framework. The purpose of this analysis was to determine if changes in the grain attachment models had a significant impact on macrosegregation predictions given that many of the input parameters are not known with complete certainty. First, a large number of inputs were given Gaussian input

probability distributions. These included material properties, boundary conditions, and inputs to the permeability and packing models. The PUQ framework circumvents the computational expense of the solidification model by running only a small number of simulations at a select number of points determined by the Smolyak sparse grid algorithm. A polynomial response surface is then fitted to the resulting data. Monte Carlo sampling is then performed on the comparatively inexpensive response surface to construct output probability distribution functions. The macrosegregation in these cases was quantified using the deviation of a three-parameter Weibull distribution fit to the final Zn composition field, normalized by the nominal composition. An initial analysis found that the macrosegregation field for three grain attachment models is most sensitive to the dendrite arm spacing, free-floating particle size, and the critical solid fraction for dendrite coherency. A comparison between the CPF and AVM models showed little difference in the predicted normalized Weibull deviation for the given input uncertainties. It was found that the input distribution must be narrowed to approximate 10% of their estimated values before the models predicted significantly different results. This data suggests that the inclusion of the velocity field in the grain attachment criterion does not have a significant effect on predicted macrosegregation development in the context of the uncertainty inputs. For the differences in the models to become relevant, future work should be focused on experimental data that improves the knowledge of the input parameters, or model improvements that reduce the output uncertainty. The next comparison was between the CPF and continuum models. Uncertainty quantification was used to calibrate the new model parameters in the continuum scheme (the packing range

and weighting exponent) by maximizing the similarity between the output distributions of the two attachment schemes for the same set of input uncertainty. After calibration, the two models exhibited practically identical output probability distributions for the normalized Weibull deviation. In this case, because both attachment schemes were designed to model the same physical phenomena (i.e. they assume that the critical solid fraction is constant and uniform, and do not include the effect of the local velocity field) the similarity in the output distribution was not surprising. The importance in this results is that because the overall macrosegregation prediction does not change significantly between the two schemes, then the continuum model is preferred due to its suppression of numerical artifacts. Finally, the sensitivity of the continuum model to the packing range and weighting function exponent was evaluated, and found to be smaller than that of the critical solid fraction, the dendrite arm spacing, and the free-floating particle size, though not completely negligible. In general, these collective results show that the continuum grain attachment model is a significant improvement over the previous discrete attachment models for approximating the interactions between the bulk fluid flow and the rigid mushy zone in simulations of equiaxed solidification using a mixture formulation of the governing conservation equations.

8.2 Future Work

While the work presented here has improved the modeling of interactions between the bulk fluid flow and the rigid mush in mixture solidification simulations, there are many areas where additional work must be done to improve the understanding of the physical

phenomena and to improve the predictive ability of solidification models and macrosegregation predictions.

8.2.1 Evaluation and Development of Freckle Criteria

CHAPTER 3 showed that freckle predictions in macroscale solidification simulations are unreliable due to instabilities that necessarily form on the length scale of the numerical grid. However, these artificial channels may be suppressed by application of appropriate convergence criteria. Going forward with improving the prediction of freckles for various metallurgical processes, the primary challenge is bridging the multiple length scales involved in freckle formation and propagation. At the lowest length scale, instabilities that are responsible for channel formation may be as small as the dendrite arm spacing. But the fluid flow, solute transport, and heat transfer that affect small-scale channel development are all a function of the macroscale process parameters. It is clear that if an adequate freckle criterion is to be developed, the fundamental phenomena at these various length scales must be collectively understood.

A significant shortcoming of many existing freckle criteria is that they are limited to vertical or near vertical solidification directions. When the solidification front is far from horizontal, channel development is complicated by the additional fluid flow parallel to the interface. A significant advance in understanding freckle formation would be to investigate the case of a cavity cooled from a sidewall by using both macro- and microscale simulation tools, and preferably for a specific situation for which experimental data may be either easily obtained or already available in the literature. Macroscale

simulations, such as those presented in this work, may be used to predict the temperature gradients and local fluid flow conditions throughout the process. These conditions may then be compared to the experiments to determine where freckles are most likely to occur. Microscale simulations (e.g. cellular automata or phase field) can then be applied using local conditions determined by the macroscale models to areas with and without freckles (Figure 8.1). If these models accurately predict the formation or absence of channels, then they may be used to gain a deeper understanding of the physical phenomena responsible for freckle growth, and perhaps, will suggest an avenue for development of a general freckle criterion or improvements to existing criteria. Of course there are examples of microscale models used for freckle predictions [17,18], but these studies have been limited to directional solidification and have not been applied to arbitrary solidification front angles or in the presence of bulk flow fields that develop by thermosolutal natural convection during casting processes.

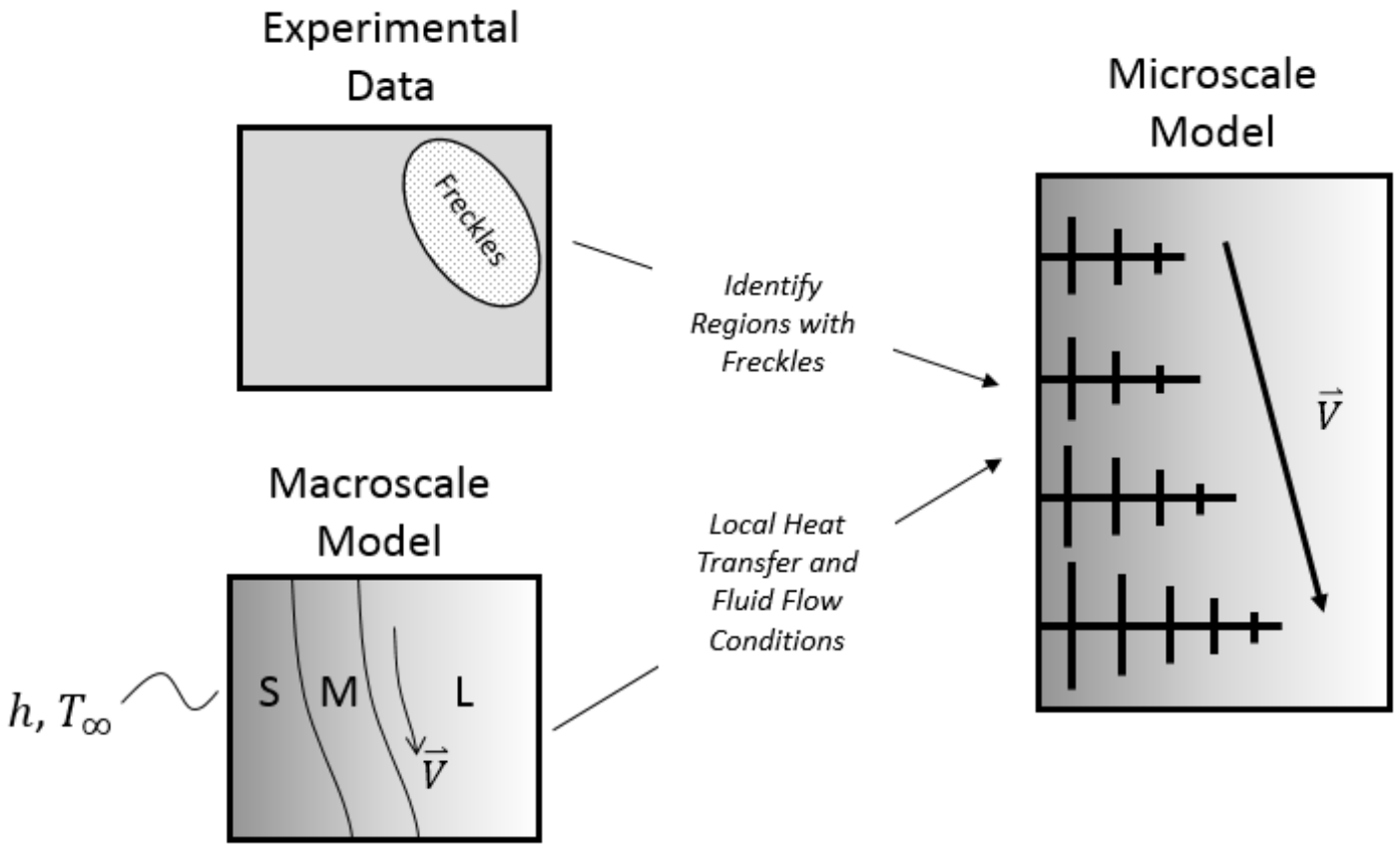

Figure 8.1: Schematic of a multi-scale approach to understanding freckle formation.

8.2.2 Determining the Packed Fraction and Interface Geometry

For equiaxed solidification simulations using the mixture formulation of the governing conservation equations, the continuum grain attachment model represents a significant improvement over the existing discrete attachment schemes. However, while its implementation in this work demonstrated its ability to suppress numerical artifacts, its development relied on a variety of simplifying assumptions and approximations. The first of these is the crude scheme used to determine the packed fraction of a cell (Equation (2.19)), which assumes that grain attachment occurs linearly over a finite range of solid fractions. However, the interface between the slurry and rigid solid regions is sharp on a length scale smaller than the control volume size, as shown in Section 6.2. The present model simply spreads grain attachment out over an arbitrary range of solid fractions, which is simple to implement and convenient from a numerical standpoint, but is not physically accurate.

One better method would be to use some interpolation scheme to determine the location of the iso-solid fraction line equal to the critical solid fraction in each cell. The amount of that cell containing free-floating vs. rigid solid can then be calculated based on the assumed packing fraction for the system. This approach has two major advantages. The first is that it is a more accurate depiction of the dendrite coherency point for the system in that it does not smear the grain attachment transition over a range of solid fractions. It instead determines the location of the interface between the two regions and perform the appropriate volume averaging for each cell. The second advantage is that it more accurately represents the geometry of the interface. As discussed previously, a

primary deficiency in the discrete models is that by forcing control volumes to contain either only free-floating solid particles or only rigid solid, the shape of the interface is misrepresented by being forced to fall on control volume faces. The continuum model as formulated in CHAPTER 2 is an improvement in that it allows a more flexible depiction of the interface shape, but the packing range is an artificial construction. A more accurate interpolation from the solid fraction field would be a further improvement on representing the interface geometry. Similarly, the power law form of the weighting function presented here is simply a convenient approach to adjusting the behavior of the transition region between free-floating and rigid solid, but more physically accurate forms may be developed in the future based on the fundamentals of solidification and multi-phase flows. Further development of methods for determining the packed fraction and form of the weighting function should ideally improve the representation of the physical system (perhaps including the effect of the local velocity field for example), and should be simple to implement using the formulation of the governing equations for momentum conservation developed here.

Another possible improvement for the continuum attachment model is adding in a rigorous interface reconstruction algorithm, similar to those used for fluid-fluid interfaces in multiphase flow simulations [85]. A schematic of such a reconstruction is shown in Figure 8.2. This approach would be a further improvement on the accuracy with which the interface geometry is represented. More importantly, implementing a reconstruction scheme could be used to improve the free-floating solid model. Currently, solid advection across a control volume face is calculated based on an interpolated value

of the packed fraction, P, between two main control volumes. This approach treats solid advection as an average of the packing in two neighboring control volumes regardless of the orientation of the interface. With the information from the reconstruction, the geometry of interface can be approximated on a sub-control volume length scale, allowing for a more exact determination of the fraction of each control volume face over which solid may be advected. Essentially, the packed fraction at the faces of a control volume is calculated based on the reconstruction rather than a simple interpolation. For example, consider a cell on the reconstructed interface as shown in Figure 8.3. The cell itself has a packed fraction, P, of approximately 0.5. In the present scheme, this means if this cell neighbors a fully packed cell (the south face in Figure 8.3), then the interpolated value of P used to determine the solid velocity in Stokes' law at this face would be $P_s = 0.75$, where the subscript denotes the south face of the control volume. However, based on the reconstruction, it is clear that this interface is completely packed and no solid motion should be possible (i.e. $P_s = 1$). A similar problem is encountered at the north face. If the neighboring cell to the north has no rigid solid, then the interpolated value of the packed fraction would be $P_n = 0.25$. However, it is clear from the location of the interface that there is no rigid solid at this face. The reconstruction approach allows for the correct determination of $P_n = 0$. At the east and west faces, the location at which the reconstructed interface intersects the faces may be readily calculated and the cell face packed fractions evaluated accordingly.

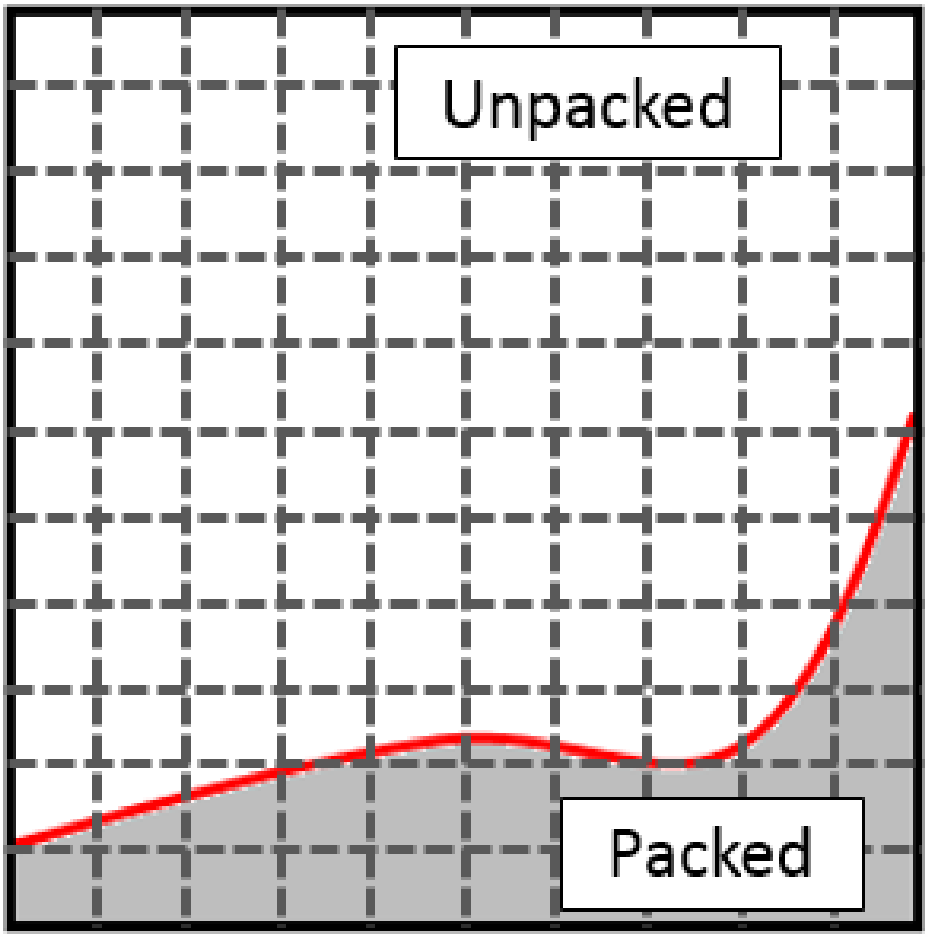

Figure 8.2: A schematic of the geometry of the reconstructed interface between the slurry and rigid solid regions of the domain.

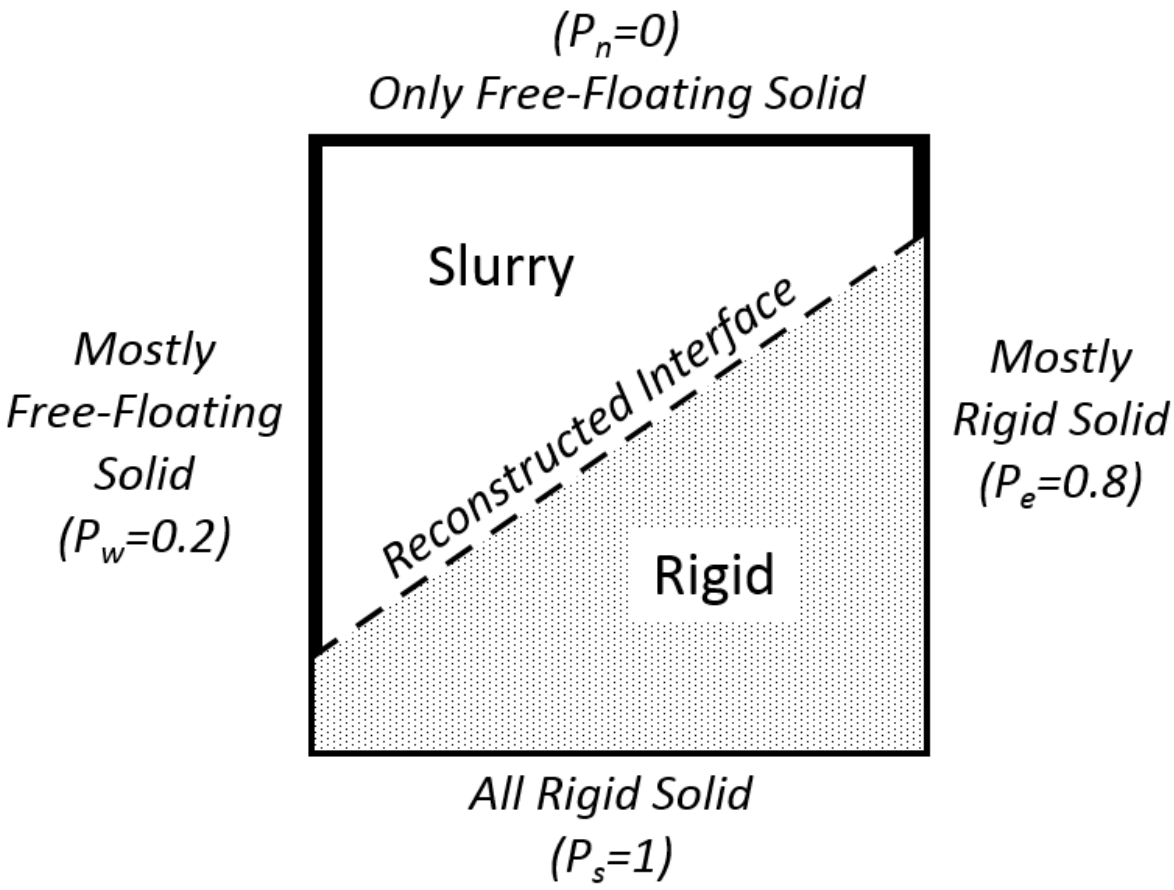

Figure 8.3: Schematic showing an example control volume lying on the reconstructed interface. The bolded portions of the faces indicate boundaries with neighboring control volumes that allow the motion of solid particles.

Another advantage of more accurate knowledge of the interface geometry is that it allows a better determination of the local viscosity of the solid pseudo-fluid. The model presented in this work used Vreeman's [71] recommendation for an average solid viscosity. The primary purpose for this is to avoid numerical instabilities caused by the fact that the viscosity function approaches infinity at the prescribed packing fraction. Vreeman's argument is based on the sharpness of the interface in that only a very small region of free-floating solid with a solid fraction near the dendrite coherency point is strongly affected by the increasing solid viscosity. With the introduction of the continuum model and the interface reconstruction, this approximation may no longer be necessary. Instead, the solid fraction of only the unpacked portion of the cell may be calculated based on the interface geometry and local gradients in the solid fraction field. The local solid viscosity may then be calculated based on the average solid fraction of just this portion of the cell containing free-floating solid. The relevant source terms that the solid viscosity affects in the momentum equations are then only included based on the packed fraction of the cell and the weighting function.

8.2.3 Local Grain Morphology

Dendrite coherency is a function of a variety of variables, most of which affect the solid fraction at which grains coalesce because they affect the grain morphology. In prescribing a particular critical solid fraction that is constant and uniform throughout the domain, all of the grain attachment models discussed in this work assume that the grain morphology is constant and uniform. Of course, the composition, cooling rate, and grain

refiner additions vary throughout the domain due to heat and mass transport phenomena, and potentially have a significant effect on the distribution of grain morphologies, and therefore, packing fractions. Wang and Beckermann [48] proposed a set of morphological relationships for this purpose, but in the context of the multi-phase model formulation for the conservation equations for solidification. If possible, these relationships should be adapted for the mixture formulation or a new set of relationships developed for this purpose.

8.2.4 Uncertainty Quantification and Experimental Validation

As discussed in CHAPTER 7, as new model developments are implemented, their impact on the overall solution should be evaluated using uncertainty quantification and compared to both previous versions of the model and experimental data. Such evaluation is necessary for a variety of reasons. The first is as a guard against adding computationally expensive model features that do not significantly change the solution. There is a constant temptation to continue adding ever more complexity that, it is often assumed, better represents the physical system. However, such changes must constantly be weighed against any additional computational expense. A simple model addition that greatly improves the predictive ability of the simulation without sacrifices to computation time is of course welcome, but these types of modifications must be differentiated from those that greatly affect the model expense without significantly changing the solution. This problem is also closely tied to the risk of adding additional uncertainty to the model by

adding new uncertain parameters. Such effects should be monitored during model development and supplemented with experimental measurements when necessary.

Specifically for uncertainty in macrosegregation predictions, there is need for further improvements to the quantification of macrosegregation. It was noted during this study that the normalized Weibull deviation, while certainty an improvement over the more commonly used macrosegregation number, tends to produce a noisy data set when a wide range of input parameters is used, an issue that reduces the accuracy of a fitted response surface and may, in the future, make comparisons with experimental data difficult. This problem may be due to the presence of numerical artifacts, such as channel segregates, that distort the composition field and tend to have a significant effect on the normalized Weibull deviation. Further improvements to the continuum model may be able to resolve this problem, but modification of the method for fitting the three-parameter Weibull distribution or development of another, more stable metric may be necessary.

Another glaring need in this research area, and an opportunity for use of uncertainty quantification, is quality experimental data for model validation. Some macrosegregation data exist for direct-chill casting, but considering the significant complexity and uncertainty in the boundary conditions for that process, for the purpose of basic grain attachment model validation, a more simplistic static casting case would be preferred. Good data would include a variety of information. Composition measurements that describe the macrosegregation would be the primary output. Other measurements are necessary to determine model inputs. The static casting should be outfitted with an

array of thermocouples in order to provide cooling condition data for validation, but also to determine local packing fractions using the thermal method employed by some researchers [41,42]. Any packing fraction measurements should be supported by microscopy to determine the local grain morphologies. Further thermal measurements should be used to determine boundary conditions [86]. Ideally, the process will be performed several times in order to quantify the uncertainty in the outputs of interest for a fair comparison to the model outputs, which of course, should be generated using uncertainty quantification techniques.

REFERENCES

REFERENCES

[1] J.A. Dantzig, M. Rappaz, Solidification, CRC Press, Boca Raton, Fl., 2009.

[2] P. Auburtin, T. Wang, S.L. Cockcroft, A. Mitchell, Freckle formation and freckle criterion in superalloy castings, Metall. Mater. Trans. B. 31 (2000) 801–811. doi:10.1007/s11663-000-0117-9.

[3] C. Beckermann, J.P. Gu, W.J. Boettinger, Development of a Freckle Predictor via Rayleigh Number Method for Single-Crystal Nickel-Base Superalloy Castings, Metall. Mater. Trans. A. 31 (2000) 2545–2557. doi:10.1007/s11661-000-0199-7.

[4] J.A. Van Den Avyle, J.A. Brooks, A.C. Powell, Reducing Defects in Remelting Processes for High-Performance Alloys, JOM. (1998) 22–25. doi:10.1007/s11837-998-0374-7.

[5] K. Suzuki, T. Miyamoto, Study on the Formation of “A” Segregation in Steel Ingot, Trans. Iron Steel Inst. Japan. 18 (1978) 80–89.

[6] T. Sawada, S. Suzuki, K. Kajikawa, A numerical analysis of inverted V-segregation and its dependency on alloy properties, in: A. Kharicha, R.M. Ward, H. Holzgruber, M. Wu (Eds.), Int. Symp. Liq. Met. Process. Cast., Leoben, Austria, 2015: pp. 426–430.

[7] R. Mehrabian, M.A. Keane, M.C. Flemings, Experiments on macrosegregation and freckle formation, Metall. Trans. 1 (1970) 3238–3241. doi:10.1007/BF03038445.

[8] N. Mori, K. Ogi, Study on formation of channel-type segregation, Metall. Trans. A. 22 (1991) 1663–1672. doi:10.1007/BF02667378.

[9] M.R. Bridge, M.P. Stephenson, J. Beech, Direct observations on channel segregate formation in aluminium alloys, Met. Technol. 9 (1982) 429–433. doi:10.1179/030716982803286025.

[10] S.M. Copley, A.F. Giamei, S.M. Johnson, M.F. Hornbecker, The Origin of Freckles in Unidirectionally Solidified Castings, Metall. Trans. 1 (1970) 2193–2204. doi:10.1007/BF02643435.

[11] C.S. Magirl, F.P. Incropera, Flow and Morphological Conditions Associated With Unidirectional Solidification of Aqueous Ammonium Chloride, J. Heat Transfer. 115 (1993) 1036–1043. doi:10.1115/1.2911358.

[12] A. Hellawell, J.R. Sarazin, R.S. Steube, Channel convection in partly solidified systems, Philos. Trans. Phys. Sci. Eng. 345 (1993) 507–544. doi:10.1098/rsta.1993.0143.

[13] M.G. Worster, Convection in Mushy Layers, Annu. Rev. Fluid Mech. 29 (1997) 91–122. doi:10.1146/annurev.fluid.29.1.91.

[14] M.T. Rad, P. Kotas, C. Beckermann, Rayleigh number criterion for formation of A-segregates in steel castings and ingots, Metall. Mater. Trans. A Phys. Metall. Mater. Sci. 44 (2013) 4266–4281. doi:10.1007/s11661-013-1761-4.

[15] P. Auburtin, S.L. Cockcroft, A. Mitchell, A.J. Schmalz, Center Segregation, Freckles and Development Directions for Niobium-Containing Superalloys, in: Superalloys 718, 625, 706 Var. Deriv., TMS, 1997: pp. 47–54. doi:10.7449/1997/Superalloys_1997_47_54.

[16] A. Bejan, Convection Heat Transfer, 2nd ed., John Wiley & Sons, Inc., New York, 1995.

[17] L. Yuan, P.D. Lee, G. Djambazov, K. Pericleous, Multiscale Modeling of the Onset of Freckle Formation During Vacuum Arc Remelting, in: Int. Symp. Liq. Met. Process. Cast., 2009: pp. 39–46.

[18] L. Yuan, P.D. Lee, A new mechanism for freckle initiation based on microstructural level simulation, Acta Mater. 60 (2012) 4917–4926. doi:10.1016/j.actamat.2012.04.043.

[19] W.D. Bennon, F.P. Incropera, A continuum model for momentum, heat and species transport in binary solid-liquid phase change systems- II . Application to solidification in a rectangular cavity, Int. J. Heat Mass Transf. 30 (1987) 2171–2187. doi:10.1016/0017-9310(87)90095-0.

[20] W.D. Bennon, F.P. Incropera, A continuum model for momentum, heat and species transport in binary solid-liquid phase change systems- I . Model formulation, Int. J. Heat Mass Transf. 30 (1987) 2161–2170. doi:10.1016/0017-9310(87)90094-9.

[21] C. Frueh, D.R. Poirier, S.D. Felicelli, Effect of computational domain size on the mathematical modeling of transport processes and segregation during directional solidification, Metall. Mater. Trans. A. 31 (2000) 3129–3135. doi:10.1007/s11661-000-0092-4.

[22] P.K. Sung, D.R. Poirier, S.D. Felicelli, Sensitivity of mesh spacing on simulating macrosegregation during directional solidification of a superalloy, Int. J. Numer. Methods Fluids. 35 (2001) 357–370. doi:10.1002/1097-0363(20010215)35:3<357::AID-FLD99>3.0.CO;2-9.

[23] P.K. Sung, D.R. Poirier, S.D. Felicelli, Simulating the Initiation of a Channel during Directional Solidification of a Superalloy, Metall. Mater. Trans. A. 32A (2001) 202–207. doi:10.1073/pnas.0703993104.

[24] J. Guo, C. Beckermann, Three-Dimensional Simulation of Freckle Formation During Binary Alloy Solidification: Effect of Mesh Spacing, Numer. Heat Transf. Part A. (2003) 559–576. doi:10.1080/10407780390224184.

[25] J. Jain, A. Kumar, P. Dutta, Numerical Studies on Channel Formation and Growth During Solidification: Effect of Process Parameters, J. Heat Transfer. 129 (2007) 548. doi:10.1115/1.2709660.

[26] H. Combeau, M. Bellet, Y. Fautrelle, D. Gobin, E. Arquis, O. Budenkova, *et al.*, Analysis of a numerical benchmark for columnar solidification of binary alloys, IOP Conf. Ser. Mater. Sci. Eng. 33 (2012) 1–13. doi:10.1088/1757-899X/33/1/012086.

[27] A. Kumar, B. Dussoubs, M. Zaloznik, H. Combeau, Influence of Discretization of Permeability Term and Mesh Size on the Prediction of Channel Segregations, IOP Conf. Ser. Mater. Sci. Eng. 27 (2012) 1–8. doi:10.1088/1757-899X/27/1/012039.

[28] I. Vušanović, V.R. Voller, Understanding Channel Segregates in Numerical Models of Alloy Solidification: A Case of Converge First and Ask Questions Later, Mater. Sci. Forum. 790-791 (2014) 73–78. doi:10.4028/www.scientific.net/MSF.790-791.73.

[29] J. Li, M. Wu, A. Ludwig, A. Kharicha, Simulation of macrosegregation in a 2.45-ton steel ingot using a three-phase mixed columnar-equiaxed model, Int. J. Heat Mass Transf. 72 (2014) 668–679. doi:10.1016/j.ijheatmasstransfer.2013.08.079.

[30] V.R. Voller, A. Mouchmov, M. Cross, An explicit scheme for coupling temperature and concentration fields in solidification models, Appl. Math. Model. 28 (2004) 79–94. doi:10.1016/S0307-904X(03)00115-X.

[31] R. Pardeshi, V.R. Voller, A.K. Singh, P. Dutta, An explicit–implicit time stepping scheme for solidification models, Int. J. Heat Mass Transf. 51 (2008) 3399–3409. doi:10.1016/j.ijheatmasstransfer.2007.11.060.

[32] J.F. Grandfield, D.G. Eskin, I.F. Bainbridge, *Direct-Chill Casting of Light Alloys*, John Wiley & Sons, Inc., Hoboken, New Jersey, 2013.

[33] D.H. StJohn, M. Qian, M.A. Easton, P. Cao, Z. Hildebrand, Grain Refinement of Magnesium Alloys, Metall. Mater. Trans. A. 36 (2005) 1669–1679.

[34] J. Ni, C. Beckermann, A volume-averaged two-phase model for transport phenomena during solidification, Metall. Trans. B. 22 (1991) 349–361. doi:10.1007/BF02651234.

[35] A. V. Reddy, C. Beckermann, Simulation of the effect of thermosolutal convection, shrinkage induced flow, and solid transport on macrosegregation and equiaxed grain size distribution in a DC continuous cast Al-Cu round ingot, in: V.R. Voller, S.P. Marsh, N. El-Kaddah (Eds.), Mater. Process. Comput. Age II, 1995: pp. 89–102.

[36] G.D. Scott, D.M. Kilgour, The density of random close packing of spheres, J. Phys. D. Appl. Phys. 2 (2002) 863–866. doi:10.1088/0022-3727/2/6/311.

[37] D.B. Spencer, R. Mehrabian, M.C. Flemings, Rheological behavior of Sn-15 pct Pb in the crystallization range, Metall. Trans. 3 (1972) 1925–1932. doi:10.1007/BF02642580.

[38] A.K. Dahle, D.H. StJohn, Rheological Behaviour of the Mushy Zone and its Effect on the Formation of Casting Defects During Solidification, Acta Mater. 47 (1999) 31–41. doi:10.1016/S1359-6454(98)00342-5.

[39] S.A. Metz, M.C. Flemings, A Fundamental Study of Hot Tearing, AFS Trans. 78 (1970) 453–460.

[40] R.J. Claxton, Aluminum alloy coherency, JOM. 27 (1975) 14–16.

[41] L. Arnberg, G. Chai, L. Backerud, Determination of dendritic coherency in solidifying melts by rheological measurements, Mater. Sci. Eng. A. 173 (1993) 101–103.

[42] M. Malekan, S.G. Shabestari, Effect of grain refinement on the dendrite coherency point during solidification of the A319 aluminum alloy, Metall. Mater. Trans. A 40 (2009) 3196–3203. doi:10.1007/s11661-009-9978-y.

[43] G. Chai, L. Backerud, T. Rolland, L. Arnberg, Dendrite coherency during equiaxed solidification in binary aluminum alloys, Metall. Mater. Trans. A. 26 (1995) 965–970. doi:10.1007/BF02649093.

[44] A.K. Dahle, L. Arnberg, The rheological properties of solidifying aluminum foundry alloys, JOM. 48 (1996) 34–37. doi:10.1007/BF03222888.

[45] A.K. Dahle, L. Arnberg, On the assumption of an additive effect of solute elements in dendrite growth, Mater. Sci. Eng. A. 225 (1997) 38–46. doi:10.1016/S0921-5093(96)10873-X.

[46] C.Y. Wang, C. Beckermann, Equiaxed dendritic solidification with convection: Part I. Multiscale/multiphase modeling, Metall. Mater. Trans. A. 27 (1996) 2754–2764. doi:10.1007/BF02652369.

[47] C.Y. Wang, C. Beckermann, Equiaxed Dendritic Solidification with Convection: Part II. Numerical Simulations for an Al-4 Wt Pct Cu Alloy, Metall. Mater. Trans. A. 27 (1996) 2765–2783. doi:10.1007/BF02652370.

[48] C.Y. Wang, C. Beckermann, A Multiphase Solute Diffusion Model for Dendritic Alloy Solidification, Metall. Trans. A. 24 (1993) 2787–2802. doi:10.1007/BF02659502.

[49] C.Y. Wang, S. Ahuja, C. Beckermann, H.C.D.G. Iii, D. Groh, Multiparticle Interfacial Drag in Equiaxed Solidification, Metall. Mater. Trans. B. 26 (1995) 111–119. doi:10.1007/BF02648984.

[50] A. Ludwig, M. Wu, Modeling of globular equiaxed solidification with a two-phase approach, Metall. Mater. Trans. A. 33 (2002) 3673–3683. doi:10.1007/s11661-002-0241-z.

[51] M. Zaloznik, H. Combeau, An operator splitting scheme for coupling macroscopic transport and grain growth in a two-phase multiscale solidification model: Part I - Model and solution scheme, Comput. Mater. Sci. 48 (2010) 1–10. doi:10.1016/j.commatsci.2009.04.036.

[52] M. Wu, A. Fjeld, A. Ludwig, Modelling mixed columnar-equiaxed solidification with melt convection and grain sedimentation – Part I: Model description, Comput. Mater. Sci. 50 (2010) 32–42. doi:10.1016/j.commatsci.2010.07.005.

[53] M. Wu, A. Ludwig, A. Fjeld, Modelling mixed columnar-equiaxed solidification with melt convection and grain sedimentation – Part II: Illustrative modelling results and parameter studies, Comput. Mater. Sci. 50 (2010) 43–58. doi:10.1016/j.commatsci.2010.07.006.

[54] J. Ni, F.P. Incropera, Extension of the continuum model for transport phenomena occurring during metal alloy solidification—I. The conservation equations, Int. J. Heat Mass Transf. 38 (1995) 1271–1284. doi:10.1016/0017-9310(94)00236-O.

[55] J. Ni, F.P. Incropera, Extension of the continuum model for transport phenomena occurring during metal alloy solidification - II. Microscopic considerations, Int. J. Heat Mass Transf. 38 (1995) 1285–1296. doi:10.1016/0017-9310(94)00237-P.

[56] C.J. Vreeman, M.J.M. Krane, F.P. Incropera, The effect of free-floating dendrites and convection on macrosegregation in direct chill cast aluminum alloys Part I: model development, Int. J. Heat Mass Transf. 43 (2000) 677–686. doi:10.1016/S0017-9310(99)00174-X.

[57] C.J. Vreeman, F.P. Incropera, The effect of free-floating dendrites and convection on macrosegregation in direct chill cast aluminum alloys Part II: predictions for Al-Cu and Al-Mg alloys, Int. J. Heat Mass Transf. 43 (2000) 687–704. doi:10.1016/S0017-9310(99)00175-1.

[58] I. Vusanovic, M.J.M. Krane, Macrosegregation in horizontal direct chill casting of ternary Al alloys: Investigation of solid motion, IOP Conf. Ser. Mater. Sci. Eng. 27 (2012) 1–6. doi:10.1088/1757-899X/27/1/012069.

[59] P. Marepalli, J.Y. Murthy, B. Qiu, X. Ruan, Quantifying Uncertainty in Multiscale Heat Conduction Calculations, J. Heat Transfer. (2014). doi:10.1115/1.4027348.

[60] A. Chernatynskiy, S.R. Phillpot, R. LeSar, Uncertainty Quantification in Multiscale Simulation of Materials: A Prospective, Annu. Rev. Mater. Res. 43 (2013) 157–182. doi:10.1146/annurev-matsci-071312-121708.

[61] R.A. Hardin, K.K. Choi, N.J. Gaul, C. Beckermann, Reliability based casting process design optimisation, Int. J. Cast Met. Res. 28 (2015) 181–192. doi:10.1179/1743133614Y.0000000142.

[62] K. Fezi, M.J.M. Krane, Uncertainty Quantification in Solidification Modelling, IOP Conf. Ser. Mater. Sci. Eng. 84 (2015) 012001. doi:10.1088/1757-899X/84/1/012001.

[63] M. Hunt, B. Haley, M. McLennan, M. Koslowski, J. Murthy, A. Strachan, PUQ: A code for non-intrusive uncertainty propagation in computer simulations, Comput. Phys. Commun. 194 (2015) 97–107. doi:10.1016/j.cpc.2015.04.011.

[64] F.C. Blake, The Resistance of Packing to Fluid Flow, Am. Inst. Chem. Eng. 14 (1922) 415–421.

[65] J. Kozeny, Ueber kapillare Leitung des Wassers im Boden, Sitzungsber Akad. Wiss., Wien. 136(2a) (1927) 271306.

[66] P.C. Carman, Fluid Flow through Granular Beds, Trans. Inst. Chem. Eng. 15 (1937) 150–167.

[67] P.C. Carman, Determination of the Specific Surface of Powders, J. Soc. Chem. Ind. 57 (1938) 225–234.

[68] P.C. Carman, Permeability of saturated sands, soils and clays, J. Agric. Sci. 29 (1939) 262. doi:10.1017/S0021859600051789.

[69] M.J.M. Krane, Modeling of Transport Phenomena during Solidification Processes, in: ASM Handbook, Vol. 22B, Met. Process Simul., ASM International, 2010: pp. 157–167.

[70] M. Ishii, N. Zuber, Drag coefficient and relative velocity in bubbly, droplet or particulate flows, AIChE J. 25 (1979) 843–855. doi:10.1002/aic.690250513.

[71] C.J. Vreeman, Modeling Macrosegregation in Direct Chill Cast Aluminum Alloys, M.S. Thesis Purdue University, 1997.

[72] S. V. Patankar, *Numerical Heat Transfer and Fluid Flow*, McGraw-Hill, New York, NY, 1980.

[73] C.J. Vreeman, F.P. Incropera, Numerical Discretization of Species Equation Source Terms in Binary Mixture Models of Solidification and Their Impact on Macrosegregation in Semicontinuous, Direct Chill Casting Systems, Numer. Heat Transf. Part B Fundam. 36 (1999) 1–14. doi:10.1080/104077999275749.

[74] V.R. Voller, C.R. Swaminathan, General Source-Based Method for Solidification Phase Change, Numer. Heat Transf. Part B Fundam. 19 (1991) 175–189. doi:10.1080/10407799108944962.

[75] M. Lalpoor, D.G. Eskin, D. Ruvalcaba, H.G. Fjær, A. Ten Cate, N. Ontijt, *et al.*, Cold cracking in DC-cast high strength aluminum alloy ingots: An intrinsic problem intensified by casting process parameters, Mater. Sci. Eng. A. 528 (2011) 2831–2842. doi:10.1016/j.msea.2010.12.040.

[76] W.F. Gale, *Smithells Metals Reference Book*, 8th ed., Elsevier, 2004.

[77] T. Iida, R. Guthrie, *The Physical Properties of Liquid Metals*, Clarendon Press, Oxford, 1988.

[78] J.O. Andersson, T. Helander, L. Höglund, P. Shi, B. Sundman, Thermo-Calc & DICTRA, computational tools for materials science, Calphad Comput. Coupling Phase Diagrams Thermochem. 26 (2002) 273–312. doi:10.1016/S0364-5916(02)00037-8.

[79] K. Fezi, A. Plotkowski, M.J.M. Krane, A Metric for the Quantification of Macrosegregation during Alloy Solidification, Metall. Mater. Trans. A. 47 (2015) 2940–2951. doi:10.1007/s11661-016-3420-z.

[80] D.G. Neilson, F.P. Incropera, Unidirectional solidification of a binary alloy and the effects of induced fluid motion, Int. J. Heat Mass Transf. 34 (1991) 1717–1732. doi:10.1016/0017-9310(91)90148-8.

[81] A. Plotkowski, M.J.M. Krane, The Effect of Velocity Based Packing Schemes on Macrosegregation Development in Simulations of Equiaxed Solidification, Appl. Math. Model. In Review (2016).

[82] A. Plotkowski, M.J.M. Krane, On the Numerical Prediction of Channel Segregation, Int. J. Heat Mass Transf. 100 (2016) 11–23.

[83] M.D. Morris, Factorial Sampling Plans for Preliminary Computational Experiments, Technometrics. 33 (1991) 161–174. doi:10.2307/1269043.

[84] F. Campolongo, J. Cariboni, A. Saltelli, An effective screening design for sensitivity analysis of large models, Environ. Model. Softw. 22 (2007) 1509–1518. doi:10.1016/j.envsoft.2006.10.004.

[85] J. Yanke, K. Fezi, R.W. Trice, M.J.M. Krane, Simulation of Slag-Skin Formation in Electroslag Remelting Using a Volume-of-Fluid Method, Numer. Heat Transf. Part A Appl. 67 (2014) 268–292. doi:10.1080/10407782.2014.937208.

[86] A. Plotkowski, M.J.M. Krane, The Use of Inverse Heat Conduction Models for Estimation of Transient Surface Heat Flux in Electroslag Remelting, J. Heat Transfer. 137 (2015) 0313011–0313019. doi:10.1115/1.4029038.

VITA

VITA

Alexander J. Plotkowski
Graduate School, Purdue University

Alex Plotkowski was raised in Grandville Michigan where he lived with his parents and sister. He attended Grandville High School, and upon graduation in 2007, enrolled in the engineering program at Grand Valley State University. During his time at GVSU, he maintained Dean's list honors in every semester, held officer positions in both the ASME and Tau Beta Pi student chapters, and earned the Co-op Student of the Year award and the Neimeyer graduate student award for interdisciplinary achievement for the 2012 academic year. He graduated with honors in 2012 with a Bachelor's degree in Mechanical Engineering, a minor in Mathematics, and a Master's degree in Product Design and Manufacturing Engineering. In the fall of 2012 he joined the School of Materials Engineering at Purdue University where he worked for Dr. Krane. His research primarily focused on numerical methods for transport phenomena in alloy solidification, but also included projects on inverse heat conduction, property measurements for slags used in electroslag remelting, and approximate analytical models for alloy solidification. For serving as a teaching assistant for MSE 230, he was given the Teaching Academy Graduate Teaching Award in 2013.

PUBLICATIONS

PUBLICATIONS

A. Plotkowski and M. J. M. Krane, “The Use of Inverse Heat Conduction Models for Estimation of Transient Surface Heat Flux in Electroslag Remelting,” *J. Heat Transfer*, **137**, 031301-1 – 031301-9, 2015. doi:10.1115/1.4029038.

A. Plotkowski, K. Fezi, and M. J. M. Krane, “Estimation of transient heat transfer and fluid flow for alloy solidification in a rectangular cavity with an isothermal sidewall,” *J. Fluid Mech.,* **779**, 53-86, 2015. doi:10.1017/jfm.2015.424.

A. Plotkowski, J. deBarbadillo, and M. J. M. Krane, “Characterization of the Structure and Thermophysical Properties of Solid ESR Slags”, *Materials Science & Technology,* Published online. doi:10.1080/02670836.2015.1116134.

K. Fezi, **A. Plotkowski**, and M. J. M. Krane, “A Metric for the Quantification of Macrosegregation during Alloy Solidification”, *Metall. Mater. Trans. A*, **47**, 2940-2951, 2016. doi:10.1007/s11661-016-3420-z.

A. Plotkowski and M. J. M. Krane, “On the Numerical Prediction of Channel Segregation”, *International Journal of Heat and Mass Transfer*, **100**, 11-23.

A. Plotkowski and M. J. M. Krane, “The Effect of Velocity Based Packing Schemes on Macrosegregation Development in Simulations of Equiaxed Solidification”, *Applied Mathematical Modelling*, In Press.

K. Fezi, **A. Plotkowski**, and M. J. M. Krane, “Macrosegregation Modeling During Direct Chill Casting of Aluminum Alloy 7050”, Numerical Heat Transfer A, Submitted March 2016.

A. Plotkowski and M. J. M. Krane, “The Discrete Nature of Grain Attachment Models in Simulations of Equiaxed Solidification”, *International Journal for Numerical Methods in Fluids*, Submitted May 2016.

A. Plotkowski and M. J. M. Krane, “A Continuum Grain Attachment Model for Simulations of Equiaxed Solidification”, Computational Materials Science, Submitted May 2016.

A. Plotkowski and M. J. M. Krane, “Quantification of Epistemic Uncertainty in Grain Attachment Models for Equiaxed Solidification”, To be submitted May 2016.